Leveraging open-top light-sheet microscopy for 3D pathology: building tools for clinical studies

Kevin Warner Bishop

A dissertation

submitted in partial fulfillment of the

requirements for the degree of

Doctor of Philosophy

University of Washington

2024

Reading Committee:

Jonathan T.C. Liu, Chair

Suzie H. Pun

Drew L. Sellers

Lawrence D. True

Program Authorized to Offer Degree:

Bioengineering

Chapter 2 © Copyright 2020
Optical Society of America under the terms of the OSA Open Access Publishing Agreement

Chapter 3 © Copyright 2024
Optica Publishing Group

Chapter 4 © Copyright 2024
Springer Nature

All other material © Copyright 2024
Kevin Warner Bishop

University of Washington

Abstract

Leveraging open-top light-sheet microscopy for 3D pathology: building tools for clinical studies

Kevin Warner Bishop

Chair of the Supervisory Committee:
Jonathan T.C. Liu
Mechanical Engineering

Cancer is a leading cause of death in the United States and represents a heterogeneous set of diseases with a wide variety of treatment approaches and patient outcomes. Biopsies are often used for both initial diagnosis and to grade disease aggressiveness, a key component in making appropriate treatment recommendations. Slide-based pathology is the current gold standard for microscopic analysis of biopsies and other tissue specimens. Despite widespread use, slide-based analysis carries a number of disadvantages. First, slide-based pathology inherently limits analysis to discrete 2D cross sections, which make it difficult to characterize complex 3D tissue structures like vasculature or glandular networks. Second, pathologists typically review only a few sections from each specimen due to the time and labor required to prepare and view each slide, often

equating to less than 1% of the entire tissue volume. Third, physical sectioning destroys tissue, complicating downstream molecular assays and archiving. An emerging alternative to slide-based pathology is non-destructive 3D pathology, which provides comprehensive visualization of 3D tissue structure without destructive sectioning. A number of proof-of-concept studies have suggested that 3D pathology can provide clinically relevant information. However, large-scale clinical studies, which will be key for clinical adoption, have remained challenging. This is in part because existing methods for 3D pathology are not optimized for high-throughput imaging of hundreds to thousands of clinical specimens. To enable comprehensive clinical studies using 3D pathology, this dissertation presents a set of imaging technologies and workflows leveraging open-top light-sheet (OTLS) microscopy, a platform for 3D pathology that provides rapid volumetric imaging of large clinical specimens. The goal of this suite of methods is to offer a toolkit for 3D pathology research in the near term and serve as a step towards clinical adoption of 3D pathology in the long term.

TABLE OF CONTENTS

List of Figures x

List of Tables xx

Chapter 1. Introduction 1

1.1 Limitations of slide-based pathology for cancer diagnosis 1

1.2 Approaches to 3D pathology 4

1.3 Summary of issues addressed in this work 8

1.4 Additional work completed during the PhD: *In vivo* microscopy for non-invasive screening and surgical guidance 9

Chapter 2. Performance tradeoffs for single- and dual-objective open-top light-sheet microscope designs: a simulation-based analysis 10

2.1 Introduction 10

2.2 Analysis approach 14

2.2.1 Geometric constraints and simplifying assumptions for dual-objective systems 16

2.2.2 Geometric constraints and simplifying assumptions for dual-objective systems 17

2.2.3 Non-orthogonal dual-objective design 18

2.2.4 Quantitative output metrics 21

2.3 Analysis results 22

2.3.1 Resolution 22

2.3.2 Contrast 29
2.4 Discussion 32
2.5 Acknowledgements 35
Chapter 3. Axially swept open-top light-sheet microscopy for densely labeled clinical specimens 36
3.1 Introduction 36
3.2 Optical design 39
3.3 Results & discussion 41
3.4 Acknowledgements 46
Chapter 4. An end-to-end workflow for nondestructive 3D pathology 46
4.1 Introduction 46
4.1.1 Development of the protocol 47
4.1.2 Protocol overview 51
4.1.3 Applications and limitations 57
4.1.4 Comparison with other methods 60
4.1.5 Experimental design 63
4.1.6 Required expertise 67
4.1.7 Regulatory approvals 67
4.2 Materials 68
4.2.1 Biological materials 68
4.2.2 Reagents 69
4.2.3 Reagent setup 70
4.2.4 Equipment 70

4.3 Procedure 72
4.3.1 Tissue preparation 72
4.3.2 3D microscopy 76
4.3.3 Data processing 83
4.3.4 Quality control 88
4.4 Troubleshooting 90
4.4.1 General approaches to troubleshooting image quality 90
4.4.2 Specific problems and possible solutions 91
4.5 Outline of timing 96
4.6 Anticipated results 96
4.6.1 Archived human pathology specimens using standard Path3D 97
4.6.2 Path3D variants for clinical and preclinical tissues 97
4.6.3 Viewing and interacting with Path3D datasets 98
4.7 Code availably 98
4.8 Acknowledgements 99

Chapter 5. Future work: Assessing the prevenance of the “poorly formed gland” morphology in prostate cancer using 3D pathology 100

5.1 Introduction 100
5.2 Methods 105
5.2.1 Specimen preparation and imaging with open-top light-sheet microscopy 105
5.2.2 Selection of candidate glands 106
5.2.3 Pathologist annotation 106
5.3 Anticipated results 107

Chapter 6. Conclusion 108

Bibliography 110

Appendix A. Performance tradeoffs for single- and dual-objective open-top light-sheet microscope designs: a simulation-based analysis 122

A.1 Remote focus geometric analysis and NA limits for single-objective systems 122

A.2 Resolution and contrast computation 125

A.2.1 Spatial resolution computation 125

A.2.2 Contrast computation 127

A.3 Survey of commercial objectives 130

A.4 PSF focal volume for various architectures 132

A.5 Contrast of a dual-objective system at various collection NAs 134

A.6 Differences in working distance between configurations for example designs 134

Appendix B. Axially swept open-top light-sheet microscopy for densely labeled clinical specimens 135

B.1 List of optical components 136

B.2 Volumetric tile size 136

B.3 Ray-trace optical simulation 137

Appendix C. An end-to-end workflow for nondestructive 3D pathology 137

C.1 Image atlas of clinical and preclinical tissues processed with variants of the standard Path3D protocol 137

C.2 Photos showing agarose bead phantom preparation 139

C.3 Example scatter plot illustrating local vs. global PSF variations 139

C.4 PSF heatmaps of well-aligned vs. misaligned microscopes 140
C.5 Identifying peak signal level, background level, and noise level 142
C.6 False coloring settings..... 143
C.7 Schematic of beam paths for troubleshooting..... 143
C.8 Photos showing visual appearance of tissue after tissue preparation problems..... 145
C.9 Napari interface for interacting with Path3D data. 145
C.10 Alternative interfaces for interacting with Path3D data 146
C.11 PSF computation details 148
C.12 Improving Napari efficiency..... 149
C.13 Image processing approaches to normalize signal level..... 150
C.13.1 Lateral variations 151
C.13.2 Depth variations..... 151

LIST OF FIGURES

Figure 1.1. Conventional slide-based pathology workflow, adapted with permission from Springer Nature [2] and created in part with BioRender.com. 2

Figure 1.2. Many biological structures such as **(a)** convoluted glandular or vasculature networks, **(b)** complex distributions of cells, or **(c)** rare cells dispersed across large tissue volumes are more accurately characterized by 3D pathology than 2D pathology. Adapted with permission from Springer Nature [2]. 3

Figure 1.3. Comparison of microscopy techniques for 3D pathology. Imaging approaches can be broadly categorized into destructive sectioning-based techniques and non-destructive volumetric-imaging-based techniques. Sectioning-based techniques include **(a)** knife-edge scanning microscopy. Non-destructive techniques include **(b)** laser-scanning (e.g., confocal or multiphoton) microscopy, **(c)** conventional light-sheet microscopy, and **(d)** open-top light-sheet microscopy. Reproduced with permission from Springer Nature [2]. 7

Figure 2.1. Overview of single- and dual-objective light-sheet microscope (LSM) architectures. **(a)** Optical schematic of a conventional orthogonal dual-objective (ODO) open-top light-sheet (OTLS) system, showing the illumination (blue) and collection (green) light paths. **(b)** Inset of illumination and collection objectives of an ODO system, showing that the system's effective working distance (WD_{system}) is much less than the collection objective's working distance ($WD_{objective}$). **(c)** Optical schematic of a non-orthogonal single-objective (NOSO) OTLS system, showing the illumination (blue) and collection (green) light paths. **(d)** Inset of the shared primary objective of a NOSO system, showing the angled light sheet and collection path. CL: cylindrical lens, TL: tube lens, DBS: dichroic beam splitter. 11

Figure 2.2. Outline of the analysis approach followed. Three key design parameters were identified that, in the context of cleared tissue imaging, primarily determine the optical performance of an LSM system (regardless of specific architecture): the numerical aperture (NA) of the illumination beam, the NA of the collection beam, and the crossing angle between them. We then introduced limits on these parameters based on practical constraints including available objectives and the physical placement of those objectives. These limits give rise to a range of feasible designs. Finally, we assess the optical performance of these designs in terms of spatial resolution and contrast. 15

Figure 2.3. Geometry of a proposed non-orthogonal, dual-objective (NODO) design showing **(a)** the optical schematic and **(b)** inset of the illumination and collection objectives. The crossing angle θ is less than 90° so that the collection objective can be oriented in the normal direction with respect to the horizontal sample holder, as in a NOSO system. This allows the full working distance of the collection objective to be used and minimizes sensitivity to refractive-index mismatch. Unlike the NOSO architecture, NODO also allows the full NA of the collection objective to be used and allows for a higher crossing angle between the illumination and collection beams (with implications for axial resolution and contrast). The NODO design uses a remote focus, as in a NOSO system. CL: cylindrical lens, TL: tube lens, WD: working distance.....19

Figure 2.4. Axial resolution of a dual-objective system. **(a)** Axial resolution depends strongly on crossing angle at small angles but does not improve much beyond angles of 60°. Curves for two example illumination and collection NA pairs are shown ($NA_i = 0.1$, $NA_c = 0.4$; $NA_i = 0.2$, $NA_c = 0.$), but these trends are consistent across different choices of illumination and collection NA. **(b)** The minimum angle plotted for each system is the minimum crossing angle before the objective cones overlap. **(c)** The maximum crossing angle is 90° (the conventional ODO case), which yields the maximum possible axial resolution.....23

Figure 2.5. Impact of illumination NA on axial resolution for **(a)** an ODO system, **(b)** a NODO system at a crossing angle of 60°, and **(c)** a NOSO system using a 1.0 NA primary objective. In all cases, illumination NA is a primary driver of axial resolution. Collection NAs of 0.4 and 0.7 are shown, but trends are similar for other collection NAs. A diagram of each configuration is shown below each corresponding plot. 25

Figure 2.6. Lateral resolution as a function of collection NA for **(a)** an ODO system and **(b)** a NODO system with a 60° crossing angle. Different curves on each plot indicate different choices of illumination NA. Curves are largely unchanged both within each plot and between plots, indicating that lateral resolution in a dual-objective system is primarily determined by collection NA and is independent of illumination NA and crossing angle....26

Figure 2.7. Lateral and axial resolution as a function of collection NA for a NOSO system in the case of **(a)** a moderate-NA primary objective (0.75 NA) and **(b)** a high-NA primary objective (1.0 NA). In each plot, the primary objective NA is held constant to reveal the different performance combinations a designer could achieve with a given optical element.

For simplicity, the illumination NA is also held constant (0.2). Note that changing the collection NA implicitly changes the effective crossing angle in our NOSO simulations. **(c)** Cone angles and PSF schematic for a moderate-NA shared primary objective. At moderate objective NAs, the crossing angle θ is constrained to relatively small values. Any further reduction in crossing angle, resulting from an increase in collection NA, leads to a degradation in axial resolution. Thus, there is a tradeoff between axial and lateral resolution. **(d)** Cone angles and PSF schematic for a high-NA shared primary objective. The crossing angle θ is relatively large in all cases, such that axial resolution is less sensitive to changes in collection NA. For ease of comparison, a single example collection NA (0.6) is shown in both (c) and (d).....27

Figure 2.8. Contrast of a dual-objective system. **(a)** Impact of crossing angle on contrast is plotted for three illumination NAs (different curves). A collection NA of 0.7 is used in this example, though the trends shown hold for other collection NAs (with slight improvements in contrast overall at higher collection NAs). The minimum angle plotted for each system is the minimum crossing angle before the illumination and collection cones overlap. The maximum angle plotted is 90° (the conventional ODO case) which gives the maximum possible contrast. These cases are shown for a 0.1 illumination NA and 0.7 collection NA system in **(b)** and **(c)**, respectively. Contrast improves with higher crossing angles, but gains begin to saturate around 60°. 30

Figure 2.9. Comparison of contrast for ODO, NODO (60° crossing angle), and NOSO systems that can be built using **(a)** a moderate-NA (0.7) primary objective and **(b)** a high-NA (1.0) primary objective (i.e., the collection objective for dual-objective systems or the shared primary objective for single-objective systems). For simplicity, the effective collection NA is held constant for each NOSO curve (0.5 for the moderate-NA case and 0.7 for the high-NA case). For all systems, increasing the illumination NA improves contrast but offers diminishing returns at higher illumination NAs. The NOSO system provides poorer contrast than the ODO or NODO systems in the moderate-NA case, while all systems provide similar contrast in the high-NA case.....31

Figure 3.1. Open-top light-sheet (OTLS) systems using **(a)** a low-NA unswept illumination light sheet providing a large FOV (green) on the camera, **(b)** a high-NA unswept light sheet that

underfills the camera due to the reduced depth of focus, and **(c)** a high-NA light sheet that is swept in synchrony with the rolling shutter to recover a large FOV. 37

Figure 3.2. Optical layout of the illumination **(a)** and collection **(b)** arms. **(c)** Schematic of the optical arrangement near the sample. A: aspheric lens, $GV_{X/Y}$: galvo mirrors, C: cylindrical lens, L_{1-6}: spherical lenses, O_{1-4}: objectives, FW: filter wheel.....40

Figure 3.3. (a-b) Axial PSF measurements from a bead phantom with and without axial sweeping across the FOV. **(c-d)** One camera frame of a human kidney (FLARE amine stain) with and without sweeping, demonstrating an increased usable FOV. 43

Figure 3.4. 3D dataset of a human prostate specimen stained with a fluorescent analog of H&E and imaged with both a high-NA swept illumination light sheet and low-NA unswept light sheet. **(a-b)** *En face* views (XY cross section) false-colored to mimic conventional H&E staining show fused glands indicative of Gleason pattern 4 carcinoma, arrows in (a). **(c-d)** Zoomed views of the cytoplasm channel show improved contrast and separation of red blood cells with axial sweeping. **(e-f)** Axial views (XZ cross section) from the nuclear channel show improved contrast and axial resolution (sharper peaks) with axial sweeping. Line intensity profiles **(g)** from the nuclear channel of (a-b), **(h)** from the cytoplasm channel of (c-d), and **(i)** from the nuclear channel of (e-f).....44

Figure 4.1. (a) Flowchart showing the four key sections to the Path3D workflow: tissue preparation, 3D microscopy, data processing and quality control. Iterative optimization is essential for producing consistent and high-quality datasets. **(b)** Each section of the standard Path3D protocol can be adapted on the basis of the needs of a specific application. **(c)** Path3D datasets are suitable for a range of scientific analyses based on computational analysis, visual interpretation or a combination of the two. AI, artificial intelligence; ECi, ethyl cinnamate. 49

Figure 4.2. (a) 3D rendering (produced using Imaris) and *en face* 2D cross sections of a 3-mm-diameter punch biopsy of prostate cancer tissue (FFPE) false-colored to mimic the appearance of standard H&E staining. **(b)** 3D rendering (produced using Imaris) and orthogonal 2D cross sections of a 1-mm-diameter core-needle biopsy of prostate cancer tissue false colored to mimic the appearance of standard H&E staining. **(c)** 2D cross section of squamous mucosal tissue false colored to mimic the appearance of standard H&E staining. **(d)** 2D cross section of colon cancer tissue shown with both H&E false coloring

and standard fluorescence coloring. **(e)** 2D cross section of esophagus tissue (Barrett's esophagus) shown with both H&E false coloring and standard fluorescence coloring. Images are shown with a standard sharpening filter. Panel (c) adapted from reference [77] under Creative Commons license CC BY 4.0. 51

Figure 4.3. (a) Various sample types, including common archival specimens such as multi-specimen blocks, large single specimens and punch biopsies, can be used with Path3D. **(b)** Tissue punches are loaded into six-well cassettes for deparaffinization (Step 1A). **(c)** Cassettes are incubated in xylene on a hot plate with a magnetic stir bar (Step 1B). **(d)** Biopsies are individually incubated in the staining solution in a Roto-Therm rotator (Step 2B). **(e)** Biopsies are individually cleared by incubating in ECi on an orbital shaker (Step 2D). 52

Figure 4.4 Initially, agarose bead phantoms are qualitatively assessed in real time while being previewed to optimize the focus and alignment of the microscope (Step 5). **(a)** An example bead image (single slice) shows the relative bead density. Line profiles of a well-focused bead, **(b)**, in the *X*, **(c)**, and *Y*, **(d)**, directions show symmetric Gaussian profiles with peak detector counts well above the background level. After imaging a 3D volume, the Bead_PSF_computation package is used to quantify the full width at half maximum (FWHM) values for each bead (Step 6). **(e)** A histogram of lateral (*X*) FWHM values from all beads acquired with a well-aligned microscope shows a distribution centered near the expected resolution with minimal spread. The inset shows an *XY* slice of the average 3D Gaussian curve fit. **(f)** A heat map from a well-aligned example shows consistent lateral resolution with respect to the *X* and *Y* position within the imaged volume. A perceptually uniform diverging colormap [90] (Matplotlib [91], 'coolwarm') is intentionally used to accentuate regions of particularly poor resolution. See **Figure C.4** for additional details on heat maps. 54

Figure 4.5 Images and line profiles (the yellow line in each image) are from human prostate tissue imaged with OTLS microscopy and show various staining, clearing and imaging conditions. **(a)** Optimal staining and imaging conditions showing high SBR (>10) and peak signal levels (>2,000 detector counts) in both channels with uniform signal levels across the tissue. Insets show well-resolved collagen fibers (eosin channel) and nuclei (TO-PRO-3 channel). **(b)** Poor clearing results in scattering of illumination and/or collection beams,

degrading image sharpness with depth. **(c)** Insufficient deparaffinization results in poor staining (especially at the core of the sample) in both channels. **(d)** Excessive eosin concentration causes the illumination light to be absorbed before reaching the interior of the tissue, resulting in bright edges and a dark core. Note the laterally asymmetric brightness when imaging at depth because of the illumination light entering from one side of the tissue in this particular imaging geometry (OTLS microscopy) (**Figure C.7**). **(e)** Uneven staining because of poor TO-PRO-3 penetration in tissue resulting in bright edges and a dark core. **(f)** Low eosin signal level (resulting in poor SNR) because of inadequate dye concentration, laser power or exposure time. Note the presence of noise artifacts (vertical stripes) in the image because of insufficient SNR. 91

Figure 5.1. Schematic of Gleason grading system for grading of prostate cancer based on 2D glandular morphology, where higher scores indicate more aggressive disease. © 2015 Indiana University. 102

Figure 5.2. Two-dimensional cross sections taken from a 3D prostate cancer dataset. Yellow arrows indicate a gland that appears poorly formed (i.e., lacking a lumen), indicative of Gleason pattern 4, at a depth of 70 μm. Upon 3D examination, the same gland is revealed to be a tangential section of a well-formed Gleason pattern 3 gland. Adapted from [150]. CC BY 4.0. 104

Figure A.1. (a) Optical schematic of a non-orthogonal single-objective (NOSO) LSM system, showing the illumination (blue) and collection (green) light paths. **(b)** Inset of the shared primary objective of a NOSO system showing the angled light sheet and collection path. **(c, d)** Inset of the remote focus of a NOSO system (c) without a refractive prism, showing some light is lost at the remote focus and (d) with a refractive prism, showing collection of otherwise lost light. CL: cylindrical lens, TL: tube lens, DBS: dichroic beam splitter. 123

Figure A.2. Computational methods for analyzing the resolution and contrast of a given configuration. **(a)** Three-dimensional point spread functions (PSFs) (assuming Gaussian illumination and uniform collection) are computed separately and multiplied together using the adjoint method to calculate a system PSF. **(b)** Resolution is computed by finding the full width at half maximum through the center of the system PSF in the lateral and axial directions (relative to the collection objective). **(c)** To analyze relative differences in image contrast, the system PSF is convolved with a random bead phantom, in which single voxels

are set to a value of 1 to simulate diffraction-limited fluorescent beads. Relative contrast levels are then computed based on the value of the response at the locations of the beads (I_{beads}) relative to the background signal level seen in the images ($I_{background}$). 126

Figure A.3. Example diffraction-limited fluorescent bead phantom and response for contrast computation. A 0.01% bead concentration is shown for an orthogonal dual-objective (ODO) system with 0.7 collection NA and 0.2 illumination NA. Note that the figure shows a single slice of a 3D phantom, so many beads visible in the response cannot be seen in the phantom as they are in planes in front of or behind the plane shown. 128

Figure A.4. Variation in contrast measurement for a dual-objective system for various bead concentrations in the simulated fluorescent phantom. **(a-c)** Impact of crossing angle on contrast for 0.01%, 0.1%, and 0.5% bead phantoms. Each plot shows contrast at three different illumination NAs (different curves). A collection NA of 0.7 is used for all systems in this example. **(d-f)** Example phantom responses for bead concentrations of 0.01%, 0.1%, and 0.5%, respectively. Near-perfect contrast is achieved regardless of configuration at low concentrations (sparsely labeled samples; (a) and (d)) but varies significantly with configuration at higher concentrations (densely labeled samples; (c) and (f)). 129

Figure A.5. Impact of illumination NA on PSF volume for **(a)** an ODO system, **(b)** a NODO system at a crossing angle of 60°, and **(c)** a NOSO system using a 1.0 NA primary objective. Collection NAs of 0.4 and 0.7 are shown. In all cases, PSF volume depends significantly on both illumination NA and collection NA. All three configurations show similar focal volume trends, indicating that architecture is not a significant driver of focal volume on its own. 133

Figure A.6. Contrast of a dual-objective system as a function of crossing angle for collection NAs of 0.4, 0.7, and 1.0. In all cases, contrast improves with crossing angle until around 60°, at which point further gains are minimal. Contrast also improves slightly at higher collection NAs, as the collection objective provides some additional optical sectioning at higher NAs. 134

Figure B.1. Volumetric tiles are created by stage scanning the sample along the X axis through a stationary field of view (determined by the width and depth-of-focus of the illumination light sheet). The volumetric tile width and height (YZ cross section) are determined by the field of view, and the depth (X dimension) is determined by the scan extent. Imaging larger

tiles decreases the total number of tiles required to cover a given volume, reducing the number of overlapping seams (redundantly imaged regions). Fewer seams significantly reduces the computational time required to fuse tiles into a contiguous 3D volume and reduces stitching artifacts. 136

Figure B.2. A ray-trace simulation of the illumination arm was performed Zemax OpticStudio to validate the voice-coil-based axial sweeping method. The solid curves show the RMS line spread (half width) at the illumination light sheet beam waist for each wavelength (i.e., the spread due to geometric aberrations alone). The dotted lines show the diffraction-limited half line width (i.e., without aberrations). The line spread is below the diffraction-limited line width across the axial focal range for each wavelength, indicating near-diffraction-limited performance. O_1 was modeled based on US patent 9001420B2. Models for the remaining lenses were obtained from their manufacturers. 137

Figure C.1. Image atlas of clinical and preclinical tissues processed with variants of the standard Path3D protocol. **(a)** Fixed human lymph node prepared with a CUBIC-clearing-based Path3D variant [8] and false colored to mimic the appearance of standard H&E staining, shown as volumetric renderings (generated using Aivia) and 2D cross sections. **(b)** Fresh human head & neck cancer surgical specimen (tongue) prepared using a single-stain (acridine orange) Path3D variant without clearing. A single 2D view of the irregular tissue surface was computationally extracted from a thin 3D volume. Nuclear and cytoplasmic channels were computationally separated and false colored to mimic the appearance of standard H&E staining [114]. **(c)** Whole mouse kidney with vasculature and glomeruli labelled with antibodies delivered via *in vivo* retro-orbital injection and cleared with ECi. A maximum intensity projection color-coded by depth (left) allows visualization of the whole kidney vasculature in a single image. 139

Figure C.2. Photos showing agarose bead phantom preparation. Phantoms molded in inverted microcentrifuge tubes (step 3F) form flat-bottomed cylindrical plugs, which are convenient for use with inverted or open-top microscopes with a planar sample holder. 139

Figure C.3. Example scatter plot illustrating local vs. global PSF variations. The plot was produced by the Bead_PSF_computation package (step 6) and shows individual beads in a volumetric agarose phantom dataset. Scatter plots show how a microscope's lateral resolution (FHWM of individual beads) changes across the field of view (X position). Well-

aligned microscopes should have a global variance (i.e., average FWHM values in one region relative to another) of 25% or less. Due uncertainty inherent in measuring the FWHM of diffraction-limited beads, there may be significantly higher variance between individual beads. 140

Figure C.4. PSF heatmaps of well-aligned vs. misaligned microscopes. Heat maps were generated with the Bead_PSF_computation package (step 6) from example agarose bead datasets and show how a microscope's resolution varies across the field of view (FOV). Each point represents a single diffraction-limited bead. The bead's position indicates its location in the FOV (XZ plane in this case), while the color indicates the full width at half maximum (FWHM) of the fit Gaussian function in the lateral or axial direction. In the well-aligned case, **(a)** there is minimal variation in resolution across the FOV. In the rotated case, **(b)** the axial resolution is degraded in the lower left and upper right corners of the FOV, suggesting the light-sheet focus is rotated relative to the camera. In the decentered case, **(c)** the axial resolution at the bottom of the FOV is degraded relative to the top of the FOV, indicating the light-sheet focus is not centered within the FOV. Note that a perceptually uniform diverging colormap [90] (Matplotlib [91], "coolwarm") is used, such that beads near the center of the FWHM range appear dull and beads at the edges of the range appear brightly colored. This was selected intentionally to accentuate regions of particularly poor resolution, as these regions are typically the most informative for assessing resolution uniformity. 141

Figure C.5. Identifying peak signal level, background level, and noise level**. (a)** Human prostate tissue with eosin staining. **(b)** Profile of yellow line shown in (a) indicating peak signal level and background level. Empty gland lumens indicated by orange arrows in (a) show up as regions of background signal in (b). **(c)** Zoom in of a background region indicated by red box in (b) shows random noise level. 142

Figure C.6. False coloring settings. The same raw fluorescence data, **(a)** can be used to generate false-colored data with a range of appearances, **(b)** by adjusting the color parameters (such as normalization factors) in FalseColor Python (step 18).....143

Figure C.7. Schematic of beam paths for troubleshooting. Understanding light paths of a given microscope can be useful to troubleshoot image quality issues. **(a)** In this example, a uniformly stained specimen is imaged on an open-top light-sheet (OTLS) microscope. Due

to excessive eosin concentration, illumination light is rapidly attenuated by dye absorption at the tissue surface. This results in bright signal at the edges facing the illumination beam (I) and low signal at the tissue core and edges facing away from the illumination beam (II). **(b)** Upon initial inspection, *en face* views of the dataset can give the appearance of poor dye penetration, illumination light attenuation, or collection light attenuation. However, evaluation of light paths reveals that high signal is seen in areas of short illumination path length in tissue (I) and that low signal is seen in areas of long illumination path length in tissue (II), suggesting that illumination attenuation due to excessive dye concentration is the culprit. 144

Figure C.8. Photos showing visual appearance of tissue after tissue preparation problems. **(a)** Uneven TO-PRO-3 staining of a human prostate specimen results in visible dark patches on the tissue surface (yellow arrows). **(b)** Mouse flank skin specimen shown after increasing amounts of time in ECi clearing medium. Short clearing times result in a relatively opaque specimen. By 2 hours of clearing, the specimen is relatively transparent and suitable for imaging. 145

Figure C.9. Napari interface for interacting with Path3D data. Napari viewer (steps 19 - 20), showing a false-colored Path3D dataset of a human prostate core needle specimen. The interface allows users to pan, zoom, and scroll to different depth levels, as well as add annotations. 146

Figure C.10. Alternative interfaces for interacting with Path3D data. **(a)** QuPath interface, showing a false-colored human esophagus biopsy. Pathologist annotations indicating regions of low-grade dysplasia (yellow) and high-grade dysplasia (red). **(b)** Custom web interface developed by Ground Truth Labs showing a false-colored human prostate core needle specimen. The integrated grading section below the image allows pathologists to record information such as Gleason grade and presence of cribriform glands for each specimen. 147

LIST OF TABLES

Table 4.1. Troubleshooting of Path3D 92
Table A.1. Survey of commercial objectives for cleared tissue imaging 130
Table A.2. Comparison of effective system working distance between ODO and NOSO/NODO configurations 135
Table B.1. Optical components used in axially swept OTLS microscope 136

ACKNOWLEDGEMENTS

First, I would like to thank my PhD advisor, Prof. Jon Liu, for his mentorship over the past five years. He has helped me grow tremendously as a scientist, as a communicator, and has taught me how to always focus the clinical needs driving research. Thank you to Dr. Adam Glaser, who became like a second advisor when I began graduate school and taught me an incredible amount about optics and research as a whole. I also thank my committee members for their guidance as I completed my thesis: Profs. Dan Fu, Suzie Pun, Drew Sellers, and in particular Prof. Larry True for his wealth of clinical knowledge and enthusiasm for 3D pathology.

I thank my collaborators in the UW Chemistry department, Prof. Josh Vaughan and Dr. Che Poudel, for their invaluable advice both scientifically and professionally during my PhD. I also thank my collaborators at Oxford University, particularly Prof. Ian Mills and Dr. Dylan Windell, who helped get a light-sheet microscope from Seattle to England and for being such generous hosts in the UK.

The Engage Science Communication program at UW helped me learn how to bring science beyond the lab, and I'm grateful for the opportunity to join such a vibrant community of science communicators and friends.

I'm grateful to Prof. Christine O'Brien at Washington University in St. Louis for being a wonderful mentor to me and role model of compassion in academia both before and during my PhD.

I thank Chelsea Gibbs for our thesis writing group, without which this document might not exist, and more importantly for her friendship throughout my time in Seattle.

I am grateful to all the members of Molecular Biophotonics Lab. In particular, I am grateful to Rob Serafin for our many valuable brainstorming sessions about science (and food) and being my go-to Python expert, Dr. David Brenes for tirelessly answering all my questions about postdoc life and for our countless chats about surviving academia, and Dr. Lindsey Erion Barner for everything she taught me about microscopy as well as for being my running buddy and a huge source of moral support throughout my PhD. I am lucky to have met such incredible colleagues and lifelong friends.

Finally, I thank my parents, my brother, my constant companion Beans, and most importantly my wife Erika who has been my biggest supporter. None of this would have been possible without her confidence, level-headedness, occasional righteous indignation, and love, and I will always be grateful.

Chapter 1. Introduction

1.1 Limitations of slide-based pathology for cancer diagnosis

Cancer is the second leading cause of death in the United States (behind heart disease) and represents a diverse range of diseases with highly heterogenous treatment approaches and patient outcomes [1]. For most types of cancer, biopsies (small pieces of tissue excised from a patient) are an essential tool for disease detection and diagnosis. Following initial diagnosis, a key function of biopsies is for grading disease aggressiveness, which is essential to determine appropriate treatment recommendations. Many aggressive treatments courses, while effective in halting disease progression, carry significant side effects, and are ideally reserved for patients with high-risk disease in order to limit unnecessary burden on the patient and the healthcare system. Conversely, more conservative treatment approaches such as active surveillance in prostate cancer (and in some cases forgoing immediate treatment entirely) are often appropriate in patients with low-risk disease.

Slide-based pathology is considered the gold standard for microscopic analysis of biological tissue specimens and is widely used in a range of applications, including assessing surgical margins during tumor resection, analyzing clinical and pre-clinical specimens in research contexts, and evaluation of diagnostic biopsies for cancer diagnosis. In a typical pathology workflow, collected tissue specimens are fixed in formalin, dehydrated, embedded in paraffin wax, cut into thin (~5 μm) sections, mounted on glass slides, stained, and viewed under a widefield microscope (**Figure 1.1**).

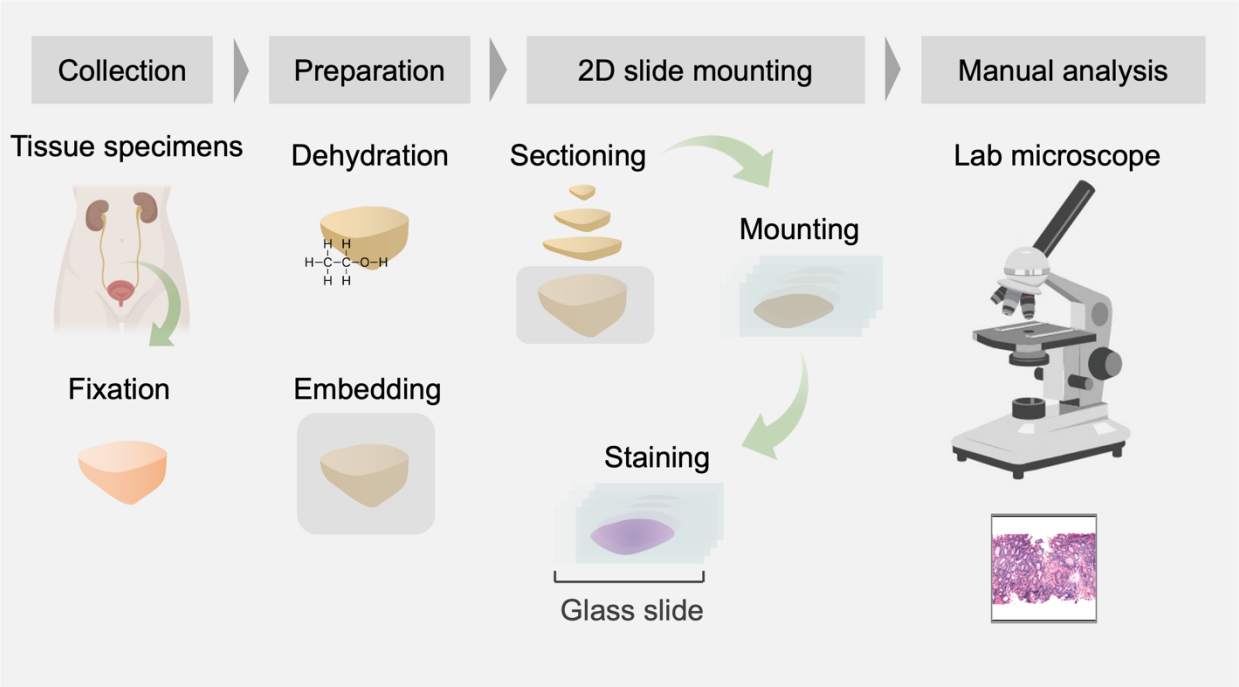


Figure 1.1. Conventional slide-based pathology workflow, adapted with permission from Springer Nature [2] and created in part with BioRender.com.

Despite widespread use, conventional slide-based pathology carries a number of disadvantages. First, slide-based analysis inherently limits examination to 2D tissue structure. While discrete 2D cross sections accurately represent some structures, many biological tissues are composed of complex and interconnected 3D structures, such as vascular or glandular networks, that are difficult to visualize with 2D sections (**Figure 1.2**a). Second, preparing individual pathology slides is both time and labor intensive, meaning only a few sections from each specimen are reviewed in most cases. In a clinical context, this typically equates to a pathologist reviewing less than 1% of the total volume of a biopsy specimen. For complex distributions of tissue components, particularly in heterogeneous tissues like cancer, the resultant undersampling can inadequately characterize spatial relationships or the relative abundance of various cells and structures (**Figure 1.2**b). Rare events or cell types (e.g., immune infiltrates) can be missed

altogether (**Figure 1.2**c). Note that in addition to microscopic sampling bias introduced by slide-based pathology, macroscopic sampling bias can be introduced by selecting a finite number of biopsy sites from a macroscopically heterogeneous tissue. See Section 1.4 for additional discussion of this related challenge. Third, physical sectioning of valuable tissue specimens is inherently destructive to part or all of the tissue, making downstream molecular assays (e.g., genomic analysis) or archiving more challenging.

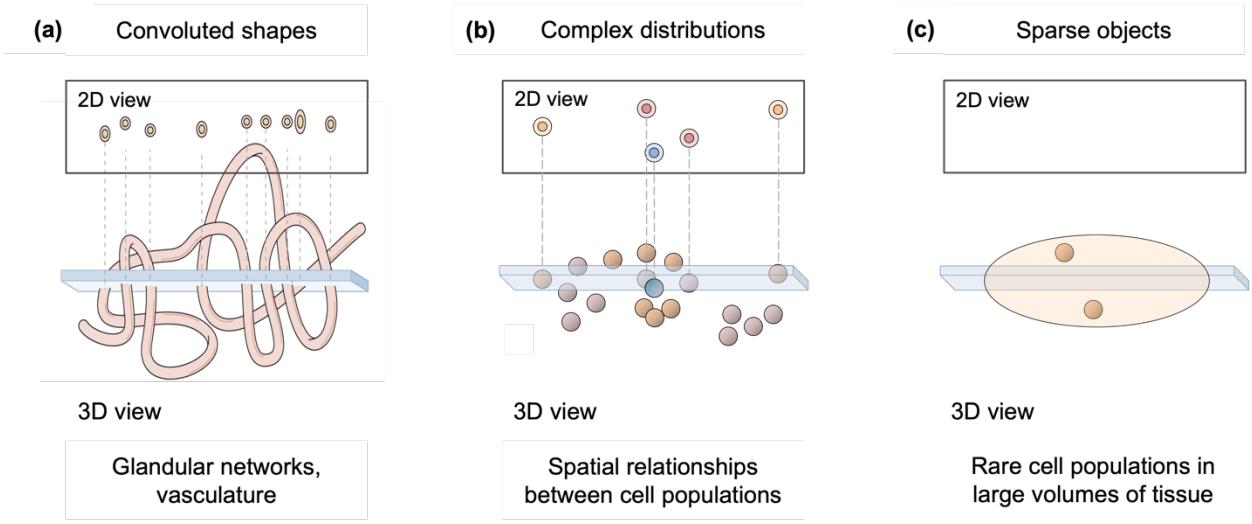


Figure 1.2. Many biological structures such as **(a)** convoluted glandular or vasculature networks, **(b)** complex distributions of cells, or **(c)** rare cells dispersed across large tissue volumes are more accurately characterized by 3D pathology than 2D pathology. Adapted with permission from Springer Nature [2].

Three-dimensional pathology, the focus of this work, is an alternative approach to slide-based analysis of tissues in which entire tissue specimens are imaged and visualized in three dimensions [2,3]. Three-dimensional pathology approaches address many of the limitations outlined above, providing 3D structural information, comprehensive sampling of tissue specimens, and (in some cases) non-destructive imaging, which preserves valuable specimens for downstream analysis or archiving. An increasing number of studies by our group and others have presented

preliminary results pointing to the value of 3D pathology in various disease contexts, including 3D mapping of immune infiltrates in head & neck cancer [4], 3D changes in kidney structure in renal biopsies [5], mapping of 3D microvasculature in bladder cancer [6,7], improved accuracy in assessing lymph-node metastasis size for breast cancer using 3D pathology [8], and improved detection of neoplasia in esophageal biopsies using 3D pathology [9,10]. Finally, 3D analysis may help resolve known grading ambiguities in prostate cancer, a particularly promising application that will be discussed in detail in Chapter 5.

1.2 Approaches to 3D pathology

A number of approaches to generating 3D pathology datasets have been proposed to date that can be broadly categorized as either destructive serial-sectioning techniques or non-destructive sectioning-free techniques. A brief comparison of these methods is provided below. Section 4.1.4 provides a detailed discussion of the technical tradeoffs of serial-sectioning and non-destructive 3D pathology methods, as well as further discussion of various labeling, optical clearing, and 3D imaging approaches that can be used for non-destructive 3D pathology. Several recent review articles also offer additional discussion of various 3D pathology methods [2,3,11].

Serial-sectioning techniques physically cut thin sections from a thick tissue specimen (e.g., using an automated microtome) and image each section in 2D (**Figure 1.3**a) [12–18]. Sequential 2D sections are then reconstructed into a contiguous 3D volume. This approach obviates the need for additional tissue preparation steps (such as the optical clearing and staining required for non-destructive techniques, which can be time consuming in thick tissue specimens). However, such approaches are inherently destructive as they require physically cutting specimens. This can make downstream archiving and molecular assays challenging, which is a significant limitation in the

context of valuable clinical samples. Sectioning-based approaches can also be prone to sectioning artifacts and may require complex and computationally intensive reconstruction strategies [18].

Non-destructive techniques rely on volumetric "optical sectioning" microscopy methods to directly image intact specimens in 3D without physical sectioning. Typically, these approaches rely on optical clearing protocols, chemical approaches that remove scattering biomolecules and provide a homogeneous refractive index for unaberrated imaging deep within thick tissue specimens. Uncleared tissues can be successfully imaged in 3D over certain depth ranges with some imaging methods, such as with multiphoton microscopy techniques that use longer illumination wavelengths, which scatter less in biological tissues [19,20].

Laser-scanning microscopy techniques (e.g., confocal and multiphoton microscopy) are the most widely available volumetric microscopy methods (**Figure 1.3**b) [5,19–23]. These approaches collect volumetric datasets point-by-point by raster scanning a focused beam across a specimen in three dimensions and collecting excited fluorescence on a point detector. While straightforward, laser-scanning techniques are relatively slow and, in the case of confocal microscopy, extremely light-inefficient, which can contribute to photobleaching. Light-sheet microscopy is an alternative technique in which a thin "sheet" of light excites fluorescence from a 2D plane within the specimen, which is imaged onto a 2D camera (**Figure 1.3**c) [24]. The light sheet (or specimen) is then scanned to collect consecutive 2D planes, forming a 3D volumetric dataset. Camera-based imaging makes light-sheet microscopy significantly faster than laser-scanning approaches and dramatically increases light efficiency. However, conventional light-sheet systems typically require bulky objectives to be placed in close proximity to the specimen and often require complex sample mounting schemes. This can make it difficult to efficiently image large or irregular samples (such as biopsies or surgical resections). Open-top light-sheet (OTLS) microscopy is a variation

of light-sheet microscopy in which illumination and collection optics are placed below a transparent planar sample holder (**Figure 1.3**d) [25–31]. The unobstructed open top can alleviate constraints on sample size/shape and can enable straightforward mounting of multiple specimens at once, making it an appealing platform for high-throughput 3D pathology. Additional discussion of the benefits and tradeoffs of OTLS microscopy is provided in Section 2.1.

In short, there are a variety of promising approaches for 3D pathology, each with distinct pros and cons depending on requirements such as speed, ease of use, and tissue preservation. The remainer of this work will primarily focus on non-destructive 3D pathology of cleared tissues using OTLS microscopy due its advantages in the context of large-scale studies of clinical specimens. However, many of the topics discussed here are also applicable to other 3D pathology approaches.

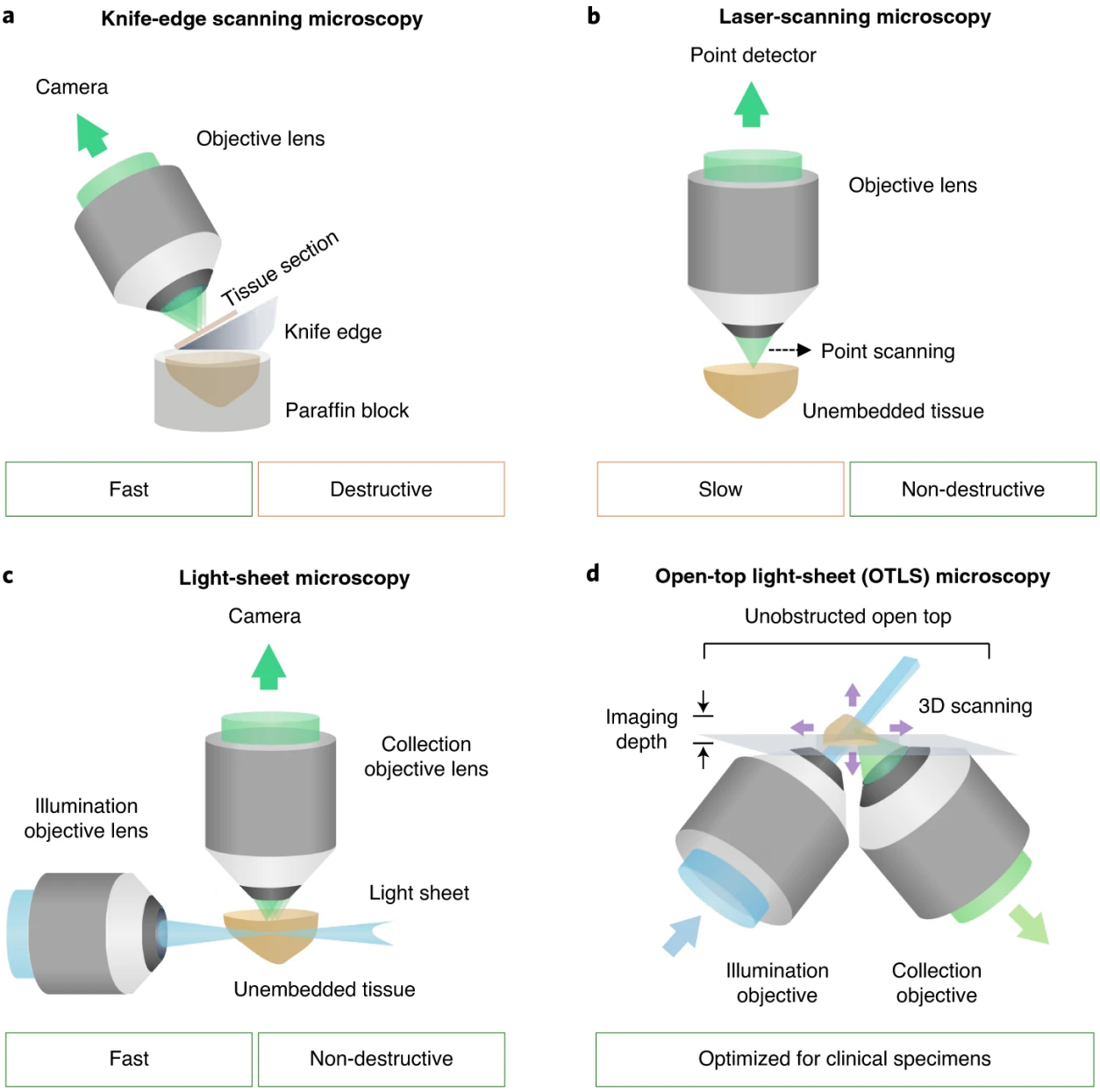


Figure 1.3. Comparison of microscopy techniques for 3D pathology. Imaging approaches can be broadly categorized into destructive sectioning-based techniques and non-destructive volumetric-imaging-based techniques. Sectioning-based techniques include **(a)** knife-edge scanning microscopy. Non-destructive techniques include **(b)** laser-scanning (e.g., confocal or multiphoton) microscopy, **(c)** conventional light-sheet microscopy, and **(d)** open-top light-sheet microscopy. Reproduced with permission from Springer Nature [2].

1.3 Summary of issues addressed in this work

In summary, there are a number of compelling proof-of-concept studies on technical aspects of 3D pathology including hardware development, as well as a growing number of examples in which 3D pathology provides clinically relevant information. Nonetheless, clinical studies quantifying differences in diagnostic or prognostic accuracy between 2D and 3D pathology have remained challenging. One contributing factor is that existing methods for generating 3D pathology data are generally not optimized for large-scale studies of hundreds to thousands of specimens. The remainder of this dissertation focuses on developing hardware tools and imaging workflows suitable for comprehensive clinical studies assessing the value of 3D pathology, specifically leveraging OTLS microscopy and tissue clearing for non-destructive 3D pathology.

Chapter 2 presents a simulation-based study comparing the optical performance and practical tradeoffs of various OTLS architectures, including description of a novel non-orthogonal dual objective (NODO) OTLS configuration. Chapter 3 describes a NODO OTLS microscope optimized specifically for high-throughput imaging of clinical specimens through the use of axially swept illumination, a strategy which improves imaging throughput and performance in densely labeled clinical tissues. Chapter 4 provides an end-to-end workflow for generating 3D pathology datasets from clinical specimens, with a specific emphasis on data quality and consistency in the context of large-scale clinical studies. Finally, Chapter 5 outlines an in-progress clinical study, which will leverage the tools described in the prior chapters to compare 2D and 3D pathology in the context of resolving Gleason grading ambiguities for prostate cancer. I anticipate that the collection of technologies and methods presented here will provide a toolkit for 3D pathology as a research tool in the short term and offer a valuable step towards clinical translation in the long term.

1.4 Additional work completed during the PhD: *In vivo* microscopy for non-invasive screening and surgical guidance

In addition to the work on 3D pathology described here, I spent a portion of my PhD working on *in vivo* microscopy. Conventional excisional biopsy presents several inherent challenges including requiring invasive procedures to remove tissue, difficulty in obtaining real time diagnostic information for intraoperative guidance, and potential undersampling of heterogeneous tissues (such as tumors). *In vivo* microscopy technologies provide real time microscopic assessment of tissues (sometimes referred to as "optical biopsy") without requiring specimens to be removed from the patient, often dramatically increasing the amount of tissue that can be interrogated. This work is not addressed further in this dissertation, but readers are encouraged to consult the following additional publications from my PhD for more information:

(1) **K. W. Bishop**, K. C. Maitland, M. Rajadhyaksha, and J. T. C. Liu, "In vivo microscopy as an adjunctive tool to guide detection, diagnosis, and treatment," *Journal of Biomedical Optics* **27**, (2022).

This publication is a perspective review exploring potential use cases along with translational opportunities and challenges of *in vivo* microscopy.

(2) **K. W. Bishop***, B. Hu*, R. Vyawhare*, Z. Yang*, D. C. Liang, G. Gao, E. Baraznenok, Q. Han, L. Lan, S. S. L. Chow, N. Sanai, and J. T. C. Liu, "Miniature line-scanned dual-axis confocal microscope for versatile clinical use," *Biomedical Optics Express* **14**, 6048–6059 (2023).

This publication describes a second-generation dual-axis confocal microscope optimized for clinical use cases, including disease detection and surgical guidance.

Chapter 2. Performance tradeoffs for single- and dual-objective open-top light-sheet microscope designs: a simulation-based analysis

The work in this chapter was published in *Biomedical Optics Express* (Bishop et al. 2020) [32] and is reprinted with permission. © 2020 Optical Society of America under the terms of the OSA Open Access Publishing Agreement

2.1 Introduction

Light-sheet microscopy (LSM), also known as selective plane illumination microscopy (SPIM), has become a valuable tool for many biomedical investigations and applications. In LSM, a sheet of light is used to excite fluorescence from a thin plane ("optical section") within a relatively transparent sample [24,33]. Adjacent 2D planes within the sample are successively illuminated and imaged using a high-speed camera to rapidly scan a volumetric region. A key advantage of this camera-based technique is that 3D imaging can be performed more quickly and simply than with laser-scanning microscopy (e.g., confocal and multiphoton microscopy). In addition, selective planar illumination is optically efficient, minimizing photobleaching of fluorophores and phototoxicity to living organisms [34]. LSM was originally popularized for volumetric imaging of live model organisms in developmental biology [33,35–37] and more recently has been explored for imaging large optically cleared *ex vivo* tissues [38–40], including clinical specimens [7,27,28].

A number of unique LSM architectures exist that can be broadly separated into two categories: dual-objective and single-objective LSM. Dual-objective systems use two separate objectives, arranged orthogonally to one another, for illumination and collection. Having two independent objectives provides optical-design flexibility but can place significant physical constraints on sample geometries. In an attempt to mitigate this issue, inverted LSM [36,39] and open-top light-sheet (OTLS) configurations [25,27,28,37] have been introduced in which dual objectives are

arranged at 45° angles with respect to a sample that is placed on a horizontal substrate (**Figure 2.1**a). Such designs reduce constraints on sample size and sample numbers (by allowing for unconstrained lateral image tiling) and simplify sample mounting, However, positioning the objectives at such oblique angles typically results in a reduction in axial (vertical) imaging range since the full working distance of the objectives cannot be easily accessed (**Figure 2.1**b). Additionally, achieving moderate- or high-numerical aperture (NA) imaging (i.e., NA > 0.5) using an OTLS architecture is challenging due to the precise index-matching requirements and/or corrective optics needed to minimize aberrations when high-NA off-axis beams transition between different media (e.g., immersion oil, sample holder, tissue) [26].

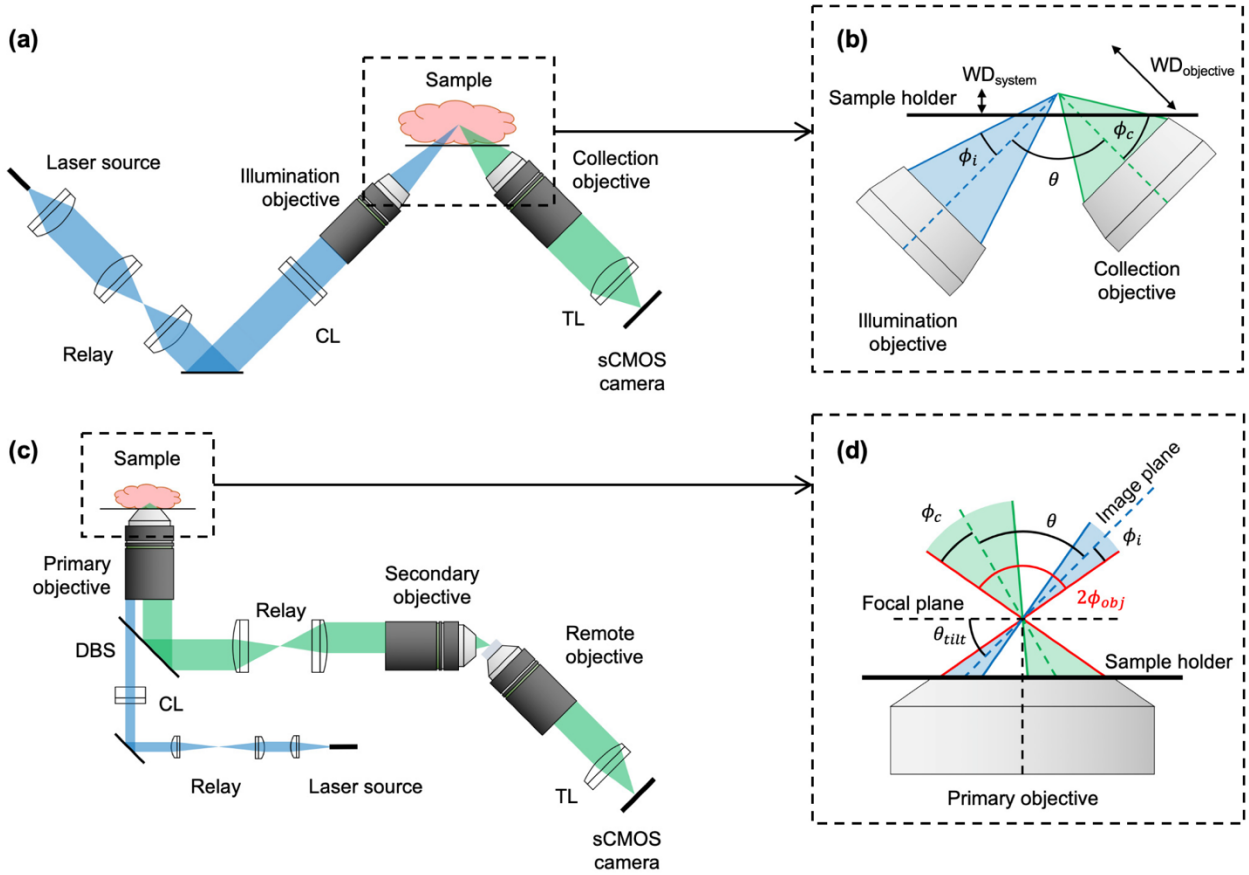


Figure 2.1. Overview of single- and dual-objective light-sheet microscope (LSM) architectures. **(a)** Optical schematic of a conventional orthogonal dual-objective

(ODO) open-top light-sheet (OTLS) system, showing the illumination (blue) and collection (green) light paths. **(b)** Inset of illumination and collection objectives of an ODO system, showing that the system's effective working distance (WD_{system}) is much less than the collection objective's working distance ($WD_{objective}$). **(c)** Optical schematic of a non-orthogonal single-objective (NOSO) OTLS system, showing the illumination (blue) and collection (green) light paths. **(d)** Inset of the shared primary objective of a NOSO system, showing the angled light sheet and collection path. CL: cylindrical lens, TL: tube lens, DBS: dichroic beam splitter.

Single-objective light-sheet microscopes have recently been developed [41–49], which use a portion of an objective's NA for illumination and a (typically larger) portion of the NA for collection (**Figure 2.1**c-d). The use of a single objective allows the full working distance of the objective to be made accessible for imaging the sample. In addition, orienting the objective in the normal direction with respect to a horizontal sample holder leverages the ideal aberration-correction properties that have been meticulously engineered into high-quality microscope objectives when imaging through flat interfaces, thus relaxing sample index-matching requirements. Furthermore, since the conjugate planes of the illumination and collection beams are the same, scanning the beams (e.g., with a mirror) in tandem, while maintaining their alignment within the sample, can be simplified.

A significant challenge in implementing a single-objective light-sheet design is that when both light paths share the same objective, the illumination light sheet cannot be oriented orthogonally to the objective collection. This makes it challenging to efficiently capture an in-focus image of the fluorescence generated by the light sheet on a flat detector array (camera chip). An innovation that has made single-objective LSM possible is creating a remote focus with a secondary objective such that a tilted third objective can be used to image the remote light sheet

onto a sCMOS detector array in the ideal orthogonal direction [41–49]. The details of this approach are described in Appendix A.1.

In light of the numerous LSM architectures and variations that have been developed in recent years, there is a natural desire amongst optical engineers to analyze their performance tradeoffs. While some analysis has been performed for a narrow subset of LSM configurations, such as examining different illumination profiles for dual-objective systems [50] and simulating various single-objective designs [51], a systematic comparison of diverse dual-objective and single-objective LSM designs has not been performed. Here we seek to fill this gap by presenting a quantitative analysis of dual- and single-objective LSM performance in response to several key design parameters. By quantifying design tradeoffs between different configurations, there is potential to identify "unreached" design spaces, which in turn will motivate future areas of innovation. For example, we describe a new non-orthogonal dual-objective (NODO) configuration that provides some advantages over orthogonal dual-objective (ODO) and non-orthogonal single-objective (NOSO) configurations for moderate-resolution applications.

It is impossible to provide a comprehensive guide for LSM design given the vast range of factors to consider such as sample characteristics (e.g., size, quantity, degree of optical clarity) and biological considerations (e.g., dynamic vs. static imaging, light dose), among others. Here we have focused our analysis on OTLS microscopy configurations for imaging fixed tissues that are optically cleared, in which optical scattering and refractive aberrations are assumed to be negligible. We also focus our analysis to assume conventional Gaussian illumination, which is the most-popular illumination method for LSM (note that a recent analysis of various LSM illumination schemes was performed by Remacha et al. [50]). With this context in mind, we examine a set of major performance metrics – primarily resolution and contrast – as functions of

a specific set of design parameters: illumination and collection beam NAs and crossing angle, as constrained by currently available objectives. Certain imaging applications could warrant consideration of alternative parameters. Optical scattering, for example, is a key consideration for imaging live, uncleared specimens, and has been examined with Monte-Carlo simulations in the past for LSM [52] and dual-axis confocal microscopy [53,54]. Nonetheless, we believe that our work represents a valuable first step towards guiding the design of OTLS systems.

2.2 Analysis approach

The overall analysis approach we followed is shown in **Figure 2.2**. We identified three key design parameters that, in the context of cleared-tissue imaging, are primary drivers of a system's optical performance regardless of the specific architecture (single- or dual-objective) used: the NA of the illumination beam, the NA of the collection beam, and the angle between the two beams. Note that we make several assumptions for the sake of simplifying our analysis. We assume single-photon (linear) Gaussian illumination, which is used in the majority of LSM applications. In particular, pure Gaussian illumination is assumed, which is a fair approximation for real Gaussian beams that are truncated (apodized) beyond the $1/e^2$ intensity points. Further, we assume that the collection NA is larger than the illumination NA, which is true in nearly all LSM systems. This allows for straightforward mathematical descriptions of geometric constraints, which in turn limit the numerical range of the design parameters that are analyzed (see next section). We assess optical performance in terms of spatial resolution and contrast (as determined by a simulated fluorescent bead phantom).

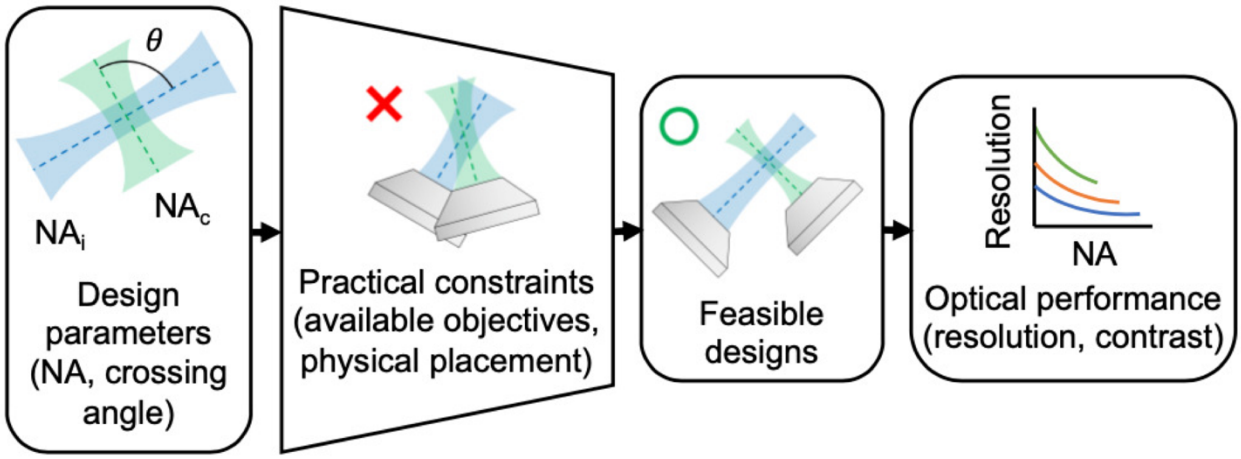


Figure 2.2. Outline of the analysis approach followed. Three key design parameters were identified that, in the context of cleared tissue imaging, primarily determine the optical performance of an LSM system (regardless of specific architecture): the numerical aperture (NA) of the illumination beam, the NA of the collection beam, and the crossing angle between them. We then introduced limits on these parameters based on practical constraints including available objectives and the physical placement of those objectives. These limits give rise to a range of feasible designs. Finally, we assess the optical performance of these designs in terms of spatial resolution and contrast.

Field of view is an important metric for some applications of LSM that is impacted by both the collection objective and the illumination NA (depth of focus of a Gaussian light sheet). However, here we assume light-sheet tiling is employed, as is common for LSM imaging of large cleared tissues. In other words, many adjacent fields of view (in all directions) in a sample volume are collected via stage scanning and computationally recombined to produce a single 3D volume. In this context, the field of view of each individual frame is less critical as the camera can be cropped as needed for smaller fields of view to maintain overall volumetric imaging rate. Additionally, axial sweeping (a technique in which the light sheet is optically scanned in the direction of propagation to increase the effective field of view) may be employed in conjunction

with tiling for high-NA (≥0.3) illumination beams, as described previously [55]. We therefore do not consider the effects of field of view in this work.

2.2.1 Geometric constraints and simplifying assumptions for dual-objective systems

The optical path for an ODO system is shown in **Figure 2.1**a. Note that these systems generally include scanning mirrors to translate the light sheet and/or stages to scan the specimen, but these have been omitted for simplicity in both **Figure 2.1**a and **Figure 2.1**c. For optically clear tissue specimens, unrestricted lateral sample extent is generally preferred. As such, we assume an OTLS architecture for both single- and dual-objective systems, which allows for a more-consistent comparison between various LSM architectures.

While the two objectives in a dual-objective system are typically placed orthogonally to one another, in principle their crossing angle is not restricted to 90°. The two objectives can be positioned at any angle relative to one another, provided they do not collide with each other.

We assume that the objective housing does not occupy additional space beyond the optical cone (NA) of the objective. In practice, the mechanical housing can restrict the minimum crossing angle attainable with a given objective pair. However, as the additional housing headroom can vary considerably between otherwise similar objectives, it is challenging to generalize this effect across all potential designs (see Appendix A.3). In order to provide an analysis that does not assume any specific commercial objective, we do not consider the objective housing in our simulations, with the acknowledgement that the designer must account for the additional housing headroom when considering candidate objectives. Given this assumption, the placement of the objectives is restricted by the crossing angle and the cone angles of the individual beams, as shown in **Figure 2.1**b. The half cone angle for each objective is determined by:

$$\phi = \sin^{-1}(NA/n) \tag{2.1}$$

Here, ϕ is the half cone angle, NA is the numerical aperture of the objective, and n is the refractive index of the immersion medium (assumed to be water, n=1.33, for this analysis). The objectives cannot physically collide, so the minimum crossing angle permitted in this system is the angle at which the illumination and collection cones begin to intersect:

$$\theta \geq \phi_i + \phi_c \tag{2.2}$$

Here, θ is the crossing angle between the optical axes of the two objectives, while ϕ_i and ϕ_c are the half cone angles of the illumination and collection objectives, respectively. In order to maintain an OTLS geometry, the objectives also cannot cross the horizontal sample holder as they would collide with the sample. The maximum crossing angle physically allowed is then constrained by:

$$\theta + \phi_i + \phi_c \leq 180° \tag{2.3}$$

This relationship assumes that the thickness of the sample holder and sample itself are negligible. Note that a crossing angle larger than 90° would never be used in practice. Equations (2.2) and (2.3) provide physical limits on how a dual objective system can be constructed, which constrain the numerical range of our simulations. Importantly, the observation that the crossing angle θ does not need to be set to 90° (as is the case in conventional orthogonal configurations) gives rise to a novel NODO design that we will examine closely later.

2.2.2 Geometric constraints and simplifying assumptions for dual-objective systems

Figure 2.1c shows the light path of a generic NOSO LSM system (with the objective arranged below the sample as previously described). As shown in **Figure 2.1**d, this configuration results in a light sheet that is tilted at some angle θ_{tilt} relative to the focal plane of the objective. The crossing angle of the illumination and collection cones is constrained by the physical NA of the shared primary objective. Assuming that the crossing angle is maximized for a given illumination and

collection NA (which offers the best performance, as shown later), the crossing angle θ is given by:

$$\theta = 2\phi_{obj} - \phi_c - \phi_i \tag{2.4}$$

Here, ϕ_{obj}, ϕ_c, and ϕ_i are the geometric half cone angles of the shared primary objective, the collection beam, and the illumination beam, respectively. Note that as in the dual-objective analysis, these geometric angles are assumed to be within a high-index medium (water, n=1.33, in this analysis).

Additional geometric analyses of the NOSO architecture (used to limit our simulations), and of light behavior at the remote focus, are provided in Appendix A.1. In particular, we assume that techniques are employed (as described by others [47,56,57]) to ensure that the collection beam can be imaged by a high-NA remote objective (and detected by the camera) with 100% throughput and negligible aberration. Likewise, we assume that the axial and lateral range of refocusing is sufficient to provide high-quality refocusing across the full field of view and depth of focus (as shown by others both theoretically and experimentally [43,57–60]). Finally, we acknowledge that use of a remote focus can introduce a range of other higher-order optical effects (e.g., Fresnel losses, point spread function [PSF] anisotropy). For the purposes of this comparison, we assume that such effects do not dominate system performance (especially for the NAs ≤1.0 evaluated here) and we direct readers to the studies cited above, and others [61], which evaluate such effects in detail.

2.2.3 Non-orthogonal dual-objective design

As mentioned previously, our analyses will include a NODO architecture, which combines attractive elements of both the ODO and NOSO configurations (we have described the implementation of this design in detail elsewhere [60]). In a NODO configuration, the collection

objective is kept perpendicular to the sample holder and a second low-NA objective is used for non-orthogonal illumination (**Figure 2.3**). Similar to NOSO systems, this offers the ability to access the full working distance of the collection objective for sample imaging, and significantly reduces sensitivity to index mismatch. Note that the latter issue (index mismatch) can be a major source of aberrations in ODO systems, where high-NA beams must transition between different media at highly oblique angles. Like the NOSO design, the NODO design requires use of a remote focus, which entails similar considerations (e.g., Fresnel losses, PSF anisotropy) to those described for the NOSO case in Appendix A.1. One difference is that in the NODO case, the entire NA of the collection objective may be used without geometric truncation at the remote focus, which is not true of the NOSO design. Specifically, there is an NA loss ($NA_i/2$ in one direction) for NOSO designs, which is not significant for very high-NA systems but becomes increasingly important at more moderate NAs [56].

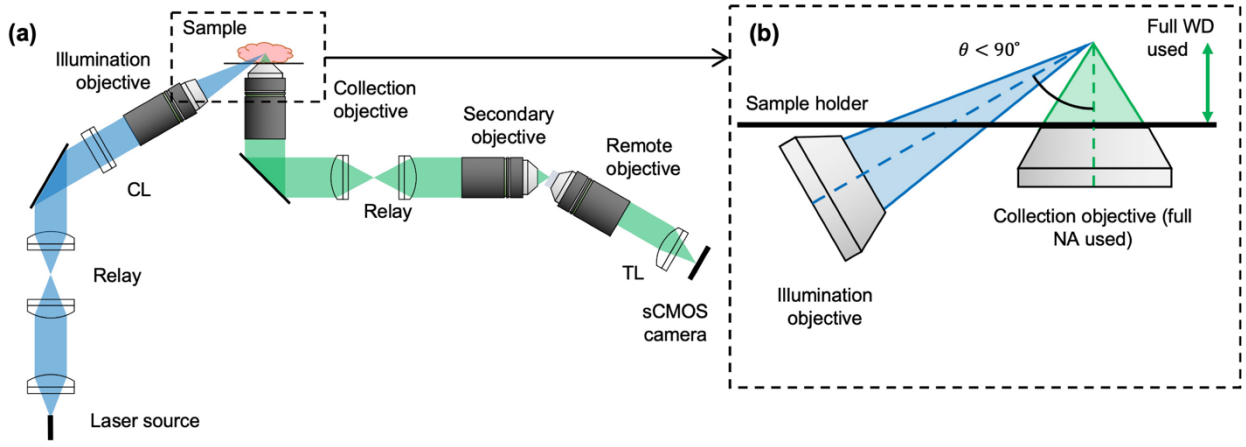


Figure 2.3. Geometry of a proposed non-orthogonal, dual-objective (NODO) design showing **(a)** the optical schematic and **(b)** inset of the illumination and collection objectives. The crossing angle θ is less than 90° so that the collection objective can be oriented in the normal direction with respect to the horizontal sample holder, as in a NOSO system. This allows the full working distance of the collection objective to be used and minimizes sensitivity to refractive-index

mismatch. Unlike the NOSO architecture, NODO also allows the full NA of the collection objective to be used and allows for a higher crossing angle between the illumination and collection beams (with implications for axial resolution and contrast). The NODO design uses a remote focus, as in a NOSO system. CL: cylindrical lens, TL: tube lens, WD: working distance.

Compared with NOSO designs, a major advantage of the NODO configuration is that since the illumination and collection beams do not need to share a single objective, there is more design flexibility in terms of beam NAs and crossing angle. One downside to a NODO system is that the illumination and collection paths no longer share a conjugate plane as in a NOSO system. This makes rapid scanning and descanning of these beams more challenging, such that the system may be less ideal for live-sample imaging. Additionally, since the collection objective is oriented normal to the sample holder, designers must consider the mechanical housing and working distance of the illumination objective to ensure the two objectives do not collide (similar to the mechanical considerations for the collection objective described in Appendix A.3). Depending on the mechanical housing of the specific objective used, crossing angles approaching 90° can be challenging to achieve in the NODO configuration due to potential collision between the illumination objective and sample holder. In theory, one could introduce a slight tilt in the collection objective to realize such angles while still being able to use most of the collection objective's working distance and reducing sensitivity to refractive index mismatch (compared to the ODO design). However, smaller angles (~60°) are readily achievable and can provide appealing performance characteristics (as we show below). Therefore, we will assume here that the collection objective always remains perpendicular to the sample holder. Even with these considerations in mind, the practical advantages of the NODO configuration for cleared-tissue

imaging warrant further consideration and quantitative comparison with conventional ODO and NOSO systems.

2.2.4 Quantitative output metrics

In cleared-tissue imaging, image quality is the primary performance metric of interest. Volumetric imaging speed is of concern, but typically scales in a predictable way with spatial resolution if samples are sufficiently labeled and photon counts are not a limiting factor. Light dose (i.e., photobleaching and photodamage) is not as critical compared with live-tissue imaging applications. We thus quantified the performance of different configurations in terms of the spatial resolution and contrast that is theoretically possible for a given system. We computed axial and lateral resolution values based on the simulated PSF of each system. We analyzed the contrast of each system by simulating the system's response to a virtual fluorescent bead phantom.

In LSM, axial resolution and contrast are related metrics, both arising from the fact that the light sheet provides "optical sectioning" in the axial direction. A recent study by Remacha et al. explores this topic in greater detail and proposes a method of differentiating the illumination light path's contribution to each of these metrics: axial resolution is defined as the width of the PSF in the axial direction (that is, the position where the PSF's local value crosses some threshold), while "optical sectioning thickness" is the axial range containing most of the light sheet's power [50]. We likewise define axial resolution based on the PSF width. We then use a bead phantom to measure contrast, a metric which encompasses the illumination beam's effect on contrast (optical sectioning) into a final contrast value describing what users would observe as the relative contrast of the entire system. Additional details regarding these resolution and contrast computations are provided in Appendix A.2.

2.3 Analysis results

In this study, we used the geometric constraints identified above to identify key input parameters for each microscope configuration. For dual-objective systems, the input parameters are: illumination NA, collection NA, and crossing angle (where ODO systems have a crossing angle of 90° and NODO systems have a crossing angle less than 90°). In single-objective systems, the input parameters are: primary objective NA, effective illumination NA, and effective collection NA. Note that these three parameters uniquely determine the crossing angle of the beams, as expressed in Eq. (2.4). We limited our simulations to a range of primary objective NAs (i.e., collection-objective NA for dual-objective systems) ranging from 0.4 to 1.0 based on currently available commercial objectives that are suitable for imaging cleared tissues (Appendix A.3). Axial resolution, lateral resolution, and contrast were computed as functions of the listed design parameters. Rather than presenting every possible combination of input parameters and output metrics, we focus our presentation on a number of observations that are deemed to be most critical for designers.

2.3.1 Resolution

2.3.1.1 For dual-objective systems, larger crossing angles improve axial resolution until ~60°

We first consider how the axial resolution of a conventional ODO system compares to a NODO system by examining how it varies as a function of crossing angle. **Figure 2.4**a shows this relationship for two pairs of illumination and collection NAs ($NA_i = 0.1$, $NA_c = 0.4$ and $NA_i = 0.2$, $NA_c = 0.7$). As expected, axial resolution improves with crossing angle, with the ODO configuration thus providing the best axial resolution. However, the gains in axial resolution are minimal beyond angles of ~60°, a finding that is consistent across NA pairs beyond those shown.

For example, increasing the crossing angle from 45° to 60° in the 0.1 illumination NA case (as shown) improves axial resolution by 16.8%. Conversely, increasing the crossing angle further from 60° to 75° only improves axial resolution by an additional 9.7%. Conveniently, a 60° crossing angle is readily achievable (in terms of physical placement of objectives) for most choices of illumination and collection NA, including for the NODO case in which the collection objective is oriented normal to the horizontal sample holder. Therefore, we use 60° as the crossing angle for all further analyses of NODO systems.

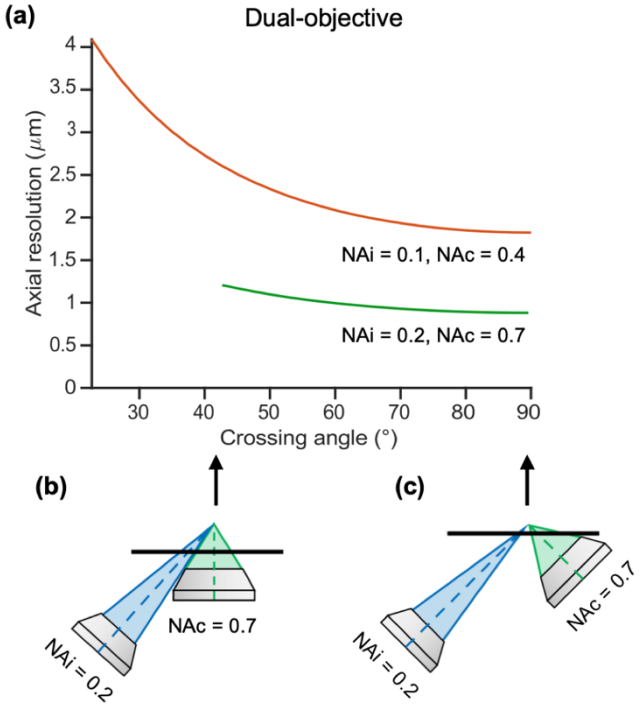


Figure 2.4. Axial resolution of a dual-objective system. **(a)** Axial resolution depends strongly on crossing angle at small angles but does not improve much beyond angles of 60°. Curves for two example illumination and collection NA pairs are shown ($NA_i = 0.1$, $NA_c = 0.4$; $NA_i = 0.2$, $NA_c = 0.$), but these trends are consistent across different choices of illumination and collection NA. **(b)** The minimum angle plotted for each system is the minimum crossing angle before the

objective cones overlap. **(c)** The maximum crossing angle is 90° (the conventional ODO case), which yields the maximum possible axial resolution.

2.3.1.2 For all systems, axial resolution is highly dependent upon illumination NA

Besides crossing angle, a primary driver of axial resolution is the light-sheet thickness as determined by the illumination NA. **Figure 2.5** shows the impact of illumination NA on axial resolution for each system architecture. As with standard microscopes, there are diminishing returns (nonlinear dependence) as the illumination NA is increased. Two collection NAs are shown in each plot (0.4 and 0.7). This trend is similar for other collection NA choices with a slightly diminishing impact of illumination NA on axial resolution as collection NA is increased. This is because as collection NA increases, the limited depth of focus of the collection objective increasingly provides optical sectioning, thereby reducing the relative contribution of light-sheet thickness to axial resolution. An implication of these observations is that while isotropic resolution at high NAs may be desirable in theory [36,55,62–64], the simplicity and geometric advantages of using an illumination NA less than the collection NA may offer an ideal compromise for many practical applications of LSM. Additional discussion of PSF isotropy (in terms of PSF volume) is provided in Appendix A.4.

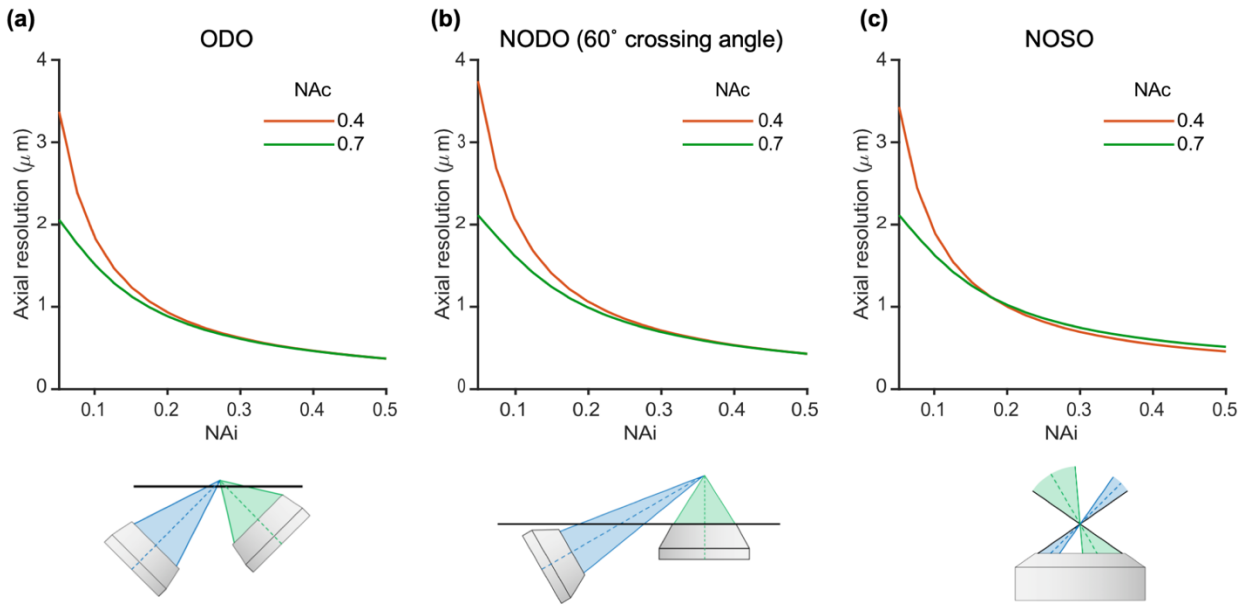


Figure 2.5. Impact of illumination NA on axial resolution for **(a)** an ODO system, **(b)** a NODO system at a crossing angle of 60°, and **(c)** a NOSO system using a 1.0 NA primary objective. In all cases, illumination NA is a primary driver of axial resolution. Collection NAs of 0.4 and 0.7 are shown, but trends are similar for other collection NAs. A diagram of each configuration is shown below each corresponding plot.

2.3.1.3 For dual-objective systems, lateral resolution is entirely determined by collection NA

The previous plots showed that in a dual-objective system, the axial resolution is primarily determined by illumination NA and crossing angle. We will now consider which factors are most impactful to lateral resolution in a dual-objective system. **Figure 2.6** shows how lateral resolution varies as a function of collection NA for an ODO system (a) and a NODO system with a 60° crossing angle (b). In these plots, the different colors correspond to different choices of illumination NA. In all cases, increasing the collection NA improves the lateral resolution. We also see that the different curves in each plot almost completely overlap, indicating that lateral resolution is not influenced greatly by illumination NA. Further, the curves are nearly identical between the ODO and NODO plots, indicating that lateral resolution is also independent of

crossing angle. In summary, lateral resolution in a dual-objective system is almost entirely determined by collection NA. Combined with the previous finding that axial resolution in a dual-objective system is primarily determined by illumination NA and crossing angle, we observe that using two objectives, which allows axial and lateral resolution to be decoupled, provides a designer with significant flexibility for optimizing system performance.

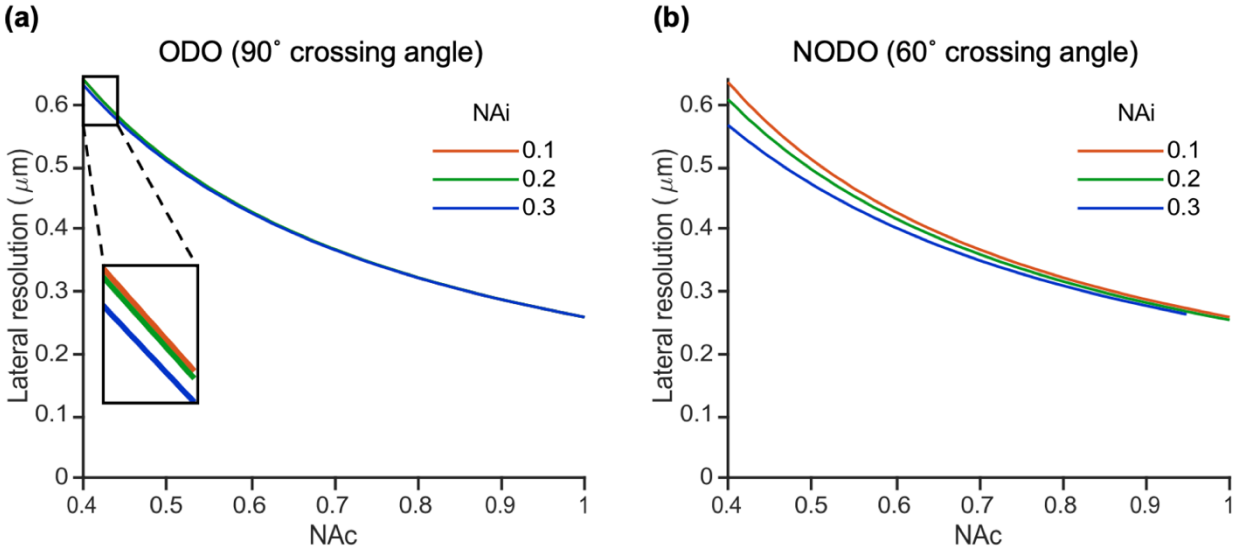


Figure 2.6. Lateral resolution as a function of collection NA for **(a)** an ODO system and **(b)** a NODO system with a 60° crossing angle. Different curves on each plot indicate different choices of illumination NA. Curves are largely unchanged both within each plot and between plots, indicating that lateral resolution in a dual-objective system is primarily determined by collection NA and is independent of illumination NA and crossing angle.

2.3.1.4 For single-objective systems with moderate NA, axial and lateral resolution must trade off

In contrast to the decoupling of axial and lateral resolution in a dual-objective system, axial and lateral resolution in a single-objective system are intrinsically linked because the two light paths share a single objective. **Figure 2.7** shows two example NOSO systems: one using a

moderate-NA primary objective (0.75, a) and one using a high-NA primary objective (1.0, b). In each plot, the primary objective NA is held constant, showing the different performance combinations a designer could achieve with a given optical element. For simplicity, the illumination NA is also held constant (selected as 0.2 for these examples) as it is generally restricted to a low value in a NA-constrained NOSO system. The plots show how axial and lateral resolution vary as functions of collection NA. Note that varying the collection NA implicitly changes the effective crossing angle of the illumination and collection light paths since they share one objective (as seen in Eq. (2.4)).

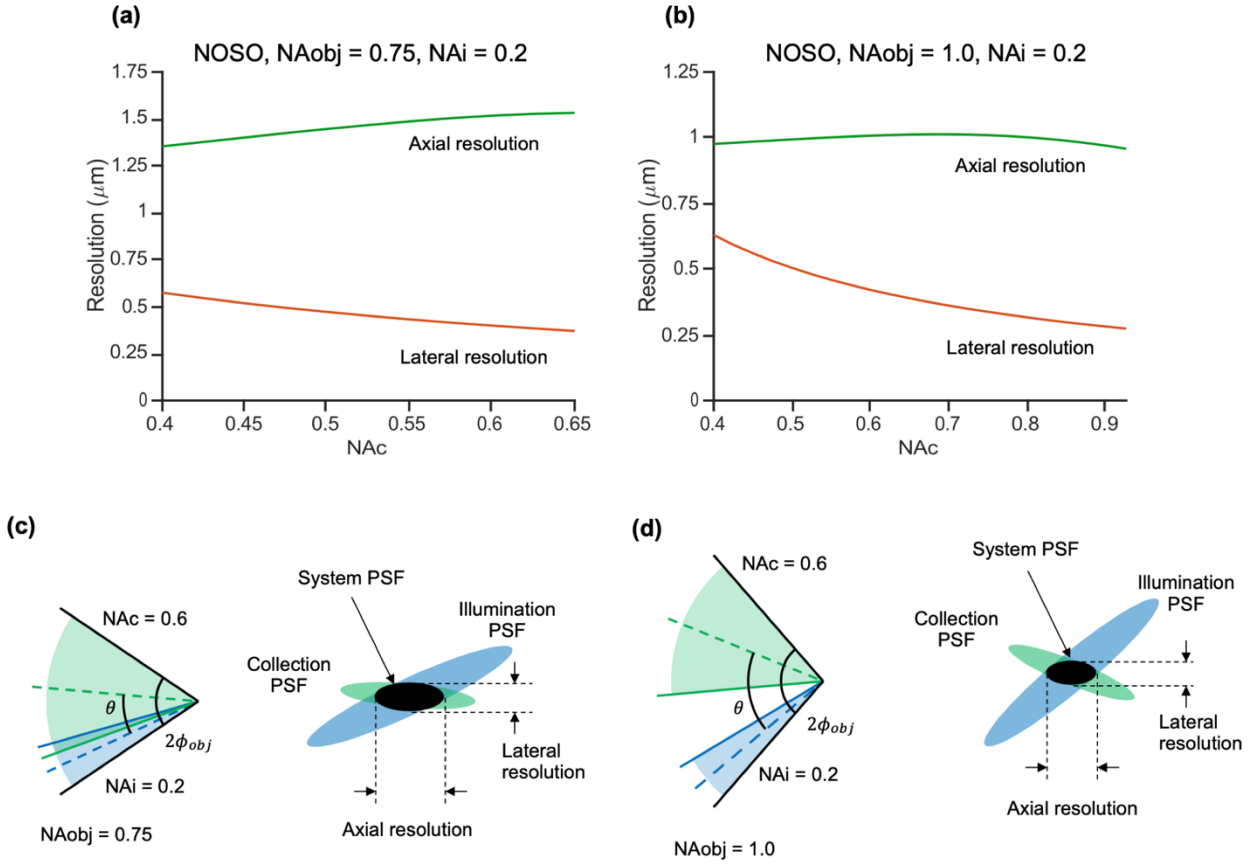


Figure 2.7. Lateral and axial resolution as a function of collection NA for a NOSO system in the case of **(a)** a moderate-NA primary objective (0.75 NA) and **(b)** a high-NA primary objective (1.0 NA). In each plot, the primary objective NA is held constant to reveal the different performance combinations a designer could achieve

with a given optical element. For simplicity, the illumination NA is also held constant (0.2). Note that changing the collection NA implicitly changes the effective crossing angle in our NOSO simulations. **(c)** Cone angles and PSF schematic for a moderate-NA shared primary objective. At moderate objective NAs, the crossing angle θ is constrained to relatively small values. Any further reduction in crossing angle, resulting from an increase in collection NA, leads to a degradation in axial resolution. Thus, there is a tradeoff between axial and lateral resolution. **(d)** Cone angles and PSF schematic for a high-NA shared primary objective. The crossing angle θ is relatively large in all cases, such that axial resolution is less sensitive to changes in collection NA. For ease of comparison, a single example collection NA (0.6) is shown in both (c) and (d).

We first consider the moderate-NA case (0.75 NA shared primary objective). Unsurprisingly, higher collection NAs result in superior lateral resolution. Interestingly, the increase in collection NA causes a degradation in axial resolution because it results in a smaller crossing angle between the illumination and collection light paths (**Figure 2.7**c), which lengthens the axial dimension of the system PSF. This finding highlights the implicit tradeoff between axial and lateral resolution in a single objective system. Note that **Figure 2.7**c-d illustrate one example choice of collection NA (0.6), while the plots above show the full range of possible collection NAs (as described in Appendix A.1).

At higher NAs (1.0 NA shared primary objective), the crossing angle remains relatively high regardless of effective collection NA. Therefore, axial resolution is not strongly dependent upon collection NA. In other words, for a high-NA NOSO system, axial and lateral resolution do not trade off to the extent that they must for a NOSO system with a lower primary objective NA. However, the beams must still share an objective, restricting the overall maximum collection NA and crossing angle that can be achieved in comparison to a dual-objective system.

2.3.2 Contrast

2.3.2.1 For dual-objective systems, larger crossing angles improve contrast until ~60°

In addition to the insights into resolution that have been discussed so far, we also identified quantitative trends regarding the contrast of single- and dual-objective systems. In **Figure 2.8**a, we consider the contrast of a dual-objective system as a function of crossing angle. See Appendix A.2 for details on the simulated fluorescent bead phantom used to determine contrast and the impact of different bead concentrations. Different curves represent different illumination NAs. A collection NA of 0.7 is used in this example, though the trends are similar for other collection NAs (with slight improvements in contrast at higher collection NAs). For example, plots for collection NAs of 0.4 and 1.0 are provided in Appendix A.5. Like in **Figure 2.4**, the minimum and maximum crossing-angle cases are depicted in **Figure 2.8**b and **Figure 2.8**c, respectively. Contrast improves at higher crossing angles as the collection and illumination light paths are more spatially separated. As with axial resolution of a dual-objective system, this dependence is strongest at small angles, and contrast improves little beyond 60°. For example, increasing the crossing angle from 45° to 60° in the 0.2 illumination NA case shown improves contrast by 14.0%. Conversely, increasing the crossing angle further from 60° to 75° only improves the contrast by an additional 5.4%. This reinforces the observation that a NODO system with a ~60° crossing angle is ideal, with optical performance close to that of an ODO system. Similar simulations with different bead concentrations are considered in Appendix A.2.

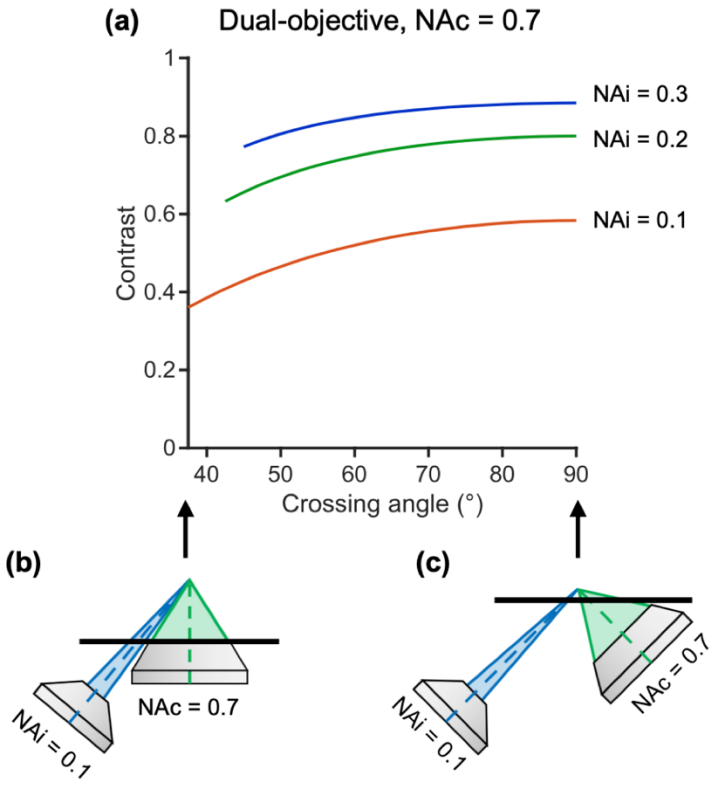


Figure 2.8. Contrast of a dual-objective system. **(a)** Impact of crossing angle on contrast is plotted for three illumination NAs (different curves). A collection NA of 0.7 is used in this example, though the trends shown hold for other collection NAs (with slight improvements in contrast overall at higher collection NAs). The minimum angle plotted for each system is the minimum crossing angle before the illumination and collection cones overlap. The maximum angle plotted is 90° (the conventional ODO case) which gives the maximum possible contrast. These cases are shown for a 0.1 illumination NA and 0.7 collection NA system in **(b)** and **(c)**, respectively. Contrast improves with higher crossing angles, but gains begin to saturate around 60°.

2.3.2.2 Contrast improves with higher illumination NA, and dual-objective systems exhibit improved contrast over single-objective systems at moderate NAs

Figure 2.9 compares the contrast of an ODO, NODO (60° crossing angle), and NOSO system as a function of illumination NA. In order to provide a fair comparison, we consider a moderate-

NA case (0.7, a) and high-NA case (1.0, b), keeping the collection/primary objective NA constant for each case. In other words, the plot shows the different configurations that could be constructed with the same optical element (a 0.7 or 1.0 NA objective). For simplicity, the effective collection NA is held constant (0.5 and 0.7 in a and b, respectively) for each NOSO curve in **Figure 2.9**. Different choices of collection NA change the upper limit on illumination NAs (as the beams must share one objective) but otherwise result in similar trends. Similar to axial resolution (**Figure 2.5**), contrast in all systems improves with illumination NA but offers diminishing returns (nonlinear dependence) at higher illumination NAs (as is true for standard microscopes). In addition, the ODO and NODO systems exhibit superior contrast to comparable NOSO systems at moderate NA. The main reason for this is that crossing angle plays a significant role in determining contrast, and dual-objective systems can achieve higher crossing angles, particularly in the moderate-NA case. At high NA, this effect is less significant, and all three systems provide similar contrast.

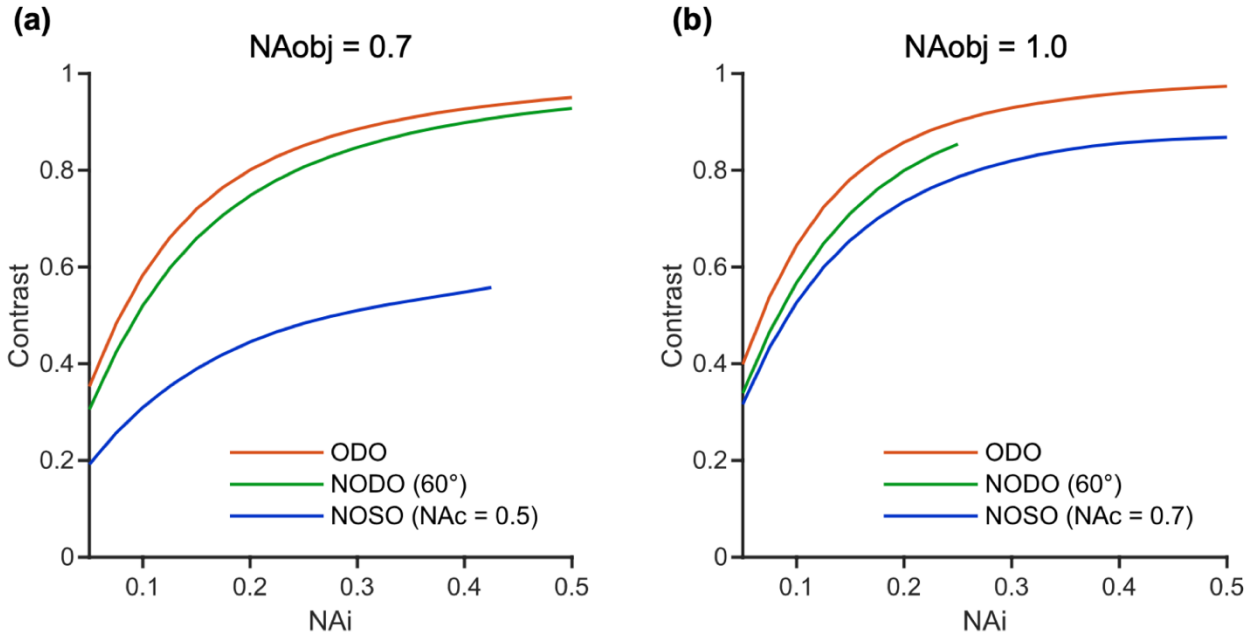


Figure 2.9. Comparison of contrast for ODO, NODO (60° crossing angle), and NOSO systems that can be built using **(a)** a moderate-NA (0.7) primary objective and **(b)** a high-NA (1.0) primary objective (i.e., the collection objective for dual-

objective systems or the shared primary objective for single-objective systems). For simplicity, the effective collection NA is held constant for each NOSO curve (0.5 for the moderate-NA case and 0.7 for the high-NA case). For all systems, increasing the illumination NA improves contrast but offers diminishing returns at higher illumination NAs. The NOSO system provides poorer contrast than the ODO or NODO systems in the moderate-NA case, while all systems provide similar contrast in the high-NA case.

2.4 Discussion

We have identified several key trends in terms of the resolution and contrast of single- and dual-objective LSM systems for cleared-tissue imaging, which we believe will be valuable as a general guide for system designers. In particular, we evaluated three OTLS microscope architectures: a conventional ODO system, a conventional NOSO system, and a novel NODO system.

Regarding the resolution of these systems, there are four main observations.

(1) For dual-objective (ODO and NODO) systems, larger crossing angles improve axial resolution until around 60° (**Figure 2.4**).

(2) For all systems, axial resolution is significantly affected by illumination NA, with diminishing returns (nonlinear dependence) at higher illumination NAs (**Figure 2.5**).

(3) For dual-objective systems, lateral resolution is entirely determined by collection NA, meaning that axial and lateral resolution are decoupled from one another (**Figure 2.6**).

(4) For single-objective (NOSO) systems at moderate NA, axial and lateral resolution must trade off (**Figure 2.7**).

We also identified two trends regarding system contrast.

(1) For dual-objective systems, larger crossing angles improve contrast until around 60° (**Figure 2.8**).

(2) Contrast for all systems improves with illumination NA, with diminishing returns (nonlinear dependence) at the highest illumination NAs, and dual-objective systems exhibit better contrast than single-objective systems when the same moderate-NA objective is used (**Figure 2.9**).

Collectively, these observations indicate that rather than one design being universally superior to another, there are specific benefits and drawbacks to each configuration depending upon the application.

There are a number of pros and cons for a NODO system. From a practical standpoint, a NODO system allows the full working distance and full NA of a collection objective to be utilized (see Appendix A.6 for further analysis of working distance between different configurations). The collection objective should ideally be oriented normal to a horizontal sample holder/interface, where refractive aberrations and index-matching requirements are minimized with modern well-corrected objectives. However, similar to a NOSO system, NODO requires a strategy to image a highly oblique non-orthogonal light sheet onto a camera chip (typically flat), such as by re-imaging a tilted remote focus. This adds a degree of optical complexity absent from an ODO system (though the remote focus does not limit performance to the extent it does in a NOSO system). Rapid time-lapse imaging of a localized 3D volume is also more challenging in a NODO system than in a NOSO system, making it less ideal for dynamic live-tissue imaging applications. Additionally, the use of multiple objectives means that, unlike a NOSO system, a NODO system cannot be easily integrated into a commercial widefield or confocal microscope.

Our quantitative analysis reveals several important aspects of NODO optical performance. For example, the NODO system (with ∼60° crossing angle) provides axial resolution comparable to an ODO system. Like an ODO system, the NODO system would require matched illumination and collection objectives to achieve isotropic resolution. However, using an illumination NA less than the collection NA offers similar resolution and contrast performance (**Figure 2.5** and **Figure 2.9**) but with the simplicity and geometric flexibility that a lower-NA illumination arm can offer, which may be most ideal for many applications. Image contrast for a NODO system is also comparable to an ODO system and better than a NOSO system. In addition, the NODO architecture decouples axial and lateral resolution, giving the designer more flexibility than a NOSO system.

To be clear, a 60° NODO system does exhibit slightly poorer performance, in terms of both resolution and contrast, than an ODO system. However, the loss in performance is modest (compared to the loss in performance if the crossing angle is reduced below 60°) and enables OTLS designers to realize the practical advantages of the NODO configuration (orthogonal placement of the collection objective with respect to the specimen surface). For some applications, this may be a desirable tradeoff.

It is important to note that the NODO design described here has some mechanical similarities to light sheet theta microscopy (LSTM), with both designs featuring a perpendicular collection objective and angled, non-orthogonal light sheet(s) [39]. Instead of using a remote focus to bring an entire 2D image into focus at the camera, LSTM only captures fluorescence from the central row of pixels (at the beam waist of the light sheet) in a manner similar to line-scanned dual-axis confocal (LS-DAC) microscopy [52,65,66]. This improves axial resolution slightly, as only the absolute thinnest part of the light sheet is used for imaging, but requires complicated mechanical scanning in order to align and synchronize the focus of the light sheet with the focal plane of the

detection objective and the rolling shutter of the camera. The LSTM design is also not as optically efficient compared to most LSM systems since most of the excited fluorescence is rejected by the sCMOS rolling shutter.

The advantages of the NODO architecture are most impactful for moderate-NA imaging systems. For low-NA systems, an ODO system is generally sufficient: long working-distance objectives and minimal off-axis aberrations mean that the complexities of a NODO architecture (e.g., having a tilted remote focus) are not warranted. At high NAs, a NOSO system allows the illumination and collection beams to have relatively large cone angles and crossing angles, which results in acceptable levels of resolution and contrast. However, as with any high-resolution (high-NA) system, the working distance and field of view of such a system will be limited, and imaging speeds will be slow. Finally, for moderate-NA systems (i.e., $0.5 < NA < 0.8$), the NODO architecture offers a combination of imaging performance (resolution and contrast), working distance, and field of view that is challenging to achieve with other architectures.

In summary, we have performed a quantitative analysis of how several key design parameters affect the performance of various OTLS microscope architectures. Our analysis reveals regimes in which various architectures are most ideal, and also shows that a NODO configuration may offer benefits for addressing cleared-tissue imaging applications where moderate spatial resolution is desired.

2.5 Acknowledgements

I would like to thank Adam K. Glaser and Jonathan T. C. Liu (co-authors on the published version of this chapter) who were instrumental in the stimulation study presented here.

The work in this chapter was supported by funding from the National Institutes of Health (NIH): R01CA175391 (J.T.C.L.) and K99CA240681 (A.K.G.); the National Science Foundation

(NSF): NSF Graduate Research Fellowship DGE-1762114 (K.W.B.); and the Department of Defense (DoD) Prostate Cancer Research Program: W81XWH-18-10358 (J.T.C.L). Any opinions, findings, and conclusions or recommendations expressed in this material are those of the authors and do not necessarily reflect the views of the NSF, NIH, or DoD.

Chapter 3. Axially swept open-top light-sheet microscopy for densely labeled clinical specimens

The work in this chapter was published in *Optics Letters* (Bishop et al. 2024) [31] and is reprinted with permission. © 2024 Optica Publishing Group

3.1 Introduction

Open-top light-sheet (OTLS) microscopy is an emerging technique for high-speed volumetric imaging of optically cleared tissues [26–30]. In an OTLS configuration, tissues are imaged through a transparent sample holder from below, similar to a flatbed document scanner. Placing the illumination and collection objectives beneath the tissue alleviates several sample-mounting constraints present in conventional (e.g., cuvette-based) light-sheet microscopes, allowing samples of arbitrary lateral size and shape to be easily imaged.

OTLS microscopy has enabled nondestructive 3D pathology, which offers several benefits over conventional slide-based histology. These include analyzing complex tissue structures in their native 3D context and sampling orders-of-magnitude more tissue than standard histology while preserving tissues for downstream assays [3]. With 3D pathology, specimens are often labeled with small-molecule stains, such as fluorescent analogs of hematoxylin and eosin (H&E) that broadly target cell nuclei (H) and proteins (E). This results in dense labeling compared to tissues labeled with highly targeted stains (e.g., neurons, vessels).

In densely labeled tissues, tight optical sectioning (high axial resolution) is helpful to minimize out-of-focus background signal for high-contrast imaging. Axial resolution can be improved by increasing the numerical aperture (NA) of the illumination light sheet. However, this reduces the field of view (FOV) and volumetric tile size (**Figure B.1**), as the depth of focus of a Gaussian light sheet is proportional to $1/NA^2$ (**Figure 3.1**a-b) [32]. Fusing many small tiles together is computationally intensive and can be error prone.

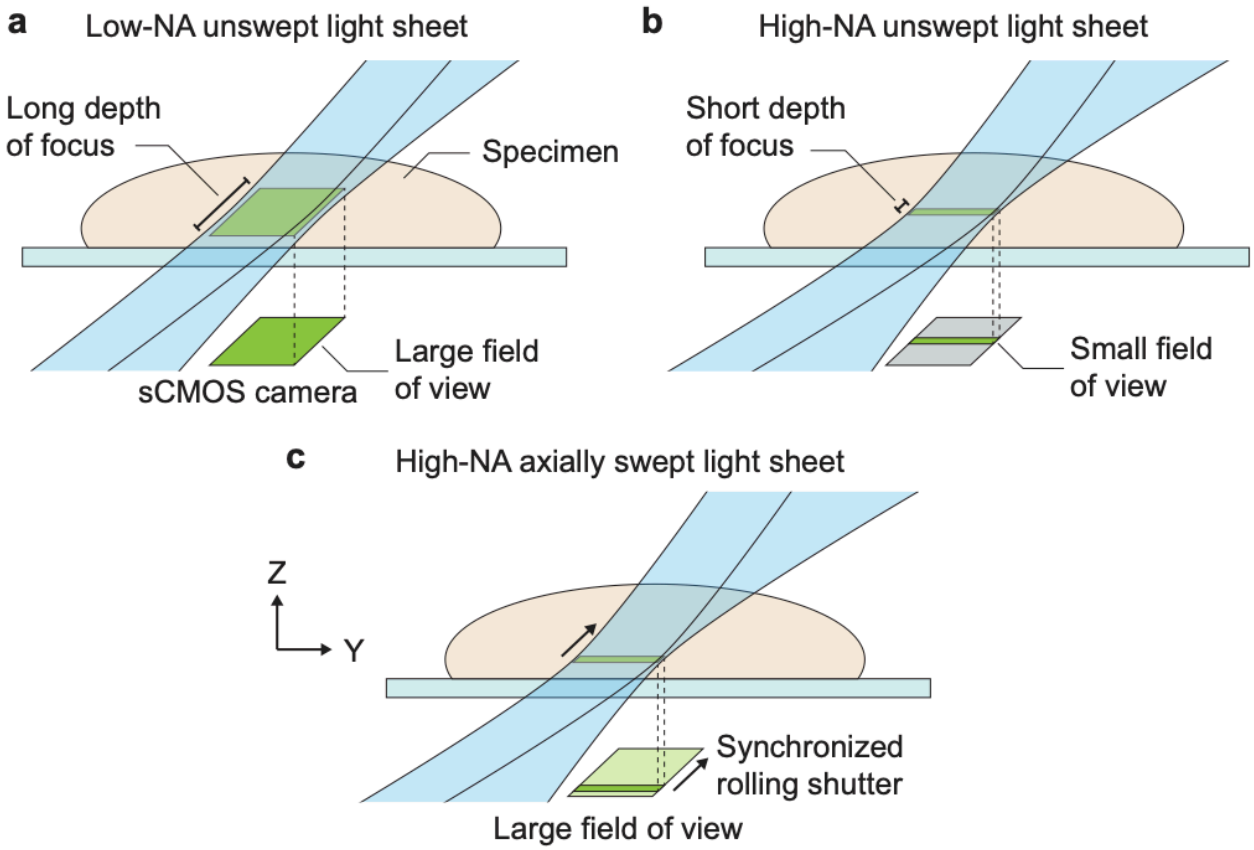


Figure 3.1. Open-top light-sheet (OTLS) systems using **(a)** a low-NA unswept illumination light sheet providing a large FOV (green) on the camera, **(b)** a high-NA unswept light sheet that underfills the camera due to the reduced depth of focus, and **(c)** a high-NA light sheet that is swept in synchrony with the rolling shutter to recover a large FOV.

Axially swept light-sheet microscopy (ASLM) circumvents the tradeoff between axial resolution and FOV [55]. In ASLM, the beam waist of a high-NA illumination light sheet is scanned along its optical axis in sync with the rolling shutter of an sCMOS camera, which images the light-sheet-generated fluorescence signal from an orthogonal direction. By synchronizing the exposed pixel rows to the thinnest part of the light sheet while scanning, ASLM can image large effective FOVs with high axial resolution (**Figure 3.1**c). One important tradeoff is that ASLM reduces a system's sensitivity, as each row of pixels on the camera is only active for a fraction of the total exposure time. However, 3D pathology applications of OTLS are not typically signal-limited due to the use of bright exogenous fluorophores and abundant labeling.

A detailed review of ASLM has been provided recently [67]. In summary, initial ASLM implementations used a remote-focusing method to sweep the illumination beam without introducing aberrations [55,62]. While advantageous for high illumination NAs (>0.4), this strategy adds significant optical complexity with fewer benefits at the moderate resolution levels most relevant for 3D pathology. Several simpler ASLM methods based on electrically tunable lenses (ETLs) have been shown [68], though high-speed scanning of ETLs is difficult to achieve and may require custom drive electronics [69]. Typical ETLs also present practical challenges, such as requiring vertical mounting to mitigate gravity-induced deformation and poor transmission at short illumination wavelengths (≤ 405 nm). Piezo actuators can overcome speed limitations of ETLs but are typically limited in scan range and are best suited for imaging small FOVs at high resolution. Voice coil actuators are an appealing alternative, and have been shown to offer a compromise between speed and scan range for ASLM [70].

Some initial work has demonstrated the utility of axial sweeping in OTLS systems [71,72]. While promising, these examples use an orthogonal dual-objective (ODO) arrangement that has a limited effective working distance (<2 mm) and high sensitivity to refractive index mismatches, both of which complicate imaging of large clinical specimens [30,32]. Here we demonstrate a simple axial sweeping method in which a lens is scanned by a high-speed voice coil actuator without remote focusing optics. We implement our method in a recently developed non-orthogonal dual-objective (NODO) architecture ideal for imaging large clinical tissues with a long working distance and low sensitivity to index mismatch [30,32].

3.2 Optical design

Our design consists of independent illumination and collection optical paths. A complete listing of components is provided in Table B.1. In the illumination arm (**Figure 3.2**a), a multi-wavelength (405, 488, 561, and 638 nm) fiber-coupled laser provides input light. Galvo mirrors approximately conjugate to the illumination objective's back focal plane provide fine adjustment of the light-sheet position at the sample. To axially sweep the beam, a high-speed voice-coil actuator scans an achromatic doublet lens (L_2). The axial magnification between the focal point of L_2 and the sample is 3.5×, such that scanning L_2 by ±1.32 mm scans the beam waist by ±375 μm at the sample, matching the full camera sensor size of 2048 × 2048 px (750 × 750 μm in the sample). We crop the sensor to 2048 × 1024 px (750 × 375 μm) here due to aberrations in the collection arm at the edges of the full FOV. This is not a fundamental limitation of the axial sweeping method, and different collection optics could utilize the full sensor. By adding a DC offset to the sinusoidal scanning waveform, the voice-coil also corrects defocus between wavelengths in multi-channel experiments.

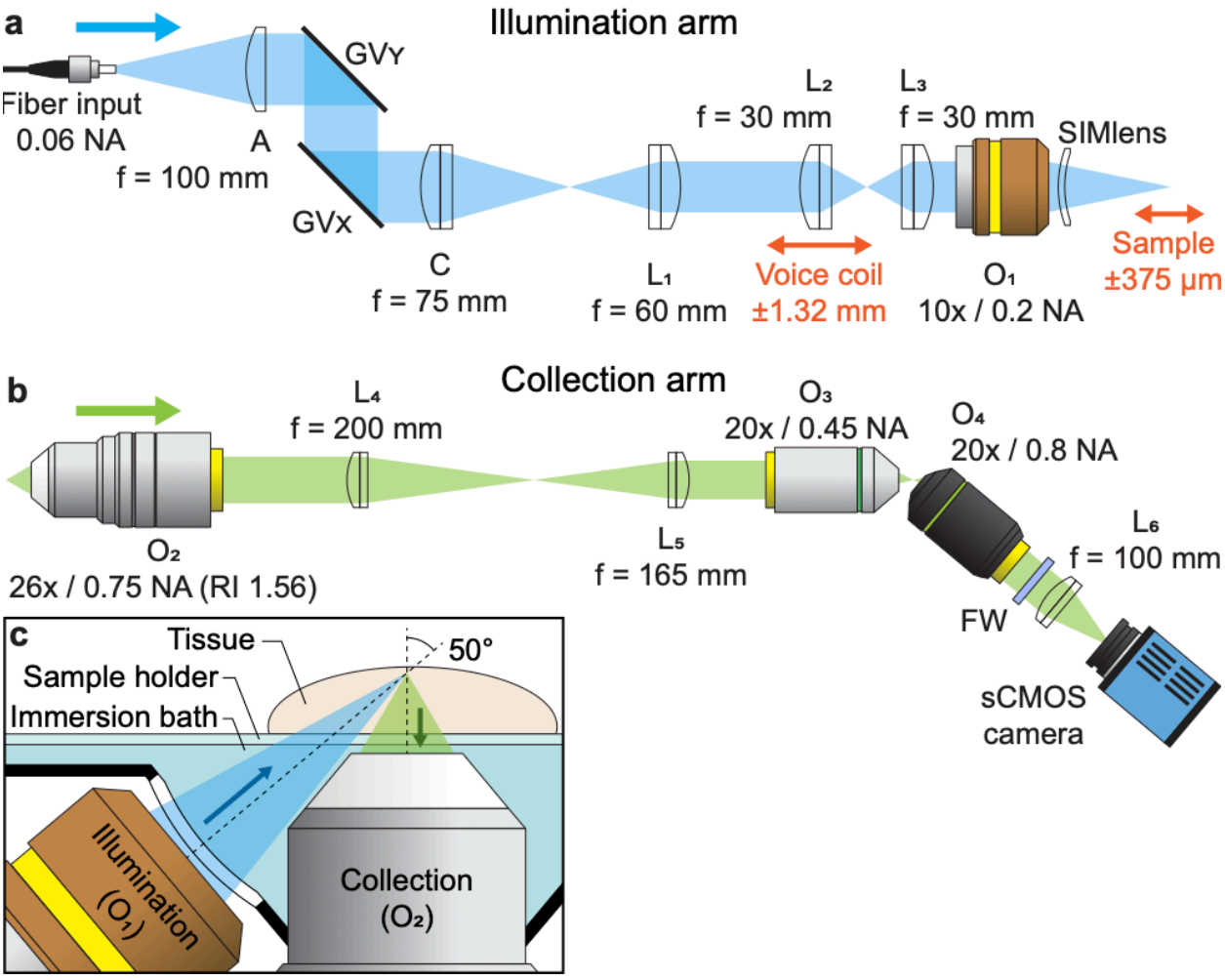


Figure 3.2. Optical layout of the illumination **(a)** and collection **(b)** arms. **(c)** Schematic of the optical arrangement near the sample. A: aspheric lens, $GV_{X/Y}$: galvo mirrors, C: cylindrical lens, $L_{1\text{-}6}$: spherical lenses, $O_{1\text{-}4}$: objectives, FW: filter wheel

The beam is finally relayed to a 10× / 0.2 NA air objective (O_1), which is paired with a custom-designed SIMlens [73]. The SIMlens is a wavefront-matching element allowing the air illumination objective to be used in an immersion configuration with minimal aberrations at the air/glass/liquid interfaces. The SIMlens also increases the beam's NA by a factor of the immersion index, for an effective illumination NA of 0.312 for the ethyl cinnamate (ECi, n = 1.56) immersion

used here. A ray-trace simulation of the illumination arm was performed in Zemax OpticStudio to validate the optical design and axial-sweeping mechanism (**Figure B.2**).

The collection arm (**Figure 3.2**b) uses a non-orthogonal dual-objective (NODO) OTLS configuration described previously [30,32]. Briefly, a primary collection objective (O_2) is oriented vertically and perpendicular to the planar sample holder, while the illumination objective (O_1) is oriented at 50° relative to the vertical axis to deliver a tilted light sheet (**Figure 3.2**c). The vertical arrangement of O_2 minimizes aberrations introduced by index mismatches between the immersion liquid, sample holder, and tissue, as well as allowing the objective's full 10-mm working distance to be used.

The tilted sample plane is relayed to a remote focal plane (between O_3 and O_4) with optics selected to provide a 1:1 spatial mapping of the light sheet from the sample to the remote focus, which minimizes distortions and aberrations [58]. A final 20× / 0.8 NA air objective (O_4) and tube lens (L_6) are oriented orthogonal to the remote-focus replica of the light sheet, which is imaged onto an sCMOS camera. A coverslip was glued to O_4 by Applied Scientific Instrumentation for high-quality imaging with this coverslip-corrected objective. Note that compared to our previous design [30], we use a lower-magnification remote objective (O_4) in order to increase the FOV and volumetric imaging speed (750 x 375 μm here compared to 340 x 40 μm previously, or a 20-fold increase in area). This results in a reduced effective collection NA compared to the full NA of the primary objective, O_2 (0.53 here compared to 0.7 previously).

3.3 Results & discussion

To measure the system's resolution, we imaged 150-nm diffraction-limited gold nanoparticles embedded in a 3D agarose phantom index-matched to ECi [74]. The beads were imaged at 638 nm in scattering mode (i.e., no emission filter). We used a custom Python script to identify beads in

the imaging volume and fit a 3D Gaussian point spread function (PSF) to each bead [74]. The resolution, defined as the PSF full width at half maximum (FWHM) in each dimension, was 1.13±0.48 μm in the x-dimension, 1.10±0.38 μm in the y-dimension, and 2.01±0.75 μm in the z-dimension (median ± standard deviation across the imaging volume). The z-resolution is slightly worse than the theoretical limit due to minor aberrations and the impact of the collection arm optics on the system PSF [32]. Here, the x- and y-axes lie in the plane of the sample holder, and the z-axis is perpendicular to the sample holder (**Figure 3.1**).

We compared bead datasets collected from the same system with and without axial sweeping (**Figure 3.3**). Each bead's position in the plot corresponds to its location within the FOV, and the bead's color indicates the FWHM in the z-dimension (axial resolution). In the unswept case (**Figure 3.3**a), the axial resolution deteriorates rapidly as a function of distance from the light-sheet beam waist at the center of the FOV. Far from the beam waist, the axial resolution is dominated by the collection objective's depth of focus (O_2) rather than the light sheet thickness, causing the FWHM to reach a plateau. In the swept case (**Figure 3.3**b), the beam waist moves across the FOV in synchrony with the camera's rolling shutter, resulting in uniform axial resolution.

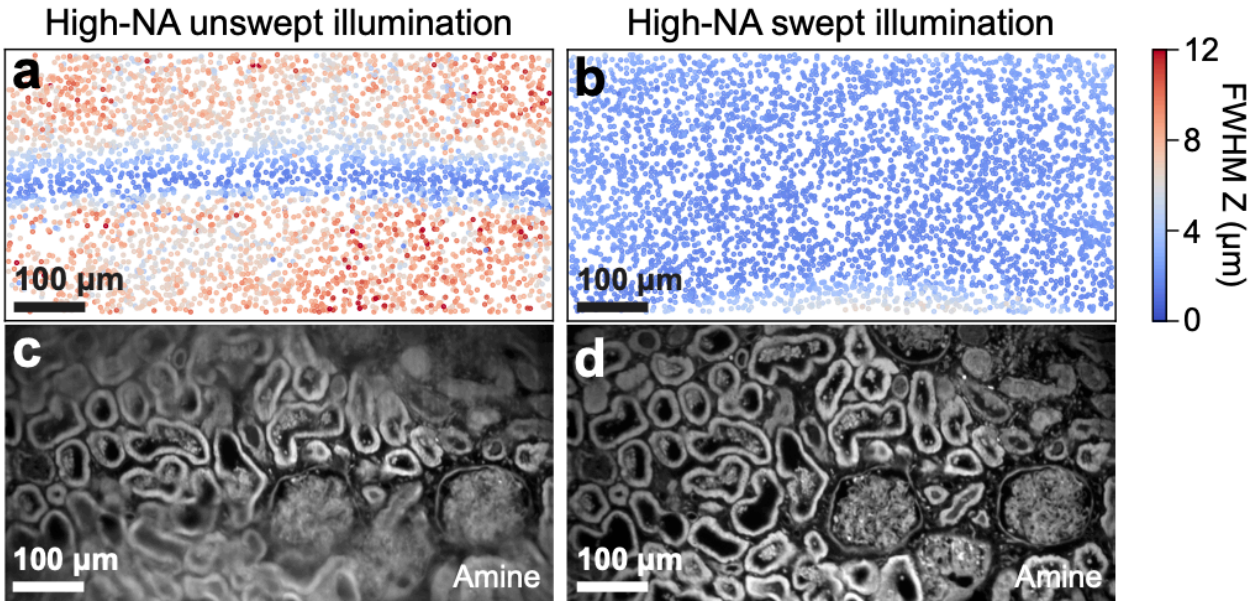


Figure 3.3. (a-b) Axial PSF measurements from a bead phantom with and without axial sweeping across the FOV. **(c-d)** One camera frame of a human kidney (FLARE amine stain) with and without sweeping, demonstrating an increased usable FOV.

To evaluate the impact of axial sweeping in tissue, we captured the same FOV from a human kidney specimen with axial sweeping turned on and off. The kidney was labeled using the fluorescent labeling of abundant reactive entities (FLARE) protocol and cleared in ECi [75]. The amine stain, which labels proteins (638 nm channel), is shown in **Figure 3.3**. Without axial sweeping, poor optical sectioning away from the beam waist degrades the image quality (**Figure 3.3**c), while axial sweeping provides tight optical sectioning across the FOV (**Figure 3.3**d). Axial sweeping also reduces shadowing artifacts (vertical stripes) that are visible in the unswept case, a known challenge in static light-sheet systems [76].

Finally, we compared the microscope to another NODO OTLS system in our lab that uses low-NA illumination without axial sweeping [30] (**Figure 3.4**). The unswept system has a measured axial resolution (FWHM of diffraction-limited beads) of 3.67±0.58 µm (median ±

standard deviation) over a 2048 × 256 px (750 × 94 μm) FOV. The two systems have identical collection arms (i.e., identical lateral resolution), enabling a controlled comparison between a system with and without axial sweeping. We imaged the same human prostate specimen on each system. The specimen was labeled with a fluorescent analog of H&E staining using TO-PRO-3 (638 nm channel) and eosin (561 nm channel) along with ECi clearing [74].

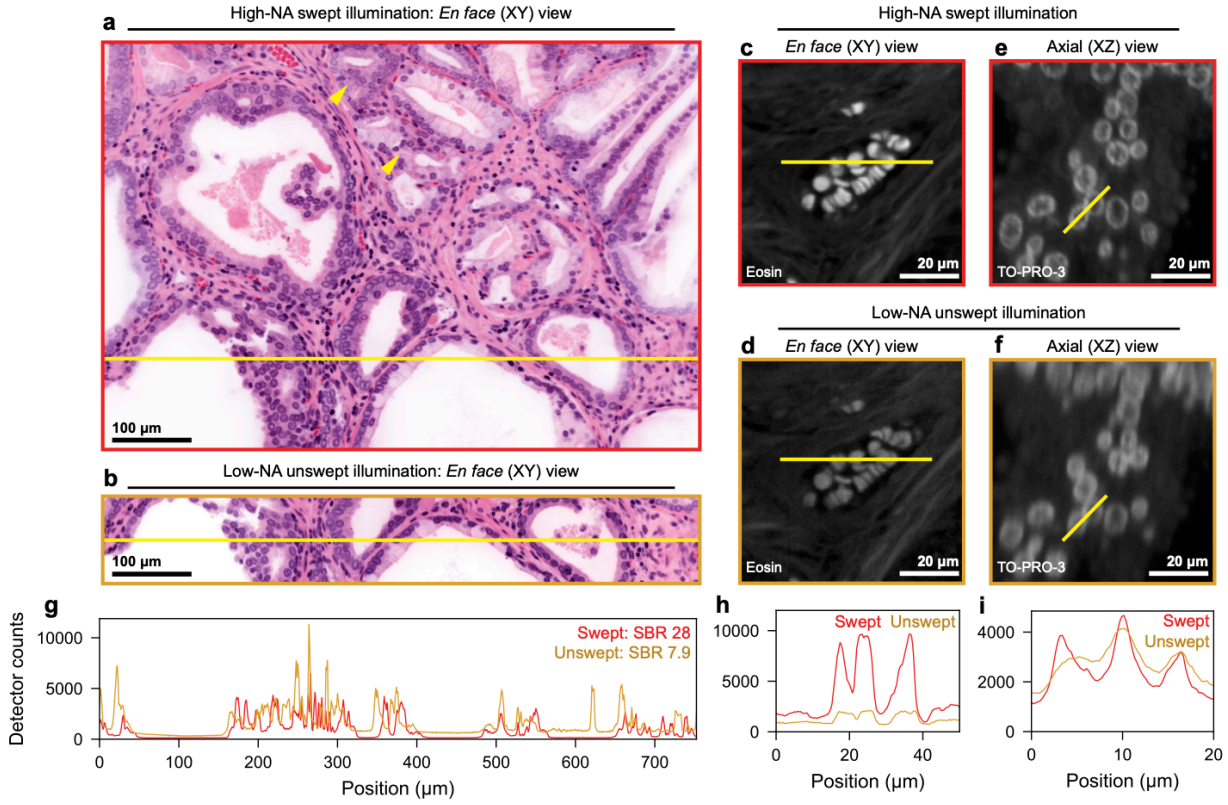


Figure 3.4. 3D dataset of a human prostate specimen stained with a fluorescent analog of H&E and imaged with both a high-NA swept illumination light sheet and low-NA unswept light sheet. **(a-b)** *En face* views (XY cross section) false-colored to mimic conventional H&E staining show fused glands indicative of Gleason pattern 4 carcinoma, arrows in (a). **(c-d)** Zoomed views of the cytoplasm channel show improved contrast and separation of red blood cells with axial sweeping. **(e-f)** Axial views (XZ cross section) from the nuclear channel show improved contrast and axial resolution (sharper peaks) with axial sweeping. Line intensity profiles **(g)**

from the nuclear channel of (a-b), **(h)** from the cytoplasm channel of (c-d), and **(i)** from the nuclear channel of (e-f).

En face (XY) views from the volumetric dataset captured with the high-NA, axially swept illumination system and low-NA, unswept illumination system are shown in **Figure 3.4**a-b (recolored with FalseColor-Python to mimic the appearance of conventional H&E staining [77]). Zoomed regions show *en face* (XY) views of red blood cells in the eosin channel (**Figure 3.4**c-d) and orthogonal axial (XZ) views of cell nuclei in the TO-PRO-3 channel (**Figure 3.4**e-f). Intensity line profiles comparing the same regions in both datasets demonstrate improved signal-to-background ratio (SBR), contrast, and axial resolution with axial sweeping (**Figure 3.4**g-i).

In terms of imaging speed, the high-NA swept system described here (2048 × 1024 px frames) runs at 17 frames per second (fps), while the low-NA unswept system (2048 × 256 px frames) runs at 100 fps (50% faster in terms of data output rate). However, the swept system requires fewer overlapping seams (redundant imaging) due to larger volumetric tiles, reducing stitching artifacts and computational time for fusing the 3D datasets. Note that the speed of both systems is currently limited by computational bottlenecks (camera data transfer and disk writing speeds) rather than fundamental hardware limits – we have demonstrated stable axial sweeping rates of up to 50 Hz.

In summary, we have developed a NODO OTLS system with rapid axial sweeping that provides improved optical sectioning in comparison to our previous OTLS systems, resulting in higher image quality in densely labeled specimens. In addition to the OTLS implementation targeted here, our straightforward axial sweeping method holds potential value for other light-sheet microscope architectures (e.g., for dynamic sample imaging) where high-speed, large FOV imaging is needed.

3.4 Acknowledgements

I would like to thank the following individuals (co-authors on the published version of this chapter) who were instrumental in the development the axially swept open-top light-sheet microscope: Lindsey A. Erion Barner, Elena Baraznenok, Lydia Lan, Chetan Poudel, David Brenes, Robert B. Serafin, Lawrence D. True, Joshua C. Vaughan, Adam K. Glaser, and Jonathan T. C. Liu.

The work in this chapter was supported by funding from the National Institutes of Health (NIH): R01EB031002 and R01CA268207 (J.T.C.L), and the Indiana Center for Advanced Renal Microscopy and Molecular Imaging U54DK137328 (J.C.V. and J.T.C.L.); the National Science Foundation (NSF): NSF Graduate Research Fellowships DGE-1762114 (K.W.B. and L.A.E.B.); and a Washington Research Foundation Postdoctoral Fellowship (C.P.). Any opinions, findings, and conclusions or recommendations expressed here are those of the authors and do not necessarily reflect the views of the NSF or NIH.

Finally, I would like to thank Priti Lal for assistance in acquiring some tissue specimens shown in this chapter and Carol Borsa at Thorlabs for helpful technical advice.

Chapter 4. An end-to-end workflow for nondestructive 3D pathology

The work in this chapter was published in *Nature Protocols* (Bishop et al. 2024) [74] and is reproduced with permission from Springer Nature. © 2024.

4.1 Introduction

Anatomic pathology, which entails the microscopic analysis of biological tissues, is often regarded as the gold standard for clinical diagnostics/prognostics and for many preclinical studies. While conventional slide-based 2D histology remains the most widespread approach for high-

resolution interrogation of tissue specimens, 3D pathology of intact tissues is gaining attention for both research applications and potential clinical assays [2,3]. Compared to conventional pathology, 3D pathology interrogates orders-of-magnitude more tissue and provides a feature-rich volumetric context for complex tissue morphologies, all without destructive tissue sectioning. This novel volumetric "big data" has the potential to improve diagnostic sensitivity and accuracy, prognostication of patient outcomes, and prediction of treatment response in comparison to 2D pathology, with the ultimate goal of improving clinical decisions for diverse individuals.

To accelerate the preclinical and clinical adoption of 3D pathology, well-controlled studies with large, curated sets of tissue specimens are needed. Here we present a comprehensive, end-to-end 3D pathology workflow termed Path3D to guide researchers in generating consistent, high-quality 3D-pathology datasets, with a focus on large-scale clinical and preclinical studies.

4.1.1 Development of the protocol

A variety of approaches have been developed for staining, imaging, and visualizing pathology specimens in 3D with impressive proof-of-concept results [2,3]. However, consistently generating high-quality 3D pathology datasets across hundreds of samples for large-scale clinical studies is nontrivial, requiring refined protocols for tissue preparation, imaging, data processing, and quality control. Generating reliable data is complicated by the fact that no general microscopy end-user can be expected to be an expert in all stages of this cross-disciplinary pipeline. Therefore, a comprehensive and detailed protocol that can be implemented by general researchers would be of value. In addition to the technical workflow requirements (image resolution, dye selection, etc.), key practical requirements include quality control, throughput/ease-of-use for hundreds of specimens, and a visualization format that is familiar to researchers and clinicians. Here we attempt to address these requirements and to provide a drop-in alternative to conventional 2D histology.

Our protocol is designed for formalin-fixed (FF) or formalin-fixed paraffin-embedded (FFPE) tissues, which describes the vast majority of archived clinical specimens. The final output of the workflow described here is a 3D dataset that can be viewed as a stack of 2D images by pathologists/researchers and that can optionally be false colored to match the appearance of standard hematoxylin and eosin (H&E) histology to facilitate interpretation. While we do not discuss downstream image-processing and computational-analysis workflows, which will vary greatly between end-users, the H&E-analogue 3D datasets generated by our protocol are also an ideal starting point for many of these computational efforts [9,78,79].

Our Path3D protocol includes four main sections (**Figure 4.1** and overview in Video S1, available online in reference [74]): (I) tissue preparation (staining and optical clearing), (II) 3D microscopy, (III) data processing, and (IV) quality control. The first three sections generate the initial datasets, which can mimic the appearance of standard H&E images if helpful (**Figure 4.2**). The last section ensures high-quality results in large-scale studies and provides feedback for iterative parameter optimization within the first three sections, as is often needed during the early stages of a project. Path3D uses a relatively fast labelling and clearing method (a few days from start to finish) that can be reliably carried out by a student (including advanced undergraduates) or research technician. In summary, Path3D enables well-controlled clinical or preclinical studies where consistent, high-throughput 3D pathology datasets are needed for tens to hundreds of specimens.

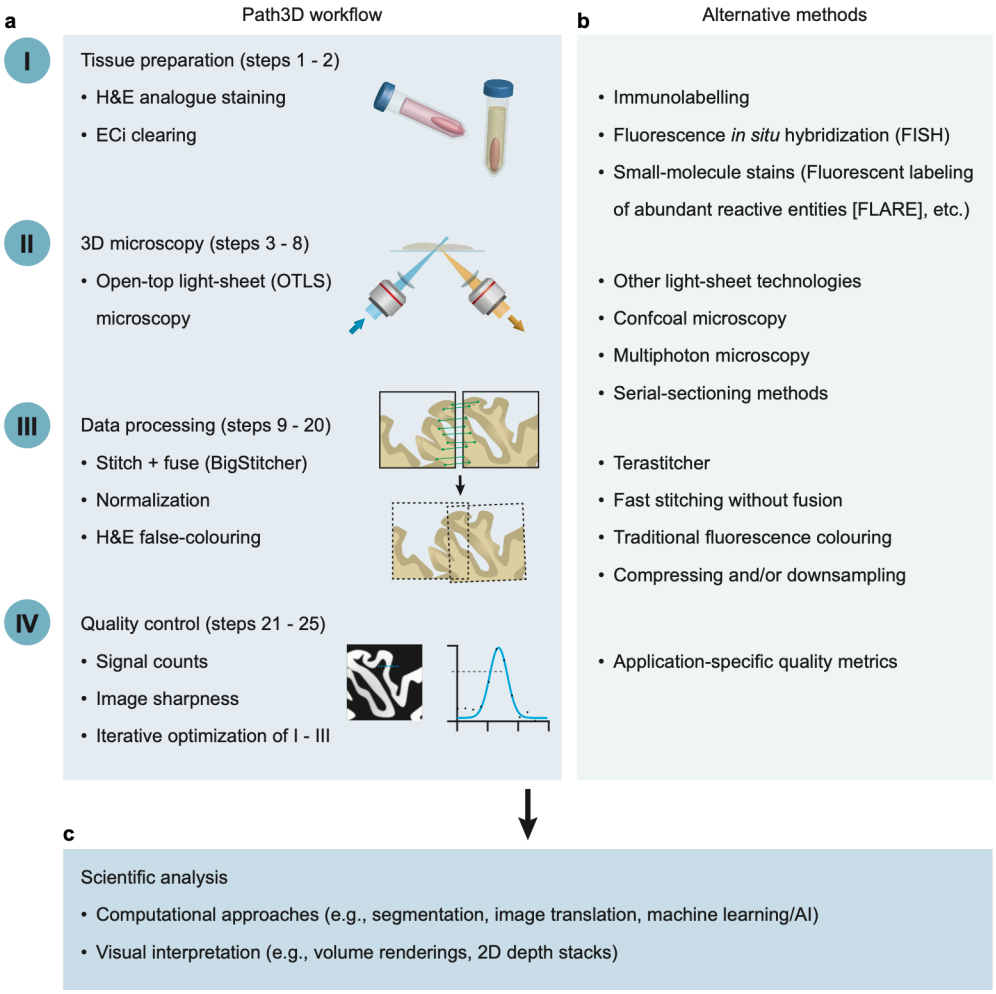


Figure 4.1. (a) Flowchart showing the four key sections to the Path3D workflow: tissue preparation, 3D microscopy, data processing and quality control. Iterative optimization is essential for producing consistent and high-quality datasets. **(b)** Each section of the standard Path3D protocol can be adapted on the basis of the needs of a specific application. **(c)** Path3D datasets are suitable for a range of scientific analyses based on computational analysis, visual interpretation or a combination of the two. AI, artificial intelligence; ECi, ethyl cinnamate.

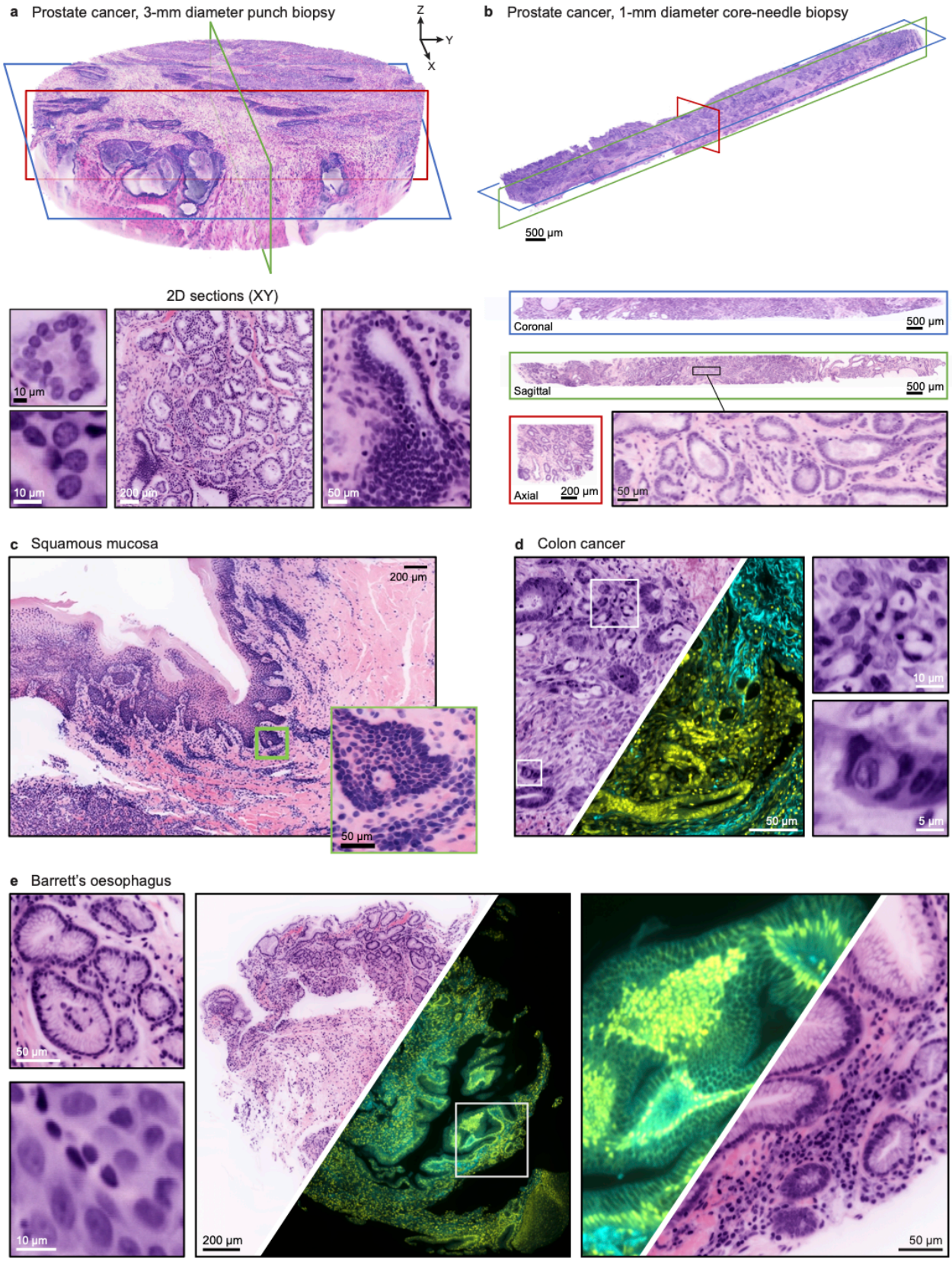

a Prostate cancer, 3-mm diameter punch biopsy
Z
Y
X
b Prostate cancer, 1-mm diameter core-needle biopsy
500 µm
2D sections (XY)
10 µm
10 µm
200 µm
50 µm
Coronal
500 µm
Sagittal
500 µm
Axial
200 µm
50 µm
c Squamous mucosa
200 µm
50 µm
d Colon cancer
10 µm
50 µm
5 µm
e Barrett's oesophagus
50 µm
10 µm
200 µm
50 µm

Figure 4.2. (a) 3D rendering (produced using Imaris) and *en face* 2D cross sections of a 3-mm-diameter punch biopsy of prostate cancer tissue (FFPE) false-colored to mimic the appearance of standard H&E staining. **(b)** 3D rendering (produced using Imaris) and orthogonal 2D cross sections of a 1-mm-diameter core-needle biopsy of prostate cancer tissue false colored to mimic the appearance of standard H&E staining. **(c)** 2D cross section of squamous mucosal tissue false colored to mimic the appearance of standard H&E staining. **(d)** 2D cross section of colon cancer tissue shown with both H&E false coloring and standard fluorescence coloring. **(e)** 2D cross section of esophagus tissue (Barrett's esophagus) shown with both H&E false coloring and standard fluorescence coloring. Images are shown with a standard sharpening filter. Panel (c) adapted from reference [77] under Creative Commons license CC BY 4.0.

4.1.2 Protocol overview

The initial tissue-processing steps (**Figure 4.3**) of Path3D are designed to mimic the traditional H&E stain while making the tissue transparent (optically clear) for high-throughput volumetric microscopy. The traditional absorption-based H&E stain for 2D histology offers general-purpose contrast by combining hematoxylin, which stains negatively charged DNA (i.e., nuclei) with a purple hue, and eosin, which stains positively charged proteins (i.e., cytoplasm and extracellular matrix) with a pink hue. To provide a fluorescent analogue of standard H&E for 3D microscopy, Path3D likewise uses both a nuclear dye (TO-PRO-3) and a cytoplasmic dye (eosin, which is naturally fluorescent). The use of small molecule dyes is essential for efficient penetration into thick tissues. After tissue staining, optical clearing is used to render thick specimens optically transparent by homogenizing the refractive index within each sample, thereby enabling fluorescence imaging deep within the tissue. Path3D is optimized for tissue clearing with ethyl cinnamate (ECi) [80], a solvent-based protocol similar to immunolabeling-enabled three-

dimensional imaging of solvent-cleared organs (iDISCO) methods [81,82]. Ethyl cinnamate clearing is relatively simple and uses nontoxic reagents.

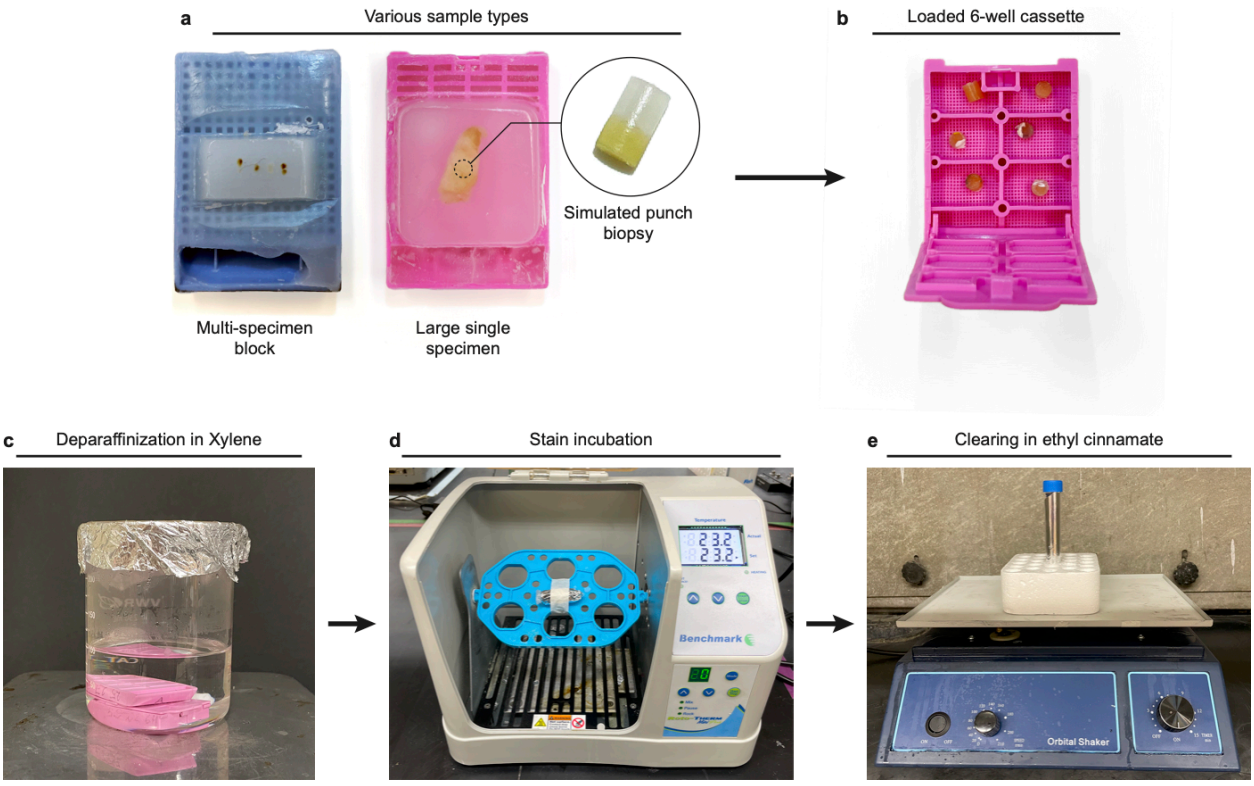


Figure 4.3. (a) Various sample types, including common archival specimens such as multi-specimen blocks, large single specimens and punch biopsies, can be used with Path3D. **(b)** Tissue punches are loaded into six-well cassettes for deparaffinization (Step 1A). **(c)** Cassettes are incubated in xylene on a hot plate with a magnetic stir bar (Step 1B). **(d)** Biopsies are individually incubated in the staining solution in a Roto-Therm rotator (Step 2B). **(e)** Biopsies are individually cleared by incubating in ECi on an orbital shaker (Step 2D).

Following tissue processing, samples are imaged with non-destructive 3D microscopy. Light-sheet microscopy (also known as selective plane illumination microscopy [SPIM]) is an ideal platform for high-throughput 3D pathology, enabling rapid and gentle imaging of cleared

specimens. We initially developed Path3D for use with open-top light-sheet (OTLS) microscopy. In an OTLS architecture, illumination and collection optics are placed below a planar sample holder such that specimens are imaged from below, much like a flatbed document scanner. This approach is specifically optimized for pathology specimens of arbitrary size and shape [25–30]. Many other custom-built light-sheet systems exist [24,83–85], as do a number of commercial options (e.g., SmartSPIM, Leica SP8, Zeiss Lightsheet 7, Luxendo LCS SPIM/MuVi SPIM, Olympus/PhaseView Alpha3, 3i Cleared Tissue LightSheet). Of particular note are single-objective light-sheet variants, which maintain a similar open-top geometry [41–43,45–47,49,86–89]. We use light-sheet microscopy in this protocol to illustrate key imaging considerations. However, our pipeline is in principle applicable to other 3D microscopy platforms (e.g., confocal microscopy, multi-photon microscopy). Further discussion of imaging platforms is provided in the 'Comparison with other methods' section. We provide strategies to establish the baseline performance of each microscope system for a given clearing protocol using 3D phantoms of diffraction-limited beads and an automated method to quantify a microscope's point spread function (PSF, adapted from a method developed by Sofroniew [https://github.com/sofroniewn/psf], which is key for later quality control and troubleshooting (**Figure 4.4**). We also offer guidelines for establishing ideal imaging conditions (considering detector counts, photobleaching, etc.).

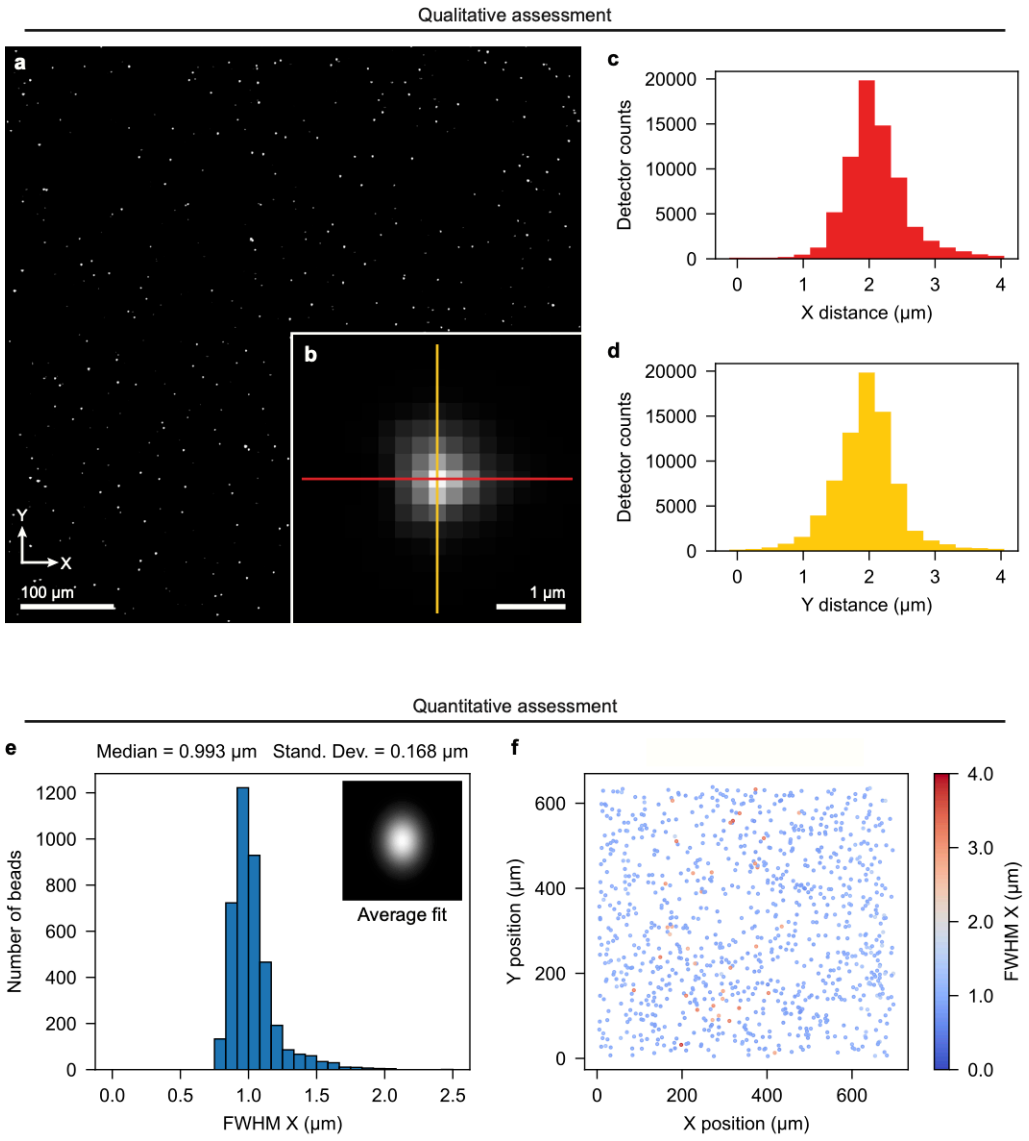


Figure 4.4 Initially, agarose bead phantoms are qualitatively assessed in real time while being previewed to optimize the focus and alignment of the microscope (Step 5). **(a)** An example bead image (single slice) shows the relative bead density. Line profiles of a well-focused bead, **(b)**, in the *X*, **(c)**, and *Y*, **(d)**, directions show symmetric Gaussian profiles with peak detector counts well above the background level. After imaging a 3D volume, the Bead_PSF_computation package is used to quantify the full width at half maximum (FWHM) values for each bead (Step 6). **(e)** A histogram of lateral (*X*) FWHM values from all beads acquired with a well-aligned microscope shows a distribution centered near the expected resolution with minimal spread. The inset shows an *XY* slice of the average 3D Gaussian curve

fit. **(f)** A heat map from a well-aligned example shows consistent lateral resolution with respect to the *X* and *Y* position within the imaged volume. A perceptually uniform diverging colormap [90] (Matplotlib [91], 'coolwarm') is intentionally used to accentuate regions of particularly poor resolution. See **Figure C.4** for additional details on heat maps.

For data processing and visualization, we focus on a fully open-source approach that can be performed by researchers with basic programming skills in Python. For nearly all 3D microscopy platforms, volumetric datasets of millimeter- to centimeter-scale tissues are first acquired by scanning the specimen in one primary direction (vertical or horizontal) to generate a 3D tile (a "volumetric brick") of image data. Adjacent tiles are typically stitched and blended together to create a large contiguous volume before further image processing or visualization is performed. Various academic [92,93] and commercial options (e.g., Aivia [https://www.aivia-software.com], Imaris [https://imaris.oxinst.com], Stitchy [https://www.translucencebio.com/products/stitchy]) exist for reconstructing 3D volumes from adjacent tiles. Likewise, a number of file formats have been developed for storing 3D datasets including HDF5 [94], Zarr [95], OME-Zarr [96], and N5 [97]. This protocol utilizes an open-source method of aligning and reconstructing tiles ('stitching and fusion') using BigStitcher [98] with HDF5 [94], which can be run as a FIJI [99] plugin and requires minimal manual tuning of parameters.

Following reconstruction, datasets may be false colored to mimic the pink and purple appearance of standard H&E histology. While anatomic pathologists are skilled at interpreting chromogenic (absorption-based) H&E slides, most are not experienced with interpreting multi-channel greyscale or arbitrarily colored fluorescence images. A variety of false-coloring methods have been developed, including machine-learning-based style-transfer methods [100–104]. While these strategies are appealing to convert images from one contrast mechanism to another, such as

converting unstained whole slide images into H&E-like images [105], they require large amounts of training data and are often hard to generalize to new data types (e.g., imaging conditions or tissue types not represented in the training data). Because Path3D datasets contain direct fluorescent analogues to conventional hematoxylin and eosin, we prefer a deterministic physics-based approach that models the absorption of light by conventional H&E dyes [106]. The explainability of this digital staining strategy is particularly appealing in the context of clinical studies and adoption by pathologists. Our approach is implemented as an open-source Python package, FalseColor-Python [77].

Compared to viewing standard 2D whole-slide images, viewing and navigating 3D pathology datasets is not straightforward nor standardized. Many clinical or preclinical studies require interpretation of 3D datasets by panels of pathologists and researchers, so an easy-to-navigate visualization and annotation method is often desired. Here we offer guidance for using Napari, an open-source Python-based package for 3D image visualization (**Figure C.9**) [107]. In our experience, Napari provides relatively smooth and user-friendly visualization of 3D pathology data and offers built-in annotation features. Critically, Napari can dynamically load pyramidal file formats to minimize the amount of memory needed to navigate large 3D datasets. For users familiar with Python, Napari also offers additional analysis tools and freedom to write custom Python plugins. Other open-source visualization packages include QuPath [108], which is designed for digital pathology and is ideal for viewing individual 2D slices in a 3D dataset, and FIJI (ImageJ) [99], which is a widely used general-purpose tool for scientific image visualization. Commercial tools like Imaris [https://imaris.oxinst.com], Arivis [https://www.arivis.com], Aivia [https://www.aivia-software.com], and Amira [https://www.thermofisher.com/us/en/home/electron-microscopy/products/software-em-3d-

vis/amira-software.html] provide excellent volumetric (object rendering) as well as slice-by-slice visualization and annotation capabilities along with the professional technical support that many researchers value (**Figure 4.2**a-b; Video S1, available online in reference [74]). Recent academic studies have also explored novel methods for volumetric rendering and visualization of 3D pathology data, including augmented/virtual reality approaches [109,110]. For large studies with unique visualization requirements, custom interfaces (e.g., web-based) can also be developed.

Throughout the Path3D protocol, continuous dataset evaluation and iterative optimization are essential to ensure that datasets are of consistently high quality for large-scale clinical or preclinical studies. Quality control is intentionally included as a routine step in the protocol rather than as a supplementary option, and we offer quantitative methods to assess resolution, contrast, and uniformity. Finally, we provide rough recommendations for the level of data quality that is necessary to produce high-quality false-colored imaging results that meet pathologists' expectations. Our metrics also generally reflect the level of quality needed for effective downstream computational analyses. Note that in some cases, commercial imaging systems may improve consistency compared to custom instruments. Nonetheless, we suggest routine dataset evaluation as data quality can be impacted by every step of the process (tissue preparation, imaging, and data processing).

4.1.3 Applications and limitations

We have used Path3D to explore a number of clinical use cases for 3D pathology to date (**Figure 4.2**). For example, various iterations of the protocol have been used to examine and quantify the 3D morphology of prostate cancer specimens [27–30,73,77–79]. This includes a proof-of-concept demonstration that 3D pathology can reduce certain ambiguities when performing Gleason grading of prostate cancer (which heavily influences treatment

recommendations) [27] and preliminary studies showing that the computational segmentation and analysis of prostate glands and nuclei in 3D have advantages for risk stratification [78,79]. Recently, we used a variation of Path3D to image whole lymph nodes from breast cancer patients and demonstrated that 2D pathology can underrepresent metastasis size compared to comprehensive 3D pathology [8]. We have also leveraged Path3D to show that diagnosis with deep-learning-assisted 3D pathology can detect esophageal neoplasia with higher per-biopsy sensitivity than standard 2D histology while also reducing pathologist workloads [9]. Additionally, the protocol has been used to generate 3D image atlases for various tissue types and disease states [10,111]. Larger studies comparing 2D and 3D pathology are underway, considering both inter- and intra-observer variability and overall accuracy (i.e., pathological grade vs. clinical outcome), and there are abundant opportunities to explore additional clinical applications of 3D pathology. Finally, the Path3D protocol has enabled a variety of preclinical studies such as characterizing 3D mouse liver cell cultures for microfluidic drug screening [112], evaluating dissolvable microneedle arrays for transdermal drug delivery in mice, and imaging whole mouse kidneys at different scales to count and assess glomerular structure and function (**Figure C.1**c).

Manually reviewing 3D datasets using conventional workflows built around 2D slides can be labor-intensive, suggesting novel 3D-based review processes will be needed. Designing clinical studies that effectively use the large data volumes available from Path3D requires careful planning, and while not described here, computational analysis in conjunction with, or instead of, manual review is often appropriate. It is also critical to establish a robust data management plan, as raw datasets can be up to a terabyte (TB) in size (depending on image volume, resolution, etc.). Fortunately, there are many options for cloud-based storage and computational processing, which should be decreasing in cost over time. We have successfully used Path3D datasets for a number

of computational use cases including image translation and glandular segmentation [78], nuclear segmentation [79], and deep learning-based triage [9], and there are likewise opportunities to adapt computational techniques developed for 2D digital pathology to 3D datasets [113].

Regardless of the specific staining and clearing protocol used (TO-PRO-3/eosin and ECi here), our data-processing and false-coloring workflow can be applied to generate H&E-like images from any fluorescent dataset with distinct nuclear and cytoplasmic channels. For example, we have used SYTOX-G or propidium iodide and NHS-ester staining with clear, unobstructed brain imaging cocktails and computational analysis – histoVision (CUBIC-HV) clearing to generate false-colored 3D datasets of human lymph nodes (**Figure C.1**a) [8]. We have also combined ECi clearing with fluorescent labelling of abundant reactive entities (FLARE) staining as an H&E analogue [75]. Furthermore, we have shown that our workflow can be adapted for single-channel (acridine orange) datasets that are computationally separated into nuclear and cytoplasmic channels (**Figure C.1**b) [114]. Our focus here is on generating datasets that replicate standard H&E stains, the most commonly used by pathologists, meaning that Path3D datasets show tissue structure but do not on their own provide molecular information. However, we and others have shown that deep learning-based virtual-staining methods can be used to mimic certain targeted stains (e.g., immunolabeling) based on H&E-like datasets [78,101].

It is important to note that while conventional H&E slides can be reimaged indefinitely, Path3D specimens, like any fluorescently labelled tissue, are subject to eventual photobleaching. The exogenous dyes used here are relatively bright (compared to endogenous fluorescent proteins, for instance) and photobleaching during initial imaging rounds is usually not an issue for well-stained specimens imaged at modest illumination powers (a few milliwatts of optical power measured at the sample). Nonetheless, repeated imaging of the same region will eventually lead to

a significant drop in signal level. To avoid photobleaching valuable specimens with multiple redundant imaging rounds, it is important to ensure staining and imaging conditions are well-optimized before starting a large clinical study and that imaging regions are judiciously selected. While we have not attempted stripping and restaining Path3D specimens, previous reports suggest this may be possible [115,116].

4.1.4 Comparison with other methods

One alternative to non-destructive 3D microscopy of cleared tissues is automated serial-sectioning microscopy, in which thin tissue sections are rapidly cut from a thick specimen such that 2D images can be obtained throughout the specimen [12–17]. While serial sectioning obviates the need for chemical clearing, it can introduce sectioning artifacts and complicate the reconstruction of 3D volumes. Both non-destructive Path3D and serial-sectioning approaches can enable downstream analyses such as conventional 2D histology and molecular assays, which will be key to demonstrating the clinical value of 3D pathology and ultimately incorporating it into clinical workflows. Serial-sectioning approaches enable direct capture and mounting of sections for conventional analyses when a standard microtome is used, requiring fewer additional steps than re-embedding and sectioning whole-mount Path3D specimens. However, serial-sectioning approaches can make it challenging to archive valuable clinical specimens, as slide-mounting and physically storing every slice from a specimen could be impractical. Path3D does not require physically sectioning the tissue, meaning whole specimens can be archived. Archival needs will depend on the application, and users should consider these trade-offs when selecting a 3D imaging approach. Note that preliminary studies have shown that the H&E-analog and ECi-clearing steps described in this protocol do not adversely affect downstream standard pathology workflows (histology and molecular assays) and we are continuing to perform studies to rigorously

demonstrate the "gentleness" of our methods when used on standard formalin-fixed specimens [9,111,117].

An additional consideration is the maximum specimen size that can be accommodated by each imaging approach. For non-destructive 3D microscopy, imaging depth is a function of both the microscope's working distance (10 mm for the OTLS system used to image many of the specimens shown here [30]) and the degree of optical clearing, which depends on the tissue type. ECi-based clearing reliably achieves imaging depths of at least 500 μm for most tissue types, and much greater imaging depths are possible for some specimens (e.g., whole mouse brains [30]). For much deeper imaging than this, some level of physical sectioning is typically required for either imaging approach (similar to conventional histology). An important caveat is that thick sections (e.g., 1 – 10 mm) can be imaged with cleared-tissue imaging, which may have advantages.

There are several alternatives to the labelling protocols chosen for Path3D. Antibody stains are the primary alternative to small-molecule stains for clinical tissues, where genetically expressed endogenous labels are not possible. While antibodies are the gold-standard in terms of molecular specificity, the diffusion of large (~150 kDa) antibodies into thick tissues can be extremely slow. Staining protocols that rely on passive antibody diffusion can take several weeks for tissues that are only hundreds of micrometers thick and tend to be complex compared to those using small molecule dyes [75,78]. A variety of methods have been developed combining immunolabeling and clearing, including strategies to speed penetration in thick tissues [118–123]. Variations of Path3D using antibodies instead of (or in addition to) small molecule dyes are possible, and while many antibody clones are compatible with ECi- and iDISCO-based clearing methods [https://idisco.info/validated-antibodies], combining immunolabeling and clearing can require specifically tailored protocols [82,124–126].

It is also worth noting that a wide range of clearing protocols have been developed that vary in complexity, protocol duration, fluorophore compatibility, and achievable level of transparency [76,127]. Aqueous clearing methods are the primary alternative to solvent-based clearing approaches. These protocols tend to be gentler on the tissue and compatible with a wider range of fluorescent labels (especially endogenous markers). However, aqueous methods come with some practical challenges especially during extended imaging sessions. These include the tendency to form precipitates, which can be problematic for immersion-based microscopes, and the gradual evaporation of the water in the tissue and/or immersion bath, which can deteriorate tissue clarity and lead to refractive index mismatch issues. We have found that ECi-based clearing (used in our Path3D protocol) is a simple, fast, and reliable method for most tissues for imaging depths of up to a few millimeters. For applications where ECi clearing is inadequate, aqueous protocols like CUBIC [128–130] can work well, as can more-elaborate solvent-based approaches, some of which involve detergents or delipidation steps [126,131]. An important note is that ECi-based clearing results in some degree of tissue shrinkage [80] due to ethanol-based dehydration, which can have both advantages (modest reduction in imaging time) and disadvantages (modest reduction in effective spatial resolution).

Finally, there are several alternatives to light-sheet microscopy for non-destructive imaging of thick tissues [132]. Initial studies used point-scanned techniques such as confocal and multi-photon microscopy [5,19–23]. Commercial point-scanned systems are widely available in core facilities, where dedicated staff and established imaging protocols can be leveraged to quickly establish feasibility in proof-of-concept studies. A major drawback to these laser-scanned systems is relatively slow imaging speed. In addition, some laser-scanned modalities, especially confocal microscopy, are highly light-inefficient, as they only collect a small fraction of the total excited

fluorescence. In the most-basic form of light-sheet microscopy, a 2D plane within the specimen is selectively illuminated and imaged with a high-speed scientific CMOS camera, such that there is very little wasted light and, consequently, reduced photobleaching of the sample. By acquiring datasets plane-by-plane (as opposed to point-by-point or line-by-line), light-sheet systems can also achieve significantly higher imaging rates than laser-scanned microscopy systems and are ideal for high-throughput imaging of large tissue specimens. Depending on the system, light-sheet microscopes can, however, have more complicated sample-mounting workflows than commercial point-scanned systems.

4.1.5 Experimental design

Here, we outline several considerations when designing studies using our Path3D protocol. We specifically focus on large studies in which tens to hundreds of samples must be processed and imaged, and in which large data volumes must be managed.

4.1.5.1 Compatible tissues and selection of sample number and size

We have developed Path3D to work with formalin-fixed (FF) tissues as well as formalin-fixed paraffin-embedded (FFPE) tissues, which are first deparaffinized in the protocol. The procedure has shown success for a variety of clinical tissues including prostate [27–30,73,77,78,111], esophagus [9,10], lung [77], kidney [77], bladder, breast, pancreas, and colon (**Figure 4.2**). We have also had success with preclinical specimens (mouse skin and kidney). For certain tissue types, we have found improved results with alternative staining and/or clearing protocols. As an example, lipid-rich lymph nodes benefit from CUBIC-HV clearing with aggressive delipidation to improve dye penetration (**Figure C.1**a) [8]. Additionally, *in vivo* delivery of antibodies via retro-orbital injection allows for efficient and complete labelling of mouse kidney vasculature and glomeruli

within minutes, even in the deepest layers of the organ (**Figure C.1**c). Nonetheless, Path3D works well for a wide variety of tissues and is the suggested starting point for new tissue types.

It is important to consider sample number and size when designing a study using 3D pathology. Tissue incubation times generally scale with sample size (the smallest dimension) and are typically longer than for 2D specimens to allow for diffusion of reagents into thick tissues. However, by obviating the need for mounting and sectioning by a skilled histotechnologist, the number of hands-on human hours is often less than or comparable to what is required for 2D histopathology. One should consider the trade-off between tissue-preparation times and the amount of contiguous tissue volume that is needed for a selected analysis. For instance, the staining/clearing time for five 100-μm-thick specimens will likely be shorter than for a single 500-μm-thick specimen.

One should also note that imaging times and dataset sizes scale roughly linear with tissue volume and to the third power with resolution. In other words, a 200 μm × 200 μm × 200 μm sample will, in general, take 8× longer to image and produce 8× more data than a 100 μm × 100 μm × 100 μm sample imaged on the same microscope. Likewise, imaging a sample with 1-μm resolution will take 8× longer and produce 8× more data compared to imaging with 2-μm resolution (given Nyquist sampling). Given that datasets can easily reach hundreds of gigabytes (GBs) and imaging sessions can take many hours for large samples, one should carefully consider what resolution and tissue volume are needed for a given study. In some cases, it may be preferable to image a smaller region of interest (ROI) rather than an entire specimen to reduce the total imaging volume. However, it is important to select ROIs with enough coverage to avoid reimaging (for instance if structures of interest are inadvertently truncated or missed) due to both the time required for reimaging and photobleaching concerns addressed above.

4.1.5.2 Computational and data storage requirements

The data processing workflow here was designed to run on a standalone workstation or local server running a standard Windows operating system set up with Python (e.g., Anaconda) but could in principle be adapted for cloud-based storage and processing. Fusing is the most computationally intensive step and benefits from a powerful CPU and large amount of RAM (for reference, we use a local server with 24 CPU cores (48 threads) and 662 GB of RAM). Stitching is much less computationally intensive but for convenience is often done with fusing on the same machine. Our stitching and fusing methods currently do not require a GPU. False coloring is less computationally intensive and can be run on a standard workstation with optional GPU acceleration. Napari performance is generally related to GPU specifications and RAM, though in most cases a standard workstation and GPU are adequate. For large studies, a large-capacity (~100 TB) storage drive is necessary. Finally, compression schemes are worth considering. A variety of compression methods are available, including standard image compression algorithms (e.g., JPEG), popular lossless algorithms (e.g., BLOSC, ZSTD, GZIP), and certain lossy algorithms optimized for scientific applications (e.g., B3D [133], SZ [134]). The ideal compression scheme for each study depends on factors such as the available storage and computational infrastructure, specific processing workflow, and microscopy platform.

Even with a powerful computer, processing times can be significant (often several weeks depending on dataset sizes and numbers). It is important to establish a streamlined workflow that requires minimal human input, such as batching datasets to run overnight. One should likewise consider how data will be transferred both internally (between local machines) and externally (to cloud-based resources, collaborators, etc.). Options include using a high-speed (10 Gbps) internal fiber network connection or loading data onto high-capacity portable drives that can be physically

transferred or shipped. Regardless of strategy, transferring tens to hundreds of TBs of data is always a slow process, and we suggest planning workflows to minimize the number of transfers required.

4.1.5.3 Light-sheet microscopy platform

Factors to consider when selecting a specific light-sheet microscopy platform include volumetric imaging rate, ease of batch imaging (e.g., imaging successive samples without user intervention), maximum sample size, and maximum imaging depth (i.e., working distance). One should also consider the platform's resolution, as this impacts both dataset size and imaging times as discussed previously. To use our stitching and fusing workflow, raw microscope datasets should be in a file format compatible with BigStitcher (e.g., HDF5). Alternatively, datasets can be stitched and fused using other methods (such as with native microscope pipelines) and converted to a standard format (e.g., HDF5, TIFF stack) for false coloring and/or visualization.

4.1.5.4 Visualization software

The most straightforward approach for image visualization by downstream users (e.g., pathologists), as described in this protocol, is to install display software (e.g., Napari, QuPath) and to load datasets onto a computer that can be accessed by users physically or via remote login. An alternative approach is to use a web-based viewer. While convenient, there are not yet open-source options for web-based viewing and this option is not discussed here. We do not recommend loading data and software directly onto every user's computer given differences in hardware, installation requirements, etc.

4.1.6 Required expertise

This protocol is intended for microscope end-users, including bioengineers, clinical researchers, and life scientists ranging from undergraduates to postdocs and staff scientists. As this is a multidisciplinary end-to-end workflow, no reader is expected to be an expert in all aspects of the process. For tissue preparation (steps 1 – 2), some experience with tissue staining and clearing is helpful but not required. For additional background, readers may consult previous work on clearing and staining, particularly ECi/iDISCO methods [76,80–82,135]. For sample imaging (steps 3 – 8), researchers should be competent using their chosen microscope platform (e.g., sample mounting, previewing samples, adjusting imaging parameters). For image processing (steps 9 – 20), users should have basic familiarity with Python (including package installation, development environments, Anaconda, etc.). Experience with using BigStitcher is also helpful; we recommend new users consult online tutorials [https://imagej.net/plugins/bigstitcher].

4.1.7 Regulatory approvals

Experiments using human or animal tissues must follow appropriate regulations with respect to informed consent/care of animals, which may include regulatory approval. This section is based on our experience with regulations in the United States (where our research is conducted).

The cost of Institutional Review Board (IRB) review for human-subjects research will vary by institution and IRB selection, ranging from no cost (such as for some internal or federally operated IRBs) to several thousand dollars or more (for some external IRBs). IRB review speed is likewise variable and can take several months, so researchers should plan ahead. Approval for initial 3D pathology studies that do not affect the standard of care (e.g., saving resected surgical specimens that would otherwise be discarded) is generally more straightforward than for interventional studies. Studies conducted using only de-identified human tissues (e.g., from an

institutional tissue bank) may not require separate IRB approval, which can greatly simplify regulatory considerations.

Institutional Animal Care and Use Committee (IACUC) review for animal research similarly ranges from no cost to several thousand dollars and can take several months. Using tissue from already-euthanized animals (e.g., from carcass donation programs after animal trainings) can be appropriate for some studies. This approach may not require separate IACUC approval.

The human specimens shown in **Figure C.1**b were obtained with approval from the University of Washington IRB and with informed consent from patients. All other human tissues shown in this manuscript were de-identified specimens provided by an institutional tissue bank and were not subject to IRB approval at the University of Washington. The animal tissues shown in **Figure C.1**c were collected with approval by the Animal Care and Use Committee at the Indiana University School of Medicine and in accordance with National Institutes of Health Guidelines for the Care and Use of Laboratory Animals. The animal tissues shown in **Figure C.8**b were collected from already-euthanized animals donated by an institutional animal facility at the University of Washington and not subject to IACUC approval.

4.2 Materials

4.2.1 Biological materials

- Formalin-fixed (FF) or formalin-fixed paraffin-embedded (FFPE) tissue specimens

  ! CAUTION Experiments using human or animal tissues must follow appropriate institutional and governmental regulations with respect to informed consent/care of animals.

4.2.2 Reagents

- Ethanol (Decon Laboratories, cat. no. 2701)

  ! CAUTION Ethanol is flammable and volatile, work with small amounts and store large quantities in a flammables cabinet. Ethanol is also an eye hazard. Wear appropriate personal protective equipment (PPE).

- Deionized (DI) water
- Sodium chloride (NaCl) (Spectrum Chemical, cat. no. SO160)
- 0.1N Hydrochloric acid (HCl) (Fisher Scientific, cat. no. SA54-1)

  ! CAUTION Hydrochloric acid is a skin and eye hazard. Wear appropriate PPE.

- Xylene (Fisher Scientific, cat. no. X3P-1GAL)

  ! CAUTION Xylene is flammable and volatile, work with small amounts and store large quantities in a flammables cabinet. Xylene is also a significant skin, eye, and respiratory hazard. Wear appropriate PPE and do not handle outside of a fume hood.

- TO-PRO-3 iodide, 1mM solution in dimethyl sulfoxide (DMSO) (Thermo Fisher Scientific, cat. no. T3605)

  CRITICAL STEP TO-PRO-3 should be protected from ambient light during storage to avoid photobleaching.

- Alcoholic eosin Y 515 (Leica Biosystems, cat. no. 3801615)

  ! CAUTION Alcoholic eosin is flammable and volatile, work with small amounts. Alcoholic eosin is also an eye hazard. Wear appropriate PPE.

  CRITICAL STEP Alcoholic eosin should be protected from ambient light during storage to avoid photobleaching.

- Ethyl cinnamate (ECi) (Thermo Fisher Scientific, cat. no. A12906.36)

! CAUTION Ethyl cinnamate degrades polystyrene and other plastics. Use glass or polypropylene (PP) containers. Using incompatible plastic containers can cause the container to rupture or contaminate the contents.

- Agarose powder (Benchmark Scientific, cat. no. A1700)
- 150-nm diameter gold nanoparticles, stabilized suspension in citrate buffer (Sigma-Aldrich, cat. no. 742058)

4.2.3 Reagent setup

Path3D staining buffer

The Path3D staining buffer is a mixture of 70% v/v ethanol in deionized (DI) water with 10 mM NaCl at pH 4. Saline conditions improve TO-PRO-3 penetration in thick tissues [123], and acidic conditions improve eosin binding. To prepare 100 mL of staining buffer solution, add 70 mL ethanol and 58.44 mg NaCl to 10 mL DI water in a 250 mL beaker. Mix the staining buffer on the orbital shaker until the NaCl is fully dissolved. Add 0.1N HCl to the solution using a transfer pipette until the solution reaches pH 4 (typically 6 – 7 drops), measured using the pH meter. Finally, add DI water until the total volume of the solution is 100 mL. The buffer solution may be stored for one month at 4 °C but should be brought to room temperature (RT, ~21 °C) before use.

! CAUTION Ethanol is flammable and volatile, work with small amounts and store large quantities in a flammables cabinet. Ethanol is also an eye hazard. Wear appropriate PPE.

! CAUTION Hydrochloric acid is a skin and eye hazard. Wear appropriate PPE.

4.2.4 Equipment

- 250 mL beaker (Kimble Kimax, cat. no. 14000-250)
- Scale (VWR, cat. no. VWR-164AC)

- Orbital shaker (Labnique, cat. no. MT-201-BD)
- Transfer pipets (Fisher Scientific, cat. no. 13-711-9AM)
- pH meter (Thermo Fisher Scientific, cat. no. 13-645-611)
- Magnetic hotplate stirrer (VWR, cat. no. 97042-606)
- 1” magnetic stir bar (VWR, cat. no. 58948-138)
- Immersion thermometer (VWR, cat. No. 89095-628)
- Razor blades (VWR, cat. No. 55411-055)
- 6-well biopsy cassettes (Simport Scientific, cat. no. M503-10)
- Standard pencil (Ticonderoga, #2/HB)
- Tweezers (POLYPLAS Hameln GmbH, cat. no. 1404B-SA)
- Standard aluminum foil (Miktomeh, 1000 SQ FT)
- Standard micropipettes (Rainin, cat. no. HU Start Kit PL-LTS 20,200,1000u)
- 2.0 mL Eppendorf safe-lock tubes (Eppendorf, cat. no. 022363352)
- Roto-Therm rotator (Southern Labware, cat. no. H2024)
- 15 mL polypropylene conical tubes (Cellstar, cat. no. 188271)
- 50 mL beaker (Kimble Kimax, cat. no. 14000-50)
- 50 mL polypropylene conical tubes (Cellstar, cat. no. 227270)
- Light-sheet microscopy platform (see Experimental design section for details)
- Computing and data storage setup (see Experimental design section for details)

4.3 Procedure

4.3.1 Tissue preparation

The following procedure is optimized for 1- to 3-mm diameter punch-biopsy or needle-biopsy specimens (~5 – 50 mm^3 biopsy volume after trimming excess wax). Incubation times and reagent volumes may need to be adjusted based on sample size.

! CAUTION Experiments using human or animal tissues must follow appropriate institutional and governmental regulations with respect to informed consent/care of animals.

1 OPTIONAL Deparaffinization of FFPE specimens *(51 hrs)*

(A) Specimen trimming and loading

(i) Trim any large pieces of excess wax (**Figure 4.3**a) from FFPE specimens using a razor blade.

CRITICAL STEP Use caution if trimming small or thin specimens as they are prone to cracking. Aggressive trimming is not necessary, and excess wax that is challenging to trim can be removed through longer xylene incubation in the following steps.

(ii) Load FFPE specimens into 6-well histology cassettes (1 specimen per well, i.e., up to 6 specimens per cassette). Label cassettes with pencil or a xylene-resistant ink (**Figure 4.3**b).

CRITICAL STEP We do not recommend using cassettes other than standard histology cassettes (a durable polymer), as many plastics (such as polystyrene) are not chemically resistant to xylene and may dissolve.

(B) Xylene incubation

(i) In a fume hood, fill a 250 mL beaker with 100 mL xylene and heat to 60 °C (measured using an immersion thermometer) on a hot plate. 100 mL of xylene is adequate to process 1 or 2 cassettes. For more than 2 cassettes, larger volumes and/or multiple beakers may be needed to ensure adequate circulation of xylene.

(ii) Add cassettes to the beaker of preheated xylene, ensuring they are fully immersed. Add a magnetic stir bar (**Figure 4.3**c).

(iii) Adjust hotplate to maintain a constant xylene temperature of 60 °C (measured using the immersion thermometer) and incubate with stirring (~200 rpm) for 48 hours.

CRITICAL STEP Cover beaker with aluminum foil to prevent evaporation.

(iv) OPTIONAL Exchange xylene with fresh xylene after 24 hours for tissues with excessive amounts of wax.

! CAUTION Xylene is flammable and volatile, work with small amounts and store large quantities in a flammables cabinet. Xylene is also a significant skin, eye, and respiratory hazard. Wear appropriate PPE and do not handle outside of a fume hood.

(C) Ethanol wash

(i) Turn off heat and let xylene cool for 15 – 20 minutes. Once xylene and cassettes have cooled to RT, remove xylene and add enough 100% ethanol to submerge cassettes (~50 – 100 mL). Incubate with stirring (~ 200 rpm) at RT for 1 hour.

(ii) Exchange the ethanol with fresh ethanol and incubate for 1 more hour.

PAUSE POINT For temporary storage (a few days), samples may be left in 100% ethanol in a sealed container to prevent evaporation.

2 Staining with a fluorescent analogue of hematoxylin & eosin (H&E) and optical clearing

(A) Tissue rehydration *(3 hrs)*

(i) In the 250 mL beaker, place cassettes in enough 70% ethanol (v/v solution in DI water) to submerge (~50 – 100 mL) and incubate for a minimum of 3 hours on the orbital shaker with gentle agitation (~60 – 80 rpm) at RT.

PAUSE POINT For temporary storage (a few days), samples may be left in 70% ethanol in a sealed container. For longer storage, samples should be rehydrated in graded-ethanol steps and stored in phosphate-buffered saline (PBS) with 0.1% sodium azide at 4 °C to prevent protein extraction. Note that sodium azide is highly toxic and appropriate usage and handling are not discussed here. Users should consult other protocols for additional guidance on storing tissues in PBS/sodium azide.

For possible problems and solutions encountered in this protocol at steps indicated with the **TROUBLESHOOTING** label, see the troubleshooting section (Table 4.1).

(B) Tissue staining *(2 days)*

(i) Prepare staining solution of 1:500 v/v TO-PRO-3 and 1:100 v/v eosin (together) in Path3D staining buffer (see Reagent Setup).

(ii) Transfer each specimen to a separate 2 mL Eppendorf tube and add 1.5 mL prepared staining solution to each tube. Incubate specimens for 48 hours in the Roto-Therm rotator with mixing mode at 20 rpm at RT (**Figure 4.3**d).

! CAUTION Alcoholic eosin is flammable and volatile, work with small amounts. Alcoholic eosin is also an eye hazard. Wear appropriate PPE.

CRITICAL STEP Ensure that specimens are completely submerged in staining buffer during incubation. For this and all subsequent steps, fluorescently labelled specimens should be protected from ambient light (e.g., by covering tubes in aluminum foil) to prevent photobleaching.

TROUBLESHOOTING

(C) Tissue dehydration *(2 hours)*

(i) Transfer each specimen to a separate 15 mL polypropylene tube and add ~10 mL 100% ethanol to each tube. Incubate specimens for 1 hour on the orbital shaker with gentle agitation (~60 – 80 rpm) at RT.

(ii) Exchange ethanol with fresh ethanol and incubate for at least 1 more hour.

(iii) OPTIONAL Incubate large samples in 100% ethanol overnight to ensure complete dehydration.

CRITICAL STEP It is important to remove all water in the specimen during this step as any residual water will impede clearing. Ensure that all sample holders and storage tubes are free from condensation and are completely dry, especially in humid environments.

CRITICAL STEP Dehydrated specimens can be brittle. Be gentle if using tweezers to transfer specimens.

TROUBLESHOOTING

(D) Tissue clearing *(4 hours)*

(i) Transfer each specimen to a new 15 mL polypropylene tube and add 10 mL ECi. Incubate specimens for 2 hours on the orbital shaker with gentle agitation (~60 – 80 rpm) at RT (**Figure 4.3**e).

(ii) Exchange ECi with fresh ECi and incubate for 2 more hours.

! CAUTION Ethyl cinnamate degrades polystyrene and other plastics. Use glass or polypropylene (PP) containers. Using incompatible plastic containers can cause the container to rupture or contaminate the contents.

PAUSE POINT Cleared specimens may be stored in 100% ECi at RT for several weeks to months before imaging. Ensure that specimens are protected from light. We do not recommend storing cleared specimens in the refrigerator. For extended archival storage (e.g., after imaging), specimens may be re-embedded in paraffin.

TROUBLESHOOTING

4.3.2 3D microscopy

4.3.2.1 Characterize systems with optically cleared agarose bead phantoms

3 Make agarose nanoparticle phantoms *(1 hour)*

(A) Fill the 50 mL beaker with 19 mL DI water. Add a magnetic stir bar and heat the liquid to ~85 °C (measured using an immersion thermometer) on a hot plate.

(B) Set stirring to a high speed (~400 rpm) and add ~1% wt/vol agarose powder (~0.2 g for a 20 mL final volume).

CRITICAL STEP Add the agarose powder slowly to prevent clumping.

(C) Cover the beaker with foil and incubate with continued stirring until agarose powder is completely dissolved (~10 – 15 min), adjusting the hotplate setting as needed to maintain a liquid temperature of ~85 – 90 °C.

CRITICAL STEP Keep the beaker covered with foil throughout agarose preparation and avoid overheating the mixture to prevent excessive evaporation. If too much water evaporates (more than ~20%), the final agarose concentration will change and may make it hard to form or use phantoms. We do not advise preparing less than 20 mL of agarose at a time, as excessive evaporation may occur.

(D) After dissolution, add ~5% v/v 150-nm diameter gold nanoparticle suspension to the solution (~1 mL nanoparticle suspension for a 20 mL final volume, yielding a target concentration of ~2×10^5 nanoparticles/mL).

CRITICAL STEP Nanoparticles may settle to the bottom of the citrate buffer. Shake or vortex the container thoroughly before removing nanoparticles.

(E) Turn off the heat and cool the mixture to 70 °C with continued stirring (10 – 15 min).

(F) Pipette mixture into 2 mL microcentrifuge tubes (~0.5 mL per tube). Close tubes and place lid-side down on a flat surface until cooled to RT (~30 min). Remove each phantom and proceed with dehydration or transfer the phantoms to DI water for storage. Microcentrifuge tubes create ~1 cm diameter cylindrical phantoms with flat bottoms, which are convenient for inverted or open-top microscopes with a planar sample holder (**Figure C.2**). However other mold shapes can be used to accommodate other sample mounting requirements.

CRITICAL STEP Work quickly as the mixture will cool and solidify rapidly once it is in a small volume in the pipette or tubes. Close and invert each tube as it is filled to prevent the mixture from solidifying in the bottom of the tube.

PAUSE POINT Uncleared phantoms may be stored indefinitely (several months or more) in DI water at RT. Many phantoms can be stored in the same container as long as they remain submerged. As nanoparticles are reflective as opposed to fluorescent, it is not necessary to protect phantoms from ambient light.

4 Dehydrate and clear agarose nanoparticle phantoms *(8 hours)*

Use a minimum of ~10 mL of liquid per phantom in each step (e.g., use 40 mL of liquid for 4 phantoms in a 50 mL conical tube), and ensure phantoms are fully submerged. The listed incubation times are minimums and longer incubations times will not adversely affect the phantom. Phantoms can be treated much like a fixed tissue and dehydrated/cleared in other media as needed.

(A) Incubate phantoms in 100% ethanol for 2 hours at RT.

(B) Exchange the ethanol with fresh ethanol and incubate for 2 more hours.

(C) Incubate phantoms in 100% ECi for 2 hours on the orbital shaker with gentle agitation (~60 – 80 rpm) at RT.

(D) Exchange the ECi with fresh ECi and incubate for 2 more hours.

CRITICAL STEP Multiple phantoms may be processed together.

PAUSE POINT Cleared phantoms may be stored indefinitely (several months or more) in ECi at RT. Many phantoms can be stored in the same container as long as they remain submerged.

5 Image the agarose nanoparticle phantoms

Image phantoms in reflectance mode (i.e., no emission filter) with red light (e.g., 638 nm) illumination. The scattering signals from gold nanoparticles tend to be significantly brighter than fluorescent dyes, so it may be necessary to use a low laser power or place a neutral density filter in the illumination or collection light path to avoid saturating the detector.

(A) Preview the bead phantom and qualitatively assess the bead size and shape (**Figure 4.4**a-d). Adjust the imaging parameters until the microscope is well aligned and beads are optimally resolved based on the following conditions:

(i) Beads should have a signal to background ratio (SBR) of at least ~20 (see Box 1). Peak signal counts should be well above the background level (i.e., signal counts in regions of agarose with no beads) and well below the detector's saturation point. For a 16-bit detector with a background level of 100 – 300 detector counts, we aim for peak signal levels of at least 5,000 detector counts.

(ii) For most systems, optimally resolved beads should form a symmetric (approximately Gaussian) point spread function (PSF) in all three dimensions. When previewing the phantom, view the beads in successive image planes (i.e., scrolling through a small volume) to qualitatively check the PSF shape and size in all three dimensions.

(iii) For Nyquist-sampled imaging, the full width at half maximum (FWHM) of each bead should be ~ 2 – 3 pixels in width. For some system geometries, the imaging plane seen while previewing may not be the highest resolution plane. Likewise in systems with anisotropic resolution, Nyquist sampling may not be expected in every spatial dimension.

(iv) Bead size and shape should be consistent across the field of view in terms of region-to-region trends. Outliers and some variation between individual beads are expected (**Figure C.3**).

CRITICAL STEP To accurately quantify resolution, beads should be diffraction-limited (i.e., 5× – 10× smaller than the microscope's resolution). Smaller beads may be necessary for some imaging systems. However, if the goal is to ensure uniformity and not to accurately quantify the PSF, slightly larger beads are acceptable.

(B) Once the beads are well-focused, collect a 3D volume (~ 1 × 1 × 1 mm^3). Select a volume that does not include the edges of the phantom or defects (cracks, air bubbles, etc.), as these can interfere with PSF quantification.

6 Quantify PSF dimensions across a 3D volume *(Computational time on the order of several hours)*

(A) Compute PSF dimensions using the Bead_PSF_computation Python package (see Appendix C.11 for additional details). The provided package requires an input bead phantom dataset as a TIFF stack. In the computed results, the X and Y dimensions are in the TIFF image plane, while the Z dimension is orthogonal to the image plane.

(i) Install the Bead_PSF_computation package by running the following command from a git command line:

```
git clone
https://github.com/kevinwbishop/Bead_PSF_computation
```

(ii) Fuse the HDF5 dataset to a TIFF stack in BigStitcher, reorienting as needed (stitching is not necessary to quantify PSFs). See steps 9 – 12 for details.

(iii) Open `PSF_notebook.ipynb` in Jupyter and run on the fused TIFF stack. Step-by-step instructions are provided in the notebook file.

PAUSE POINT Initially computing the PSFs is computationally intensive and can take several hours on a standard workstation. Once initial results are computed, the data can be saved by the notebook as a CSV file and loaded again later to quickly produce additional visualizations.

(iv) As a starting point, refer to the histograms (**Figure 4.4**e) showing the X, Y, and Z dimensions (FWHM) of each bead's PSF. For a well-aligned microscope, the median FWHM should roughly match the system's resolution (within ~25%), and the histogram should show an approximately normal distribution with minimal variance (< 25% standard deviation) in bead dimensions. The scatter plots (**Figure C.3**) and heat maps (**Figure 4.4**f, **Figure C.4**) produced by the Jupyter notebook can subsequently be used to understand how the system's resolution varies across the field of view in one or two dimensions. A well-aligned system should have global variations in FWHM of < 25% across the field of view (though bead-to-bead variance may be higher and local outliers will exist, **Figure C.3**).

TROUBLESHOOTING

(B) Agarose phantom results provide a benchmark of the resolution achievable with the imaging system's current alignment and are valuable for downstream troubleshooting. If the resolution measured with agarose phantoms is not within ~25% of the microscope's specifications, there is likely an alignment issue that needs to be addressed before proceeding.

4.3.2.2 Imaging of tissue

Due to variations in sample preparation, tissue structure, etc., some tuning of initial imaging parameters is typically required for each sample type to optimize image quality.

7 Mount the stained and cleared tissue on the microscope and preview the cytoplasm (eosin: 525 nm excitation peak, 545 nm emission peak) and nuclear (TO-PRO-3: 640 nm excitation peak, 655 nm emission peak) channels.

8 Adjust the microscope's exposure time and laser power until signal levels are adequate, then image the tissue. Use the following steps to assess signal levels while previewing the specimen:

(A) Estimate the peak signal level and signal to background ratio (SBR) of each channel (see Box 1).

(B) For optimal false-coloring results, the SBR should be ~10 or more. The peak signal level should be well above the image background level but below the detector's saturation point in order to maximize dynamic range. For a 16-bit detector with background detector counts of 100 – 300, we ideally aim for peak signal levels of at least 2000 detector counts (SBR ~10). Note that the required peak signal level and SBR will depend on the application.

CRITICAL STEP Specimens are particularly prone to photobleaching while previewing the sample, where one may be continuously viewing the same plane in a specimen. We suggest starting with minimal laser power to initially identify a region of interest.

Box 1 | Signal, background, and noise

Here, we define peak signal level as the average component of detector counts in brightly stained regions of the sample and background level as the average component of detector counts in unstained regions of the sample. The background level is a combination of detector background (e.g., dark counts), sample autofluorescence, and other sources of stray or ambient light. Background regions are typically straightforward to identify in the nuclear channel (any regions without nuclei). For the cytoplasm channel, identifying background regions can be challenging as eosin will stain most tissue components to some degree. For certain tissues, the gland or vessel lumens can be used to quantify the eosin background level. We define the noise level as the random variation (standard deviation) in the background of an image (Figure C.5).

We confirm adequate signal levels by checking the peak signal level and the signal to background ratio (SBR), or "contrast" (which can be readily estimated by comparing the peak signal level to the background level), for each specimen. The random noise level tends to be dominated by detector noise in the context of Path3D (sCMOS-based light-sheet imaging) and is typically well below the target signal levels. Therefore, adequate peak signal level and SBR usually also implies adequate signal to noise ratio (SNR), or "brightness".

4.3.3 Data processing

In this section, we describe our overall data-processing workflow and offer practical guidance relevant to Path3D datasets. The exact programmatic steps will vary with each experimental and data-management setup. For detailed usage instructions and examples, users should consult the online documentation for each software package:

BigStitcher: https://imagej.net/plugins/bigstitcher

FalseColor-Python: https://github.com/serrob23/falsecolor

Napari: https://napari.org/stable

4.3.3.1 Image tile stitching and fusing using BigStitcher *(Computational time on the order of several hours)*

9 Install FIJI [99] and the BigStitcher plugin [98].

10 Load the raw dataset and inspect the image data under different views, regions, and magnification scales. Ensure that the image tiles are roughly aligned to one another and that image quality is relatively consistent across the dataset. Note that BigStitcher supports a variety of import file formats. Multiresolution pyramidal formats such as HDF5 [94] offer efficient navigation of large datasets, which is convenient for interactive previewing.

11 Run stitching (via the Stitching Wizard) to align the tiles based on image features, which can compensate for minor misalignments between raw image tiles.

TROUBLESHOOTING

12 Run fusion to blend individual tiles into a continuous and seamless 3D volume.

CRITICAL STEP The image fusion process can be very slow (several hours for 100-GB-scale datasets on a workstation with ~512 GB of RAM). We recommend fusing the dataset on a workstation with a large amount of RAM (> 256 GB) for faster processing. Processing time and fused dataset size can be reduced by cropping the dataset to a subregion using the “Bounding Box” feature or reducing the resolution via downsampling.

(A) OPTIONAL When fusing to a TIFF stack file format, the slicing plane must be specified. Before fusing, use the “Interactively Reorient Sample” option to orient the sample view to lie in the desired slicing plane.

4.3.3.2 OPTIONAL Generating virtual H&E images using FalseColor-Python *(Computational time minimal)*

13 Install the Cuda Toolkit followed by FalseColor-Python. We recommend installing FalseColor-Python in its own virtual environment. Note that many methods within FalseColor-Python (e.g., `fc.rapidFalseColor`) require a Cuda-enabled GPU. For use without a GPU, equivalent CPU-based methods (e.g., `fc.falseColor`) are provided.

14 All false coloring and image processing methods are contained in the coloring module of FalseColor-Python. Import this module using:

```
import falsecolor.coloring as fc
```

Generating a virtual H&E image using FalseColor-Python requires two grayscale images: a nuclear channel (TO-PRO-3) and a cytoplasm channel (eosin), which will be referred to as "nuclei" and "cyto" below.

15 Read nuclei and cyto into memory using any standard image processing library such as Scikit-Image [136], OpenCV [https://opencv.org], Tifffile [137], or H5py [https://www.h5py.org]. Both the nuclei and cyto images should be NumPy arrays [138] of the same lateral dimensions.

16 To improve the appearance of smaller structures within the final virtual H&E image, FalseColor-Python has an image-sharpening method, `fc.sharpenImage`. This method returns an image that has been convolved with a horizontal and vertical edge-sharpening kernel. For example:

```
sharp_nuclei = fc.sharpenImage(nuclei)
sharp_cyto = fc.sharpenImage(cyto)
```

17 Load nuclei and cyto color settings for the virtual H&E image using `fc.getColorSettings`:

```
color_settings = fc.getColorSettings() #dict with
    'nuc' and 'cyto' as keys
nuclear_settings = color_settings['nuc'] # list of
    floats containing weights for nuclear RGB levels
cyto_settings = color_settings['cyto'] # list of
    floats containing weights for cyto RGB levels
```

The color settings represent the weights that each channel (nuclei and cyto) contributes to the final RGB (red green blue) levels of the virtual H&E image. Default settings were empirically derived to match the hue and saturation levels seen in standard histology [77]. However, color preferences in histology are subjective and these weights can be adjusted to tune the coloration as desired. Each individual color level affects the relative color balance in the final H&E image. For example, nuclei with a bluer hue in the final virtual H&E image can be achieved by increasing the first constant in the `nuclear_settings` list. Further discussion of color settings and their effect on the final appearance of the virtual H&E image is available in the `Adjusting Color Settings.ipynb notebook`.

18 Generate a virtual H&E image from nuclei and cyto using `fc.rapidFalseColor`:

```
virtual_HE = fc.rapidFalseColor(nuclei, cyto,
nuclear_settings, cyto_settings)
```

CRITICAL STEP `rapidFalseColor` has four additional input parameters: background levels for each channel (`nuc_bg_threshold` and

`cyto_bg_threshold`) and normalization factors (`nuc_normfactor` and `cyto_normfactor`). These parameters are designated as integer values, which have been optimized for datasets in our lab but will likely change depending on the microscope and individual dataset. Each of these parameters affects the saturation levels of the final virtual H&E image in a slightly different way (**Figure C.6**).

The background threshold for each channel is the pixel value (assumed 16 bit) below which all pixels will be set to zero (and thus appear white in the final virtual H&E image). This can help reduce nonspecific background in empty regions of the image. Note that this level is subtracted from *all* pixels, and thus higher values for each channel will result in a lighter appearance in the virtual H&E image.

The normalization factor for each channel is the constant that all pixels are divided by before the final coloration. This helps to reduce overly bright regions in the grayscale image such that they do not appear unrealistically saturated (or dark) in the final virtual H&E image. Further discussion of normalization settings and their effect on the final appearance of the virtual H&E image is available in the `Adjusting Color Settings.ipynb` notebook.

4.3.3.3 Visualizing fused and (optionally) false-colored datasets using Napari

CRITICAL STEP While Napari can be used out of the box on a standard workstation to view small datasets (i.e., smaller than the available RAM), viewing larger datasets can be inefficient or impossible. To view large datasets, users should use dynamic loading and/or compressed datasets to reduce computational requirements (Appendix C.12).

19 Install Napari [107] using Pip (we suggest the “batteries included” installation) in a new virtual environment.

20 Launch Napari and load the data Z-stack (raw fluorescence data or false-colored data). The Napari viewer allows users to pan, zoom in and out, and scroll in the Z-dimension through the dataset. Annotations can be added interactively using the “Layers” feature.

CRITICAL STEP For visualization in Napari, false-colored datasets must be saved as an RGB TIFF stack.

CRITICAL STEP Save annotations using “Save All Layers”. For 3-dimensional datasets, layers cannot be saved as a “napari SVG (*.svg)” file. Instead use “napari Save to Folder (*.*)”. The folder will include the original dataset and the coordinates of the shapes, points, and labels from each layer stored in a CSV file. Load saved annotations by dragging and dropping the CSV file into Napari.

TROUBLESHOOTING

4.3.4 Quality control

CRITICAL Ongoing quality control is essential to generating consistent data. The following steps should be used to iteratively establish the staining and imaging conditions at the start of a study, as well as to evaluate each collected dataset during a study. Quality control should be performed throughout an imaging study so that any problems can be caught and addressed promptly.

4.3.4.1 Quantitatively assess signal counts for each specimen

21 Fuse the raw HDF5 dataset as a TIFF stack sliced parallel to the tissue surface (HDF5 files must be viewed in BigStitcher, which does not allow for easy quantification of signal counts). See steps 9 – 12 for details. For large datasets, it is more efficient to fuse

a few discrete Z levels of interest rather than the entire specimen. Accurate stitching is not necessary for initially assessing signal counts.

22 Plot line profiles across the specimen at multiple Z levels (e.g., near the tissue surface, 250 μm deep, 500 μm deep) (**Figure 4.5**). Based on qualitative assessment of images, select line profiles that adequately capture variations in signal counts (e.g., through a dimmer core, across intensity gradients from one side of the tissue to the other). When comparing across multiple specimens, select line profiles with similar positions and orientations as signal counts may be impacted by scan direction, light-sheet illumination direction, etc. Line profiles can be plotted in FIJI [99] using the "Plot Profile" tool.

23 Confirm that the peak signal level and SBR are high enough without saturating the detector. See step 8 for additional details on assessing signal levels.

CRITICAL STEP Datasets with inadequate signal levels can often be made to *appear* bright and well contrasted by tuning display settings in BigStitcher/FIJI. However, such datasets may not yield reliable false-colored results and may not be ideal for computational analysis. It is therefore essential to quantitatively assess signal levels using line profiles.

TROUBLESHOOTING

24 Confirm that signals within each specimen are consistent both laterally and with depth. Ideally, peak signal counts for similar structures should vary by < 25% across a specimen (**Figure 4.5**).

TROUBLESHOOTING

4.3.4.2 Qualitatively assess image sharpness for each specimen

25 Assess image sharpness as a function of depth by qualitatively inspecting small features in the tissue architecture (such as isolated nuclei/subnuclear features in the nuclear channel or collagen fibers in the cytoplasmic channel). The degree of degradation with depth is driven primarily by the quality of optical clearing, and some degradation in sharpness is expected even for well-cleared tissues. For most tissue types, images should remain reasonably sharp at imaging depths of at least 500 μm.

TROUBLESHOOTING

4.4 Troubleshooting

4.4.1 General approaches to troubleshooting image quality

Loss of signal and loss of sharpness often occur together as they are related effects caused by refractive-index heterogeneities within the sample (leading to scattering and aberrations). However, in general, problems with staining or laser power/exposure time have a greater impact on signal counts, while problems with alignment and clearing have a greater impact on sharpness.

For elusive image quality issues, we suggest sketching out the light paths of both the illumination beam and excited fluorescence for different regions of tissue. These details will vary based on the geometry of the specific imaging system, and understanding how light is traveling through the tissue to and from the imaging plane can provide insights into the source of a particular problem. For instance, low signal near a tissue edge where the illumination path length in tissue is significantly longer than the collection path length could be indicative of illumination attenuation rather than collection attenuation (**Figure C.7**).

4.4.2 Specific problems and possible solutions

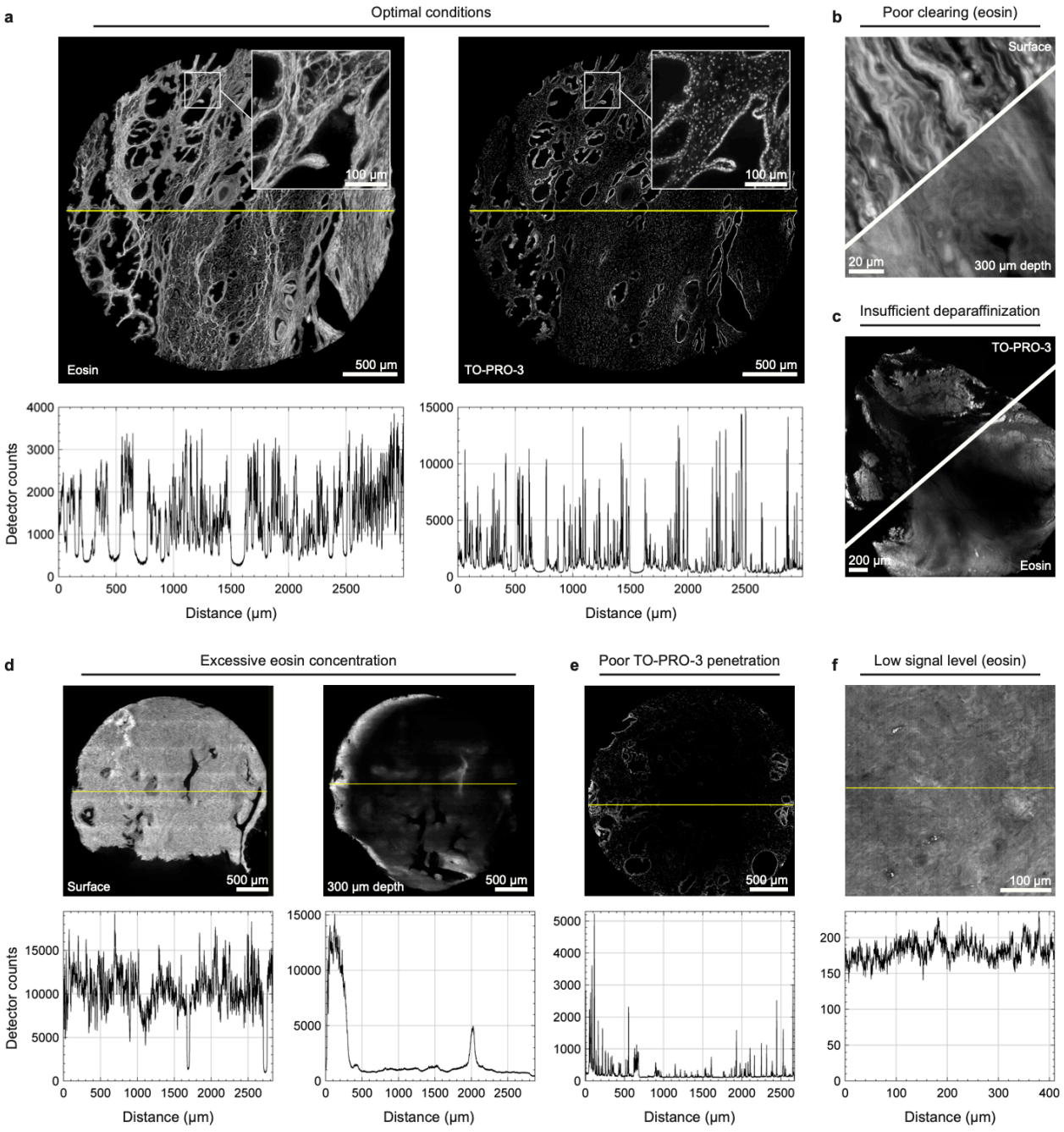


Figure 4.5 Images and line profiles (the yellow line in each image) are from human prostate tissue imaged with OTLS microscopy and show various staining, clearing and imaging conditions. **(a)** Optimal staining and imaging conditions showing high SBR (>10) and peak signal levels (>2,000 detector counts) in both channels with uniform signal levels across the tissue. Insets show well-resolved collagen fibers

(eosin channel) and nuclei (TO-PRO-3 channel). **(b)** Poor clearing results in scattering of illumination and/or collection beams, degrading image sharpness with depth. **(c)** Insufficient deparaffinization results in poor staining (especially at the core of the sample) in both channels. **(d)** Excessive eosin concentration causes the illumination light to be absorbed before reaching the interior of the tissue, resulting in bright edges and a dark core. Note the laterally asymmetric brightness when imaging at depth because of the illumination light entering from one side of the tissue in this particular imaging geometry (OTLS microscopy) (**Figure C.7**). **(e)** Uneven staining because of poor TO-PRO-3 penetration in tissue resulting in bright edges and a dark core. **(f)** Low eosin signal level (resulting in poor SNR) because of inadequate dye concentration, laser power or exposure time. Note the presence of noise artifacts (vertical stripes) in the image because of insufficient SNR.

Table 4.1. Troubleshooting of Path3D

Step	Problem	Possible reason	Solution
Step 2	Samples shows signs of distortion after dehydration or rehydration.	Direct transitions between 100% ethanol and 70% ethanol cause distortion.	Use graded steps of ethanol when dehydrating and rehydrating specimens.
Step 2	Staining, particularly the blue TO-PRO-3 stain, is visibly uneven across tissue upon gross inspection after staining (Figure C.8a).	TO-PRO-3 is typically stained in saline buffer conditions and may not penetrate into tissue if salt concentration is too low.	Verify NaCl concentration and increase concentration if needed, and ensure the tissue is sufficiently agitated while staining.
Step 2	Sample is visibly not transparent upon gross inspection after clearing (Figure C.8b).	Sample was not fully cleared in ECi.	Increase the clearing time in 100% ECi, and/or use multiple rounds of ECi.
Step 6	Python script fails to identify sufficient beads.	Bead concentration is too high or too low. Beads must be well separated in order to be properly quantified, so too high of a concentration will result in few well-separated beads. Likewise, too low of a concentration will result in few beads overall.	Visually inspect the bead dataset and compare to Figure 4.4a to assess concentration. Increase or decrease bead concentration as needed.

Table 4.1. Troubleshooting of Path3D

Step	Problem	Possible reason	Solution
Steps 9 – 11	Obvious misalignment of structures between tiles.	Overlapping areas are too small, causing the stitching algorithm to fail.	Increase overlapping regions between adjacent tiles.
Steps 19 – 20	Only one 2D image from a 3D dataset is viewable in Napari.	The dataset is saved as a multi-channel composite image stack instead of an RGB image stack.	Open the dataset in FIJI and convert to an RGB stack using "Image > Color > Stack to RGB". Save the converted dataset and reopen in Napari.
Steps 21 – 24	Uneven TO-PRO-3 signal: signal counts are high at the tissue surface on all sides, but low in the tissue core (Figure 4.5e).	Insufficient salt concentration in the staining buffer causes TO-PRO-3 to bind rapidly to the tissue surface before diffusing into the tissue core.	Increase salt concentration to slow TO-PRO-3 binding and allow time for dye to diffuse into the tissue core.
Steps 21 – 24	Signal counts are too low across tissue (for either channel) (Figure 4.5f)	Insufficient dye concentration, laser power, or exposure time.	Increased dye concentrations, higher laser powers, and longer exposure times will all increase signal counts. Generally, the first step should be to increase the dye concentration. Laser power or exposure time can be increased when dye concentration cannot be further increased (e.g., due to signal crosstalk between channels or excessive absorption of light). However, increasing the laser power and exposure time will increase photobleaching, and increasing exposure time will increase imaging times.

Table 4.1. Troubleshooting of Path3D

Step	Problem	Possible reason	Solution
Steps 21 – 24	Eosin signal is bright at sample edges but dim at the center and may be laterally asymmetric (Figure 4.5d).	Illumination light can be overly absorbed by excessive eosin staining, resulting in poor light transmission further into the tissue. This can give the appearance of poor dye penetration even when the sample is uniformly stained [75]. Depending upon the microscope configuration, this effect may result in asymmetrically bright edges: signal counts are high at surfaces facing towards the illumination beam, but low in the tissue core and surfaces facing away from the illumination beam (Figure C.7).	Reduce the eosin concentration (e.g., 1:200 dilution of alcoholic eosin). Alternatively, switch to an illumination wavelength with less efficient eosin absorption (e.g., use 561 nm, ~8% relative eosin absorption, instead of 488 nm, ~37% relative eosin absorption). Finally, one may confirm adequate dye penetration by cutting the specimen in half after staining and then imaging the cut surface *en face*.
Steps 21 – 24	Staining appears uneven in all channels (Figure 4.5c).	Tissue was not sufficiently deparaffinized, causing localized regions to remain unstained.	Refresh xylene at least once or use a higher temperature during deparaffinization.
Steps 21 – 24	The overlapping regions of adjacent imaging tiles are dimmer than the non-overlapping regions.	Sample is experiencing significant photobleaching due to excessive light exposure.	Reduce laser power, increasing staining concentration as needed (to allow for lower laser powers and/or shorter exposure times).

Table 4.1. Troubleshooting of Path3D

Step	Problem	Possible reason	Solution
Steps 21 – 24	Signal counts decrease with depth.	Illumination and/or collection light is attenuated due to imperfect clearing.	Increase clearing time and/or use multiple rounds of ECi. Note that some attenuation with depth is expected even in well-cleared specimens, especially at shorter wavelengths. If clearing cannot be further improved, one can increase the laser power with imaging depth (depending on the imaging system) to improve signal uniformity. However, this has the potential to increase photobleaching effects. Image-processing steps can also be performed to normalize/adjust the signal levels as a function of depth (if the SNR and dynamic range of the raw images allow for it). See Appendix C.13.
		Stray illumination light while imaging near the surface has photobleached deeper regions before they are imaged. To confirm presence of photobleaching, image the same sample twice and look for a global drop in signal counts between datasets.	Reduce laser power/exposure time, increasing dye concentrations as necessary to maintain adequate signal counts. Alternatively, samples may be cut into thinner pieces and imaged separately. Samples can also be imaged from deep to shallow so that photobleaching occurs most at the surface where signal counts tend to be highest.
Step 25	Image sharpness decreases with imaging depth (Figure 4.5b).	Incomplete dehydration causes scattering of illumination or collection beams.	Increase incubation time in 100% ethanol or use multiple rounds of 100% ethanol (Step 2c).

Table 4.1. Troubleshooting of Path3D

Step	Problem	Possible reason	Solution
		Incomplete clearing causes scattering of illumination or collection beams.	Increase incubation time in ECi or use multiple rounds of ECi (Step 2d).

4.5 Outline of timing

Step 1 (optional), deparaffinization: 51 hours

Step 2, tissue staining and clearing: 57 hours

Step 3 – 4, agarose phantom preparation: 9 hours

Step 5 – 6, agarose phantom imaging and quantification: variable

Step 7 – 8, tissue imaging: variable

Step 9 – 12, stitching and fusing: variable (generally several hours)

Step 13 – 18 (optional), false coloring: variable (minimal computational time)

Step 19 – 20, visualizing data: variable

Step 21- 25, quality control: variable

4.6 Anticipated results

We have employed Path3D on a range of tissue types including both human pathology tissues and preclinical animal tissues (both FF and FFPE). Here we present example results imaged with OTLS microscopy using both the standard Path3D protocol presented in this manuscript (**Figure 4.2**) and protocol variants that have been adapted for specific use cases (**Figure C.1**). We also show examples of various visualization platforms that can be used to interact with Path3D datasets (**Figure C.9** and **Figure C.10**).

4.6.1 Archived human pathology specimens using standard Path3D

The standard Path3D protocol described here works well on a variety of archived human pathology specimens and is the suggested starting point for most tissue types. For example, we have used Path3D with prostate cancer specimens of various sizes [27–30,73,77,78,111], including 3-mm punch (**Figure 4.2**a) and 1-mm core-needle (**Figure 4.2**b) biopsies. We have also used Path3D to image archived human squamous mucosa (**Figure 4.2**c) [77], colon cancer (**Figure 4.2**d), and Barrett's esophagus (**Figure 4.2**e) [9,10]. Datasets are shown with both false coloring to mimic conventional H&E staining and with standard fluorescence coloring. Volumetric datasets allow both comprehensive assessment of tissue architecture (e.g., heterogeneous glandular morphology in prostate tissue, a key prognostic indicator for prostate cancer) and visualization of individual cellular and subcellular structures (e.g., subnuclear features) at high-resolution. Three-dimensional renderings (**Figure 4.2**a-b; Video S1, available online in reference [74]), orthogonal cross sections (**Figure 4.2**b), or scrollable stacks of 2D images can be used to visualize three-dimensional tissue architecture.

4.6.2 Path3D variants for clinical and preclinical tissues

For tissue types or use cases where the standard Path3D protocol is not ideal, variants using alternative clearing and/or staining methods can be employed. For example, human lymph nodes may be prepared with a protocol variant using a SYTOX-G or propidium iodide nuclear stain and an NHS-ester cytoplasmic stain with CUBIC-HV clearing (**Figure C.1**a) [8]. Volumetric renderings and cross sections taken at different depths show changes in tissue morphology with respect to depth that would not be apparent from a single 2D histology section. We also show an unfixed head and neck cancer human surgical specimen (tongue) imaged using a rapid single-stain variant (acridine orange) without clearing (**Figure C.1**b) [114]. In this case, a surface extraction

algorithm was applied to generate a single 2D view of the irregular tissue surface from a thin 3D imaging volume. Nuclear and cytoplasmic channels were then computationally extracted from the single fluorescence channel and visualized with our standard false-coloring procedure. Finally, we show a whole mouse kidney with antibody labelling of vasculature and glomeruli using ECi clearing (**Figure C.1**c). Antibodies were delivered via *in vivo* retro-orbital injection to provide complete labelling within in a few minutes. This example uses a maximum intensity projection color-coded by depth to show kidney vasculature across the entire organ, an additional visualization option that works well for viewing sparse 3D structures as a single 2D image.

4.6.3 Viewing and interacting with Path3D datasets

Path3D datasets can be generated in standard 3D image formats (e.g., TIFF, HDF5) for use with a range of existing 3D visualization tools. The Napari interface described above, being used to visualize a false-colored prostate specimen, is shown in **Figure C.9**. **Figure C.10**a shows a false-colored esophagus specimen with overlayed pathologist annotations visualized using QuPath, an alternative open-source viewing method [9]. Custom visualization methods are also possible for specific applications. **Figure C.10**b shows a custom web-viewer developed by Ground Truth Labs being used to visualize a false-colored prostate specimen, which provides integrated grading tools to record specimen-level pathologist annotations.

4.7 Code availably

All code used in this protocol is provided on GitHub. For license information, please see the corresponding GitHub page.

PSF computation: https://github.com/LiuBiophotonicsLab/Bead_PSF_computation

FalseColor-Python: https://github.com/serrob23/falsecolor

Normalizing signal levels: https://github.com/LiuBiophotonicsLab/FixImage3D

4.8 Acknowledgements

I would like to thank the following individuals (co-authors on the published version of this chapter) who were instrumental in the development the Path3D protocol: Lindsey A. Erion Barner, Qinghua Han, Elena Baraznenok, Lydia Lan, Chetan Poudel, Gan Gao, Robert B. Serafin, Sarah S.L. Chow, Adam K. Glaser, Andrew Janowczyk, David Brenes, Hongyi Huang, Dominie Miyasato, Lawrence D. True, Soyoung Kang, Joshua C. Vaughan, and Jonathan T.C. Liu

The work in this chapter was supported by funding from the National Institutes of Health (NIH): R01EB031002 and R01CA268207 (J.T.C.L.); R00CA240681 (A.K.G.); U01CA239055, 1R01LM013864, 1U01DK133090, U01CA248226, and 2R01DK118431 (A.J.); the Pacific Northwest Prostate Cancer SPORE P50CA097186 (L.D.T); and the Indiana Center for Advanced Renal Microscopy and Molecular Imaging U54DK137328 (J.C.V. and J.T.C.L.); the National Science Foundation (NSF): 1934292 HDR: I-DIRSE-FW (J.T.C.L.) and NSF Graduate Research Fellowships DGE-1762114 (K.W.B. and L.A.E.B.); the Department of Defense (DoD) Prostate Cancer Research Program: W81XWH-20-1-0851 (J.T.C.L.) and W81XWH-18-10358 (L.D.T. and J.T.C.L.); Prostate Cancer UK: MA-ETNA19-005 (J.T.C.L.), and a Washington Research Foundation Postdoctoral Fellowship (C.P.).

I would also like to thank the following individuals for assistance with specimen collection and preparation for data presented in this manuscript: Suzanne M. Dintzis, Michael C. Haffner, Priti Lal, Chenyi Mao, Michelle M. Martinez Irizarry, Nick P. Reder, Deepti M. Reddi, Ruben M. Sandoval, Etsuo A. Susaki, and Inti Zlobec. Finally, I acknowledge the Canary Foundation and the University of Washington Center for Laboratory Animal Training Resources for providing some specimens used in this study.

Chapter 5. Future work: Assessing the prevenance of the "poorly formed gland" morphology in prostate cancer using 3D pathology

The work in this chapter describes an in-progress clinical study leveraging the 3D pathology methods described in the prior chapters to resolve ambiguities in Gleason grading of prostate cancer.

5.1 Introduction

Cancer of the prostate gland (part of the urinary and reproductive systems) is the most common cancer and second leading cause of cancer death in men* in the United States, with an estimated 299,000 new cases diagnosed and 35,000 deaths in 2024 [1]. The majority of prostate cancers are slow-growing, and in many cases may not have a significant clinical impact on the patient for years or decades. Prostate cancer also tends to be diagnosed in older patients who are more likely to have comorbidities, with 93.3% of all cases being diagnosed in patients over 55 and a median age at diagnosis of 67 years old [139]. As a result, aggressive treatment of prostate cancer is not warranted in many situations. Patients with low-risk indolent (slow-growing) disease are often candidates for "active surveillance", or regular monitoring for disease progression without immediate therapy. Conversely, patients with high-risk aggressive disease are generally disqualified from active surveillance and instead offered aggressive treatment options, such as radiation therapy or radical prostatectomy (surgical removal of the prostate). Though these treatments reduce the likelihood of metastatic disease, they carry a risk of life-altering side effects, including incontinence or impotence. Diagnosis of aggressive disease and subsequent treatment also carries a significant psychological burden for patients. Accurate stratification between high-

* Many medical statistics, including those reported here, are inadequately stratified into binary male and female groups. The term "men" is used here to reflect the categorization used in the original data, with the acknowledgement that some people who have prostates do not identify as men and vice versa.

and low-risk patients is therefore essential for effective management of prostate cancer to avoid both overtreatment of patients with indolent disease and undertreatment of patients with aggressive disease. Unfortunately, reliably distinguishing between aggressive and indolent cases remains challenging [140].

Currently, prognostic determination in prostate cancer is made in part by microscopic analysis of biopsy specimens (2D pathology), which are graded based on glandular morphology using the Gleason grading system (**Figure 5.1**) [141]. Cancerous glands are separated into one of three Gleason patterns based on glandular morphology (for historical reasons, Gleason pattern 3 is the least aggressive and Gleason pattern 5 is the most aggressive, while Gleason patterns 1 and 2 are no longer used for clinical diagnosis of cancer). Biopsies are assigned to a Gleason grade group based on the primary and secondary patterns observed by a pathologist. Distinguishing between Gleason patterns 3 (low grade) and 4 (intermediate grade) is of particular clinical importance, as patients with exclusively Gleason pattern 3 are typically candidates for active surveillance while patients with any Gleason pattern 4 component are virtually never enrolled in active surveillance.

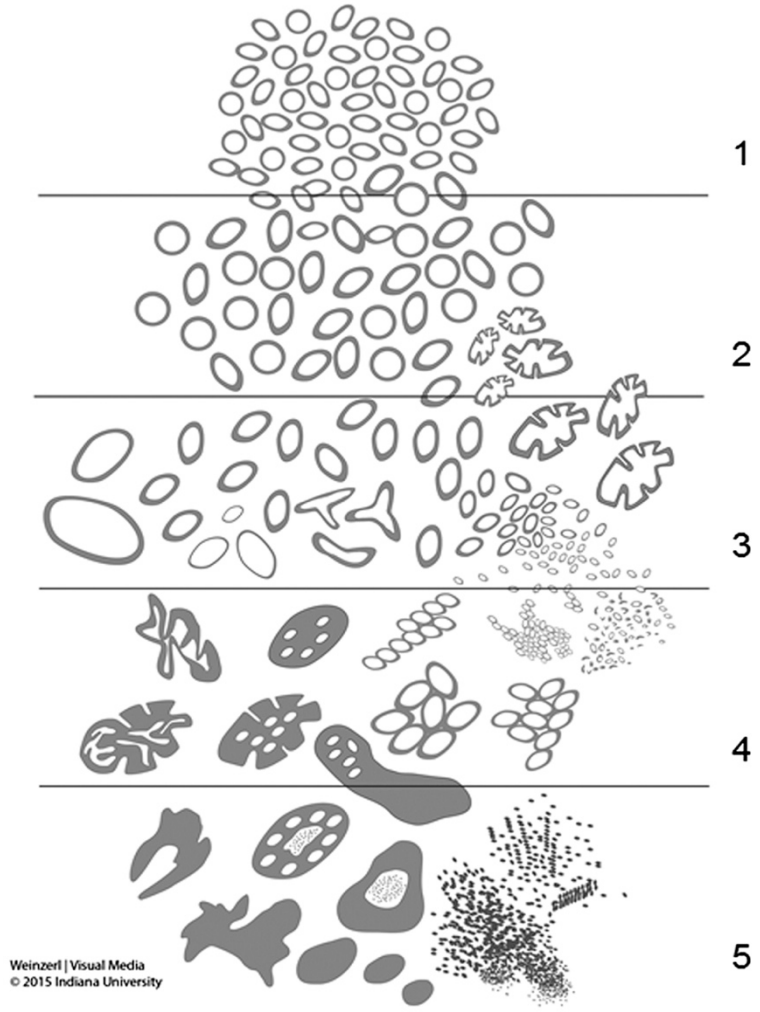


Figure 5.1. Schematic of Gleason grading system for grading of prostate cancer based on 2D glandular morphology, where higher scores indicate more aggressive disease. © The Trustees of Indiana University. Reproduced with permission.

Variable levels of interobserver disagreement when assigning Gleason grades have been well documented [142–146]. In particular, reliably distinguishing between Gleason pattern 3 and certain Gleason 4 subpatterns (and by extension, between patients who are candidates for active surveillance and those who are not) using 2D pathology remains a challenge. Separated glands with a distinct lumen are considered “well formed” and categorized as Gleason pattern 3, whereas separated glands lacking a discernible lumen are considered “poorly formed” and categorized as

Gleason pattern 4. However, if well-formed glands are tangentially sectioned through the gland wall, they can appear indistinguishable from poorly formed glands [142,143,145]. In an attempt to resolve this artifact, pathologists often apply heuristic rules to distinguish between true poorly formed glands and tangential sections of well-formed glands, such as considering the number of apparent poorly formed glands in a cluster and their proximity to nearby well-formed glands. However, even with these proxy measures, there is a lack of robust agreement among pathologists ($\kappa = 0.34$, or fair interobserver agreement) [147]. Moreover, given the lack of a reliable ground truth to identify poorly formed glands, the true prevalence of poorly formed glands relative to tangential sectioning artifacts and the absolute accuracy of these heuristic rules is unknown.

Non-destructive 3D pathology is an emerging tool to examine the 3D structure of unsectioned pathology specimens. Mounting evidence suggests that 3D pathology may provide clinically relevant insights for prostate cancer and other diseases, including resolving ambiguities in 2D Gleason grading. An early example used serial sectioning to analyze an entire prostate gland (2,678 slides). Comprehensive analysis revealed morphological heterogeneities not apparent in an initial set of 19 slides, though in this example did not alter the ultimate pathological stage [148]. More recent work leveraging 3D microscopy has aimed to assess 3D structure in addition to increasing the volume of tissue sampled. Studies by our group and others have shown examples of continuous glands that transition between distinct Gleason subpatterns (well-formed Gleason pattern 3 glands to cribriform Gleason pattern 4 glands [111], and cribriform Gleason pattern 4 glands to sheet-like Gleason pattern 5 glands [149]), suggesting that the sectioning plane may bias grading decisions in 2D pathology. Van Royen et al. provided several examples where a structure's Gleason subpattern was ambiguous in 2D but could be clearly identified in 3D [23]. Verhoef et al. characterized the three-dimensional structure of all four Gleason 4 subpatterns and two Gleason 5

subpatterns, providing a valuable starting point for developing guidance to identify each Gleason subpattern in 3D [149]. Finally, previous work from our lab has shown examples where glands appear poorly formed (Gleason pattern 4) in 2D, but 3D analysis reveals that the same structures have clear lumens in subsequent levels, indicating that these structures are tangential sectioning artifacts of well-formed (Gleason pattern 3) glands (**Figure 5.2**) [27,111,150].

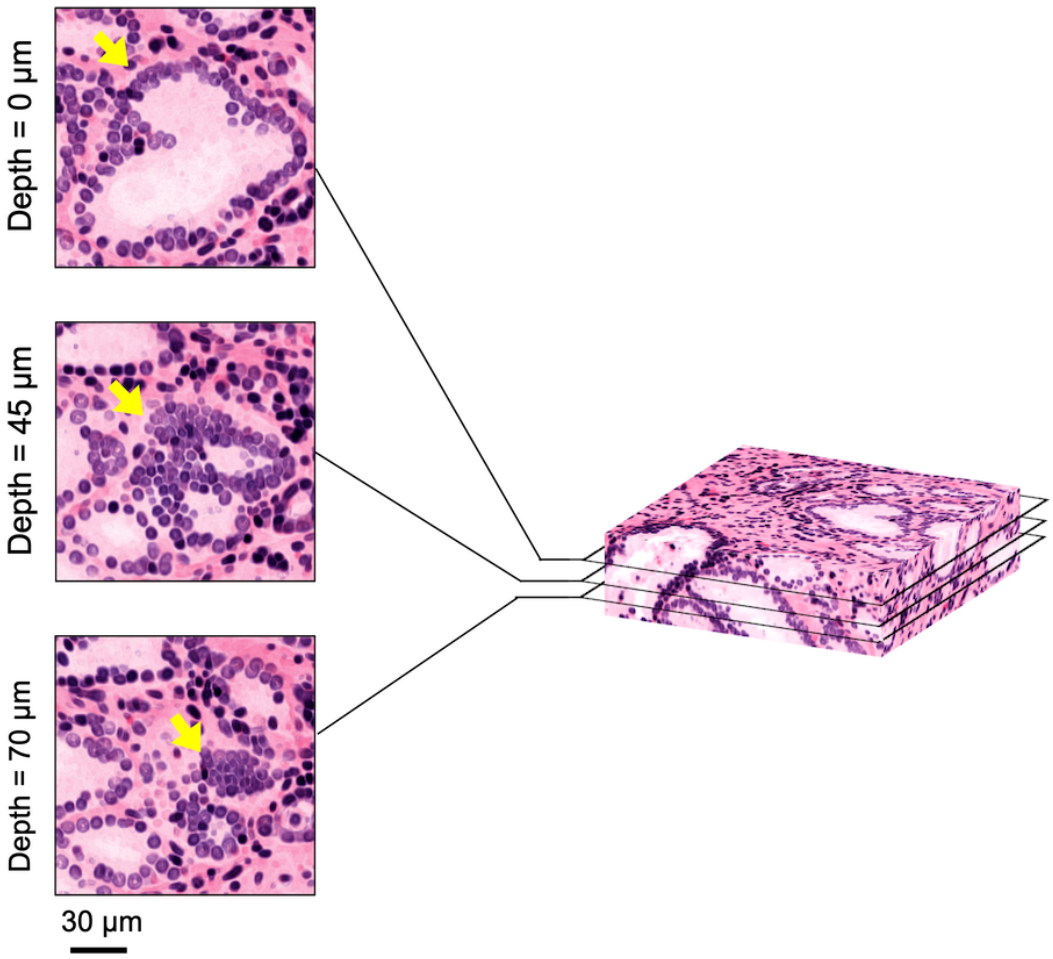


Figure 5.2. Two-dimensional cross sections taken from a 3D prostate cancer dataset. Yellow arrows indicate a gland that appears poorly formed (i.e., lacking a lumen), indicative of Gleason pattern 4, at a depth of 70 µm. Upon 3D examination, the same gland is revealed to be a tangential section of a well-formed Gleason pattern 3 gland. Adapted from [150]. CC BY 4.0.

In summary, 3D pathology provides additional structural information relative to 2D pathology, and critically can unambiguously distinguish between true poorly formed glands and tangential sectioning artifacts. Here we propose using 3D pathology to characterize the prevalence of true poorly formed glands and assess the accuracy of standard-of-care heuristic rules in distinguishing poorly formed glands from sectioning artifacts.

5.2 Methods

5.2.1 Specimen preparation and imaging with open-top light-sheet microscopy

Our lab has generated 3D pathology datasets from archived formalin-fixed paraffin-embedded (FFPE) radical prostatectomy specimens taken from 120 prostate cancer patients at University of Pennsylvania. A simulated biopsy (3-mm tissue punch) was taken from the index lesion of each specimen as identified by a practicing genitourinary pathologist. Each tissue punch was processed using a previously published protocol [74]. Briefly, specimens were deparaffinized in xylene, stained with a fluorescent analog of conventional H&E dyes (consisting of TO-PRO-3 as a nuclear dye and eosin-Y as a counter stain), and optically cleared in ethyl cinnamate (ECi) to enable high-quality optical imaging in thick tissues.

Specimens were imaged with an open-top light-sheet (OTLS) microscope using a previously described non-orthogonal dual-objective (NODO) architecture [30]. The magnification of the system's collection arm was reduced in order to increase the field of view and volumetric imaging rate (as described in [31]), yielding effective illumination and collection numerical apertures (NAs) of 0.15 NA and 0.53 NA, respectively, and a field of view 750 × 94 μm. Specimens were imaged in multiple volumetric tiles by stage-scanning in order to cover the entire specimen, and tiles were fused into a contiguous volume using BigStitcher [98]. Datasets were downsampled in all dimensions by 2×, which reduces the volumetric dataset size by 8× and, for the purpose of

human interpretation, does not appreciably impact image quality. The final effective optical resolution of each dataset is approximately 2 μm laterally and 4 μm axially. Finally, greyscale fluorescence datasets were false-colored to mimic the appearance of H&E staining using a physics-based algorithm that models absorption of light by conventional chromogenic dyes in tissue [77].

5.2.2 Selection of candidate glands

A trained researcher under the supervision of a practicing genitourinary pathologist will select 30 datasets that show potential poorly formed glands (in 2D). Candidate glands (i.e., possible poorly formed glands based on 2D morphology) will be identified from a central (simulated) 2D level taken from each these 3D datasets. Up to five candidate glands will be selected from each case, prioritizing spatial and morphological diversity and avoiding regions where morphology is ambiguous due to poor imaging quality. Candidate glands will include any gland which is separated from adjacent glands (i.e., not fused) and lacks a discernible lumen. Standard of care heuristic rules (e.g., presence of adjacent well-formed glands) to rule out sectioning artifacts will *not* be considered in selection of candidate glands. Each candidate gland will be cropped to a 100 μm × 100 μm region of interest (ROI), roughly equivalent to one field of view of a standard 20× pathology objective, and all ROIs will be randomized (i.e., not grouped by patient).

5.2.3 Pathologist annotation

Three practicing genitourinary pathologists will independently categorize each candidate gland as either a true poorly formed gland or a sectioning artifact based on both 2D and 3D analysis. First, each pathologist will view three levels, each separated by 20 μm, from each gland ROI (centered around the level used to identify the candidate gland), which corresponds to the standard of care for prostate cancer grading at the University of Washington. Pathologists will

categorize the candidate gland as either (1) a poorly formed gland or (2) a sectioning artifact of a well-formed gland based on their best clinical judgement, including standard heuristic rules.

Following a two-week washout period and randomization of ROI order, each pathologist will then view a 100 μm × 100 μm × 100 μm volume around each candidate gland (viewed as a scrollable z-stack of images sliced in the same orientation as in the 2D view). Pathologists will be asked to view the entire volume and characterize the candidate gland as either (1) a poorly formed gland or (2) a sectioning artifact of a well-formed gland. In this phase, pathologists will only consider the candidate gland's morphology and will *not* use heuristic rules that consider the morphology of adjacent glands. Here, poorly formed glands are defined as glands which lack a discernible lumen over the entire volume, whereas well-formed glands are defined as glands which show a discernible lumen at any point in the volume. Finally, pathologists will have the option to enter free-text descriptions of each dataset and will be encouraged to comment on 3D morphological characteristics of the tissue.

5.3 Anticipated results

Based on annotations above, we expect to answer three research questions:

(1) What fraction of apparent poorly formed glands are considered by pathologists to be true poorly formed glands (Gleason pattern 4) vs. sectioning artifacts (Gleason pattern 3) using standard of care methods?

(2) What fraction of apparent poorly formed glands are considered by pathologists to be true poorly formed glands (Gleason pattern 4) vs. sectioning artifacts (Gleason pattern 3) using 3D pathology?

(3) What are predominate 3D morphologies among glands which appear poorly formed in 2D sections?

Questions (1) and (2) will provide quantitative answers as to the prevalence of poorly formed glands and tangential sectioning artifacts. Crucially, if 3D pathology is assumed to provide unambiguous identification of true poorly formed glands as reported in prior studies [27,111,150], the sensitivity and specificity of 2D pathology in identifying poorly formed glands (using standard-of-care heuristic rules) can be computed. Question (3) will characterize the breadth of 3D morphologies that may appear as poorly formed glands in individual 2D sections, which is currently unknown. Specifically, we will use pathologist free-text comments to guide selection of representative 3D morphologies and generate an image atlas of 3D poorly formed glands and sectioning artifacts. We anticipate that this atlas focused on poorly formed glands will supplement existing 3D image atlases of prostate glandular morphology [111,149], eventually helping researchers and clinicians to develop standards for interpreting 3D prostate pathology datasets.

Chapter 6. Conclusion

Non-destructive 3D pathology is an emerging platform that provides comprehensive analysis of 3D tissue microstructure without destructive tissue sectioning. This approach has been explored for a number research and clinical applications. This dissertation has focused on 3D pathology to improve diagnostic and grading accuracy of cancer biopsies, which could improve treatment planning and ultimately lead to better clinical outcomes for patients. Specifically, this work has presented optimized 3D pathology technologies and workflows leveraging open-top light-sheet (OTLS) microscopy for large-scale clinical studies, which will be essential for future clinical adoption.

First, I have described a systematic simulation-based analysis of various OTLS architectures, exploring both practical and performance (optical resolution and contrast) tradeoffs in the context of cleared tissue imaging. This analysis helped identify a novel non-orthogonal dual-objective

(NODO) OTLS architecture advantageous for imaging large cleared tissues. Second, I described a NODO OTLS microscope optimized specifically for efficient imaging of clinical specimens. These tissues are often densely stained with fluorescent analogs of H&E dyes, presenting a unique imaging challenge where contrast, in addition to optical resolution, is a key driver of image quality. The optimized NODO microscope incorporates axially swept illumination to enable high-contrast imaging in these densely labeled tissues while maintaining high throughput, essential for large-scale studies. Third, I presented an end-to-end protocol covering the tissue processing, imaging, and data processing steps necessary to generate 3D pathology datasets from archived clinical specimens. This workflow includes an iterative optimization and quality control phase, informed by the needs of specific downstream applications, to ensure robust and consistent data quality across hundreds to thousands of specimens. Finally, I have described an in-progress clinical study leveraging the tools presented here exploring 3D pathology for Gleason grading of prostate cancer. The study will use 3D pathology to understand the prevalence of confounding sectioning artifacts when identifying the “poorly formed gland” Gleason subpattern. In summary, the suite of methods presented here offers a toolkit for large-scale clinical studies of 3D pathology and an important step towards eventual clinical adoption.

BIBLIOGRAPHY

1. R. L. Siegel, A. N. Giaquinto, and A. Jemal, "Cancer statistics, 2024," CA. Cancer J. Clin. **74**, 12–49 (2024).
2. J. T. C. Liu, A. K. Glaser, K. Bera, L. D. True, N. P. Reder, K. W. Eliceiri, and A. Madabhushi, "Harnessing non-destructive 3D pathology," Nat. Biomed. Eng. **5**, 203–218 (2021).
3. J. T. C. Liu, A. K. Glaser, C. Poudel, and J. C. Vaughan, "Nondestructive 3D Pathology with Light-Sheet Fluorescence Microscopy for Translational Research and Clinical Assays," Annu. Rev. Anal. Chem. **16**, annurev-anchem-091222-092734 (2023).
4. S. S.-Y. Lee, V. P. Bindokas, M. W. Lingen, and S. J. Kron, "Nondestructive, multiplex three-dimensional mapping of immune infiltrates in core needle biopsy," Lab. Invest. **99**, 1400–1413 (2019).
5. E. Olson, M. J. Levene, and R. Torres, "Multiphoton microscopy with clearing for three dimensional histology of kidney biopsies," Biomed. Opt. Express **7**, 3089–3096 (2016).
6. N. Tanaka, D. Kaczynska, S. Kanatani, C. Sahlgren, P. Mitura, A. Stepulak, A. Miyakawa, P. Wiklund, and P. Uhlén, "Mapping of the three-dimensional lymphatic microvasculature in bladder tumours using light-sheet microscopy," Br. J. Cancer **118**, 995–999 (2018).
7. N. Tanaka, S. Kanatani, R. Tomer, C. Sahlgren, P. Kronqvist, D. Kaczynska, L. Louhivuori, L. Kis, C. Lindh, P. Mitura, A. Stepulak, S. Corvigno, J. Hartman, P. Micke, A. Mezheyeuski, C. Strell, J. W. Carlson, C. Fernández Moro, H. Dahlstrand, A. Östman, K. Matsumoto, P. Wiklund, M. Oya, A. Miyakawa, K. Deisseroth, and P. Uhlén, "Whole-tissue biopsy phenotyping of three-dimensional tumours reveals patterns of cancer heterogeneity," Nat. Biomed. Eng. **1**, 796–806 (2017).
8. L. A. Barner, A. K. Glaser, C. Mao, E. A. Susaki, J. C. Vaughan, S. M. Dintzis, and J. T. C. Liu, "Multiresolution nondestructive 3D pathology of whole lymph nodes for breast cancer staging," J. Biomed. Opt. **27**, 036501 (2022).
9. L. A. Erion Barner, G. Gao, D. M. Reddi, L. Lan, W. Burke, F. Mahmood, W. M. Grady, and J. T. C. Liu, "AI-triaged 3D pathology to improve detection of esophageal neoplasia while reducing pathologist workloads," Mod. Pathol. 100322 (2023).
10. D. M. Reddi, L. A. Barner, W. Burke, G. Gao, W. M. Grady, and J. T. C. Liu, "Nondestructive 3D Pathology Image Atlas of Barrett Esophagus With Open-Top Light-Sheet Microscopy," Arch. Pathol. Lab. Med. (2023).
11. A. L. Kiemen, A. I. Damanakis, A. M. Braxton, J. He, D. Laheru, E. K. Fishman, P. Chames, C. A. Pérez, P.-H. Wu, D. Wirtz, L. D. Wood, and R. H. Hruban, "Tissue clearing and 3D reconstruction of digitized, serially sectioned slides provide novel insights into pancreatic cancer," Med **4**, 75–91 (2023).
12. D. Mayerich, L. Abbott, and B. McCORMICK, "Knife-edge scanning microscopy for imaging and reconstruction of three-dimensional anatomical structures of the mouse brain," J. Microsc. **231**, 134–143 (2008).
13. A. Li, H. Gong, B. Zhang, Q. Wang, C. Yan, J. Wu, Q. Liu, S. Zeng, and Q. Luo, "Micro-Optical Sectioning Tomography to Obtain a High-Resolution Atlas of the Mouse Brain," Science **330**, 1404–1408 (2010).
14. H. Gong, S. Zeng, C. Yan, X. Lv, Z. Yang, T. Xu, Z. Feng, W. Ding, X. Qi, A. Li, J. Wu, and Q. Luo, "Continuously tracing brain-wide long-distance axonal projections in mice at a one-micron voxel resolution," NeuroImage **74**, 87–98 (2013).

15. T. T. W. Wong, R. Zhang, C. Zhang, H.-C. Hsu, K. I. Maslov, L. Wang, J. Shi, R. Chen, K. K. Shung, Q. Zhou, and L. V. Wang, "Label-free automated three-dimensional imaging of whole organs by microtomy-assisted photoacoustic microscopy," Nat. Commun. **8**, 1386 (2017).
16. W. Yu, L. Kang, V. T. Tsang, Y. Zhang, I. H. Wong, and T. T. Wong, "Translational rapid ultraviolet-excited sectioning tomography for whole-organ multicolor imaging with real-time molecular staining," eLife (2022).
17. C. Kolluru, A. Todd, A. R. Upadhye, Y. Liu, M. Y. Berezin, F. Fereidouni, R. M. Levenson, Y. Wang, A. J. Shoffstall, M. W. Jenkins, and D. L. Wilson, "Imaging peripheral nerve micro-anatomy with MUSE, 2D and 3D approaches," Sci. Rep. **12**, 10205 (2022).
18. A. L. Kiemen, A. M. Braxton, M. P. Grahn, K. S. Han, J. M. Babu, R. Reichel, A. C. Jiang, B. Kim, J. Hsu, F. Amoa, S. Reddy, S.-M. Hong, T. C. Cornish, E. D. Thompson, P. Huang, L. D. Wood, R. H. Hruban, D. Wirtz, and P.-H. Wu, "CODA: quantitative 3D reconstruction of large tissues at cellular resolution," Nat. Methods **19**, 1490–1499 (2022).
19. H. Tu, Y. Liu, D. Turchinovich, M. Marjanovic, J. K. Lyngsø, J. Lægsgaard, E. J. Chaney, Y. Zhao, S. You, W. L. Wilson, B. Xu, M. Dantus, and S. A. Boppart, "Stain-free histopathology by programmable supercontinuum pulses," Nat. Photonics **10**, 534–540 (2016).
20. T. Yoshitake, M. G. Giacomelli, L. C. Cahill, D. B. Schmolze, H. Vardeh, B. E. Faulkner-Jones, J. L. Connolly, and J. G. Fujimoto, "Direct comparison between confocal and multiphoton microscopy for rapid histopathological evaluation of unfixed human breast tissue," J. Biomed. Opt. **21**, 126021 (2016).
21. S. Abeytunge, Y. Li, B. A. Larson, G. Peterson, E. Seltzer, R. Toledo-Crow, and M. Rajadhyaksha, "Confocal microscopy with strip mosaicing for rapid imaging over large areas of excised tissue," J. Biomed. Opt. **18**, 061227 (2013).
22. Y. K. Tao, D. Shen, Y. Sheikine, O. O. Ahsen, H. H. Wang, D. B. Schmolze, N. B. Johnson, J. S. Brooker, A. E. Cable, J. L. Connolly, and J. G. Fujimoto, "Assessment of breast pathologies using nonlinear microscopy," Proc. Natl. Acad. Sci. **111**, 15304–15309 (2014).
23. M. E. van Royen, E. I. Verhoef, C. F. Kweldam, W. A. van Cappellen, G.-J. Kremers, A. B. Houtsmuller, and G. J. L. H. van Leenders, "Three-dimensional microscopic analysis of clinical prostate specimens," Histopathology **69**, 985–992 (2016).
24. R. M. Power and J. Huisken, "A guide to light-sheet fluorescence microscopy for multiscale imaging," Nat. Methods **14**, 360–373 (2017).
25. R. McGorty, H. Liu, D. Kamiyama, Z. Dong, S. Guo, and B. Huang, "Open-top selective plane illumination microscope for conventionally mounted specimens," Opt. Express **23**, 16142–16153 (2015).
26. R. McGorty, D. Xie, and B. Huang, "High-NA open-top selective-plane illumination microscopy for biological imaging," Opt. Express **25**, 17798–17810 (2017).
27. A. K. Glaser, N. P. Reder, Y. Chen, E. F. McCarty, C. Yin, L. Wei, Y. Wang, L. D. True, and J. T. C. Liu, "Light-sheet microscopy for slide-free non-destructive pathology of large clinical specimens," Nat. Biomed. Eng. **1**, 1–10 (2017).
28. A. K. Glaser, N. P. Reder, Y. Chen, C. Yin, L. Wei, S. Kang, L. A. Barner, W. Xie, E. F. McCarty, C. Mao, A. R. Halpern, C. R. Stoltzfus, J. S. Daniels, M. Y. Gerner, P. R. Nicovich, J. C. Vaughan, L. D. True, and J. T. C. Liu, "Multi-immersion open-top light-

sheet microscope for high-throughput imaging of cleared tissues," Nat. Commun. **10**, 1–8 (2019).
29. L. A. Barner, A. K. Glaser, H. Huang, L. D. True, and J. T. C. Liu, "Multi-resolution open-top light-sheet microscopy to enable efficient 3D pathology workflows," Biomed. Opt. Express **11**, 6605 (2020).
30. A. K. Glaser, K. W. Bishop, L. A. Barner, E. A. Susaki, S. I. Kubota, G. Gao, R. B. Serafin, P. Balaram, E. Turschak, P. R. Nicovich, H. Lai, L. A. G. Lucas, Y. Yi, E. K. Nichols, H. Huang, N. P. Reder, J. J. Wilson, R. Sivakumar, E. Shamskhou, C. R. Stoltzfus, X. Wei, A. K. Hempton, M. Pende, P. Murawala, H.-U. Dodt, T. Imaizumi, J. Shendure, B. J. Beliveau, M. Y. Gerner, L. Xin, H. Zhao, L. D. True, R. C. Reid, J. Chandrashekar, H. R. Ueda, K. Svoboda, and J. T. C. Liu, "A hybrid open-top light-sheet microscope for versatile multi-scale imaging of cleared tissues," Nat. Methods **19**, 613–619 (2022).
31. K. W. Bishop, L. A. E. Barner, E. Baraznenok, L. Lan, C. Poudel, D. Brenes, R. B. Serafin, L. D. True, J. C. Vaughan, A. K. Glaser, and J. T. C. Liu, "Axially swept open-top light-sheet microscopy for densely labeled clinical specimens," Opt. Lett. **49**, 3794–3797 (2024).
32. K. W. Bishop, A. K. Glaser, and J. T. C. Liu, "Performance tradeoffs for single- and dual-objective open-top light-sheet microscope designs: a simulation-based analysis," Biomed. Opt. Express **11**, 4627–4650 (2020).
33. J. Huisken, J. Swoger, F. D. Bene, J. Wittbrodt, and E. H. K. Stelzer, "Optical Sectioning Deep Inside Live Embryos by Selective Plane Illumination Microscopy," Science **305**, 1007–1009 (2004).
34. N. Scherf and J. Huisken, "The smart and gentle microscope," Nat. Biotechnol. **33**, 815–818 (2015).
35. B.-C. Chen, W. R. Legant, K. Wang, L. Shao, D. E. Milkie, M. W. Davidson, C. Janetopoulos, X. S. Wu, J. A. Hammer, Z. Liu, B. P. English, Y. Mimori-Kiyosue, D. P. Romero, A. T. Ritter, J. Lippincott-Schwartz, L. Fritz-Laylin, R. D. Mullins, D. M. Mitchell, J. N. Bembenek, A.-C. Reymann, R. Böhme, S. W. Grill, J. T. Wang, G. Seydoux, U. S. Tulu, D. P. Kiehart, and E. Betzig, "Lattice light-sheet microscopy: Imaging molecules to embryos at high spatiotemporal resolution," Science **346**, (2014).
36. A. Kumar, Y. Wu, R. Christensen, P. Chandris, W. Gandler, E. McCreedy, A. Bokinsky, D. A. Colón-Ramos, Z. Bao, M. McAuliffe, G. Rondeau, and H. Shroff, "Dual-view plane illumination microscopy for rapid and spatially isotropic imaging," Nat. Protoc. **9**, 2555–2573 (2014).
37. P. Strnad, S. Gunther, J. Reichmann, U. Krzic, B. Balazs, G. de Medeiros, N. Norlin, T. Hiiragi, L. Hufnagel, and J. Ellenberg, "Inverted light-sheet microscope for imaging mouse pre-implantation development," Nat. Methods **13**, 139–142 (2016).
38. H.-U. Dodt, U. Leischner, A. Schierloh, N. Jährling, C. P. Mauch, K. Deininger, J. M. Deussing, M. Eder, W. Zieglgänsberger, and K. Becker, "Ultramicroscopy: three-dimensional visualization of neuronal networks in the whole mouse brain," Nat. Methods **4**, 331–336 (2007).
39. B. Migliori, M. S. Datta, C. Dupre, M. C. Apak, S. Asano, R. Gao, E. S. Boyden, O. Hermanson, R. Yuste, and R. Tomer, "Light sheet theta microscopy for rapid high-resolution imaging of large biological samples," BMC Biol. **16**, 57 (2018).
40. R. Tomer, L. Ye, B. Hsueh, and K. Deisseroth, "Advanced CLARITY for rapid and high-resolution imaging of intact tissues," Nat. Protoc. **9**, 1682–1697 (2014).

41. B. Yang, X. Chen, Y. Wang, S. Feng, V. Pessino, N. Stuurman, N. H. Cho, K. W. Cheng, S. J. Lord, L. Xu, D. Xie, R. D. Mullins, M. D. Leonetti, and B. Huang, "Epi-illumination SPIM for volumetric imaging with high spatial-temporal resolution," Nat. Methods **16**, 501–504 (2019).
42. C. Dunsby, "Optically sectioned imaging by oblique plane microscopy," Opt. Express **16**, 20306–20316 (2008).
43. M. B. Bouchard, V. Voleti, C. S. Mendes, C. Lacefield, W. B. Grueber, R. S. Mann, R. M. Bruno, and E. M. C. Hillman, "Swept confocally-aligned planar excitation (SCAPE) microscopy for high-speed volumetric imaging of behaving organisms," Nat. Photonics **9**, 113–119 (2015).
44. S. Kumar, D. Wilding, M. B. Sikkel, A. R. Lyon, K. T. MacLeod, and C. Dunsby, "High-speed 2D and 3D fluorescence microscopy of cardiac myocytes," Opt. Express **19**, 13839–13847 (2011).
45. T. Li, S. Ota, J. Kim, Z. J. Wong, Y. Wang, X. Yin, and X. Zhang, "Axial Plane Optical Microscopy," Sci. Rep. **4**, 7253 (2014).
46. M. Kumar, S. Kishore, J. Nasenbeny, D. McLean, and Y. Kozorovitskiy, "Integrated one- and two-photon scanned oblique plane illumination (SOPi) microscopy for rapid volumetric imaging," Opt. Express **26**, 13027 (2018).
47. M. Hoffmann and B. Judkewitz, "Diffractive oblique plane microscopy," Optica **6**, 1166–1170 (2019).
48. A. Millett-Sikking and A. York, "AndrewGYork/high_na_single_objective_lightsheet: Work-in-progress," (2019).
49. E. Sapoznik, B.-J. Chang, J. Huh, R. J. Ju, E. V. Azarova, T. Pohlkamp, E. S. Welf, D. Broadbent, A. F. Carisey, S. J. Stehbens, K.-M. Lee, A. Marín, A. B. Hanker, J. C. Schmidt, C. L. Arteaga, B. Yang, Y. Kobayashi, P. R. Tata, R. Kruithoff, K. Doubrovinski, D. P. Shepherd, A. Millett-Sikking, A. G. York, K. M. Dean, and R. P. Fiolka, "A versatile oblique plane microscope for large-scale and high-resolution imaging of subcellular dynamics," eLife **9**, e57681 (2020).
50. E. Remacha, E. Remacha, E. Remacha, E. Remacha, E. Remacha, L. Friedrich, J. Vermot, J. Vermot, J. Vermot, J. Vermot, J. Vermot, and F. O. Fahrbach, "How to define and optimize axial resolution in light-sheet microscopy: a simulation-based approach," Biomed. Opt. Express **11**, 8–26 (2020).
51. M. Kumar and Y. Kozorovitskiy, "Crossbill Design," (2019).
52. A. K. Glaser, Y. Wang, and J. T. C. Liu, "Assessing the imaging performance of light sheet microscopies in highly scattering tissues," Biomed. Opt. Express **7**, 454 (2016).
53. Y. Chen and J. T. C. Liu, "Optimizing the performance of dual-axis confocal microscopes via Monte-Carlo scattering simulations and diffraction theory," J. Biomed. Opt. **18**, 066006 (2013).
54. Y. Chen, D. Wang, and J. T. C. Liu, "Assessing the tissue-imaging performance of confocal microscope architectures via Monte Carlo simulations," Opt. Lett. **37**, 4495 (2012).
55. K. M. Dean, P. Roudot, E. S. Welf, G. Danuser, and R. Fiolka, "Deconvolution-free Subcellular Imaging with Axially Swept Light Sheet Microscopy," Biophys. J. **108**, 2807–2815 (2015).
56. B. Yang, Y. Wang, S. Feng, V. Pessino, N. Stuurman, and B. Huang, *High Numerical Aperture Epi-Illumination Selective Plane Illumination Microscopy* (Bioengineering, 2018).
57. A. Millett-Sikking and A. G. York, "High NA single-objective light-sheet," 20 (n.d.).

58. E. J. Botcherby, R. Juškaitis, M. J. Booth, and T. Wilson, "An optical technique for remote focusing in microscopy," Opt. Commun. **281**, 880–887 (2008).
59. E. J. Botcherby, R. Juskaitis, M. J. Booth, and T. Wilson, "Aberration-free optical refocusing in high numerical aperture microscopy," Opt. Lett. **32**, 2007–2009 (2007).
60. A. K. Glaser, K. W. Bishop, L. A. Barner, R. B. Serafin, and J. T. C. Liu, "A hybrid open-top light-sheet microscope for multi-scale imaging of cleared tissues," bioRxiv (2020).
61. J. Kim, T. Li, Y. Wang, and X. Zhang, "Vectorial point spread function and optical transfer function in oblique plane imaging," Opt. Express **22**, 11140–11151 (2014).
62. T. Chakraborty, M. K. Driscoll, E. Jeffery, M. M. Murphy, P. Roudot, B.-J. Chang, S. Vora, W. M. Wong, C. D. Nielson, H. Zhang, V. Zhemkov, C. Hiremath, E. D. De La Cruz, Y. Yi, I. Bezprozvanny, H. Zhao, R. Tomer, R. Heintzmann, J. P. Meeks, D. K. Marciano, S. J. Morrison, G. Danuser, K. M. Dean, and R. Fiolka, "Light-sheet microscopy of cleared tissues with isotropic, subcellular resolution," Nat. Methods **16**, 1109–1113 (2019).
63. F. F. Voigt, D. Kirschenbaum, E. Platonova, S. Pagès, R. A. A. Campbell, R. Kastli, M. Schaettin, L. Egolf, A. van der Bourg, P. Bethge, K. Haenraets, N. Frézel, T. Topilko, P. Perin, D. Hillier, S. Hildebrand, A. Schueth, A. Roebroeck, B. Roska, E. T. Stoeckli, R. Pizzala, N. Renier, H. U. Zeilhofer, T. Karayannis, U. Ziegler, L. Batti, A. Holtmaat, C. Lüscher, A. Aguzzi, and F. Helmchen, "The mesoSPIM initiative: open-source light-sheet microscopes for imaging cleared tissue," Nat. Methods **16**, 1105–1108 (2019).
64. J. Swoger, P. Verveer, K. Greger, J. Huisken, and E. H. K. Stelzer, "Multi-view image fusion improves resolution in three-dimensional microscopy," Opt. Express **15**, 8029–8042 (2007).
65. D. Wang, Y. Chen, Y. Wang, and J. T. C. Liu, "Comparison of line-scanned and point-scanned dual-axis confocal microscope performance," Opt. Lett. **38**, 5280–5283 (2013).
66. C. Yin, A. K. Glaser, S. Y. Leigh, Y. Chen, L. Wei, P. C. S. Pillai, M. C. Rosenberg, S. Abeytunge, G. Peterson, C. Glazowski, N. Sanai, M. J. Mandella, M. Rajadhyaksha, and J. T. C. Liu, "Miniature in vivo MEMS-based line-scanned dual-axis confocal microscope for point-of-care pathology," Biomed. Opt. Express **7**, 251–263 (2016).
67. K. M. Dean, T. Chakraborty, S. Daetwyler, J. Lin, G. Garrelts, O. M'Saad, H. T. Mekbib, F. F. Voigt, M. Schaettin, E. T. Stoeckli, F. Helmchen, J. Bewersdorf, and R. Fiolka, "Isotropic imaging across spatial scales with axially swept light-sheet microscopy," Nat. Protoc. (2022).
68. Y. Liu, A. M. Rollins, and M. W. Jenkins, "CompassLSM: axially swept light-sheet microscopy made simple," Biomed. Opt. Express **12**, 6571–6589 (2021).
69. P. N. Hedde and E. Gratton, "Selective plane illumination microscopy with a light sheet of uniform thickness formed by an electrically tunable lens," Microsc. Res. Tech. **81**, 924–928 (2018).
70. J. Ping, F. Zhao, J. Nie, T. Yu, D. Zhu, M. Liu, and P. Fei, "Propagating-path uniformly scanned light sheet excitation microscopy for isotropic volumetric imaging of large specimens," J. Biomed. Opt. **24**, 1 (2019).
71. B. Kim, M. Na, S. Park, K. Kim, J.-H. Park, E. Chung, S. Chang, and K. H. Kim, "Open-top axially swept light-sheet microscopy," Biomed. Opt. Express **12**, 2328–2338 (2021).
72. S. Park, M. Na, S. Chang, and K. H. Kim, "High-resolution open-top axially swept light sheet microscopy," BMC Biol. **21**, 248 (2023).
73. L. A. Barner, A. K. Glaser, L. D. True, N. P. Reder, and J. T. C. Liu, "Solid immersion meniscus lens (SIMlens) for open-top light-sheet microscopy," Opt. Lett. **44**, 4451 (2019).

74. K. W. Bishop, L. A. Erion Barner, Q. Han, E. Baraznenok, L. Lan, C. Poudel, G. Gao, R. B. Serafin, S. S. L. Chow, A. K. Glaser, A. Janowczyk, D. Brenes, H. Huang, D. Miyasato, L. D. True, S. Kang, J. C. Vaughan, and J. T. C. Liu, "An end-to-end workflow for nondestructive 3D pathology," Nat. Protoc. (2024).
75. M. Y. Lee, C. Mao, A. K. Glaser, M. A. Woodworth, A. R. Halpern, A. Ali, J. T. C. Liu, and J. C. Vaughan, "Fluorescent labeling of abundant reactive entities (FLARE) for cleared-tissue and super-resolution microscopy," Nat. Protoc. **17**, 819–846 (2022).
76. K. R. Weiss, F. F. Voigt, D. P. Shepherd, and J. Huisken, "Tutorial: practical considerations for tissue clearing and imaging," Nat. Protoc. **16**, 2732–2748 (2021).
77. R. Serafin, W. Xie, A. K. Glaser, and J. T. C. Liu, "FalseColor-Python: A rapid intensity-leveling and digital-staining package for fluorescence-based slide-free digital pathology," PLOS ONE **15**, e0233198 (2020).
78. W. Xie, N. P. Reder, C. F. Koyuncu, P. Leo, S. Hawley, H. Huang, C. Mao, N. Postupna, S. Kang, R. Serafin, G. Gao, Q. Han, K. W. Bishop, L. A. Barner, P. Fu, J. L. Wright, C. D. Keene, J. C. Vaughan, A. Janowczyk, A. K. Glaser, A. Madabhushi, L. D. True, and J. T. Liu, "Prostate cancer risk stratification via non-destructive 3D pathology with deep learning-assisted gland analysis," Cancer Res. canres.2843.2021 (2021).
79. R. Serafin, C. Koyuncu, W. Xie, H. Huang, A. K. Glaser, N. P. Reder, A. Janowczyk, L. D. True, A. Madabhushi, and J. T. Liu, "Nondestructive 3D pathology with analysis of nuclear features for prostate cancer risk assessment," J. Pathol. **n/a**, (n.d.).
80. A. Klingberg, A. Hasenberg, I. Ludwig-Portugall, A. Medyukhina, L. Männ, A. Brenzel, D. R. Engel, M. T. Figge, C. Kurts, and M. Gunzer, "Fully Automated Evaluation of Total Glomerular Number and Capillary Tuft Size in Nephritic Kidneys Using Lightsheet Microscopy," J. Am. Soc. Nephrol. **28**, 452–459 (2017).
81. A. Ertürk, K. Becker, N. Jährling, C. P. Mauch, C. D. Hojer, J. G. Egen, F. Hellal, F. Bradke, M. Sheng, and H.-U. Dodt, "Three-dimensional imaging of solvent-cleared organs using 3DISCO," Nat. Protoc. **7**, 1983–1995 (2012).
82. N. Renier, Z. Wu, D. J. Simon, J. Yang, P. Ariel, and M. Tessier-Lavigne, "iDISCO: A Simple, Rapid Method to Immunolabel Large Tissue Samples for Volume Imaging," Cell **159**, 896–910 (2014).
83. E. M. C. Hillman, V. Voleti, W. Li, and H. Yu, "Light-Sheet Microscopy in Neuroscience," Annu. Rev. Neurosci. **42**, 295–313 (2019).
84. E. H. K. Stelzer, F. Strobl, B.-J. Chang, F. Preusser, S. Preibisch, K. McDole, and R. Fiolka, "Light sheet fluorescence microscopy," Nat. Rev. Methods Primer **1**, 1–25 (2021).
85. S. Daetwyler and R. P. Fiolka, "Light-sheets and smart microscopy, an exciting future is dawning," Commun. Biol. **6**, 1–11 (2023).
86. V. Voleti, K. B. Patel, W. Li, C. Perez Campos, S. Bharadwaj, H. Yu, C. Ford, M. J. Casper, R. W. Yan, W. Liang, C. Wen, K. D. Kimura, K. L. Targoff, and E. M. C. Hillman, "Real-time volumetric microscopy of in vivo dynamics and large-scale samples with SCAPE 2.0," Nat. Methods **16**, 1054–1062 (2019).
87. A. Millett-Sikking and A. York, "AndrewGYork/high_na_single_objective_lightsheet: Work-in-progress," (2019).
88. J. Kim, M. Wojcik, Y. Wang, S. Moon, E. A. Zin, N. Marnani, Z. L. Newman, J. G. Flannery, K. Xu, and X. Zhang, "Oblique-plane single-molecule localization microscopy for tissues and small intact animals," Nat. Methods **16**, 853–857 (2019).

89. B. Yang, M. Lange, A. Millett-Sikking, X. Zhao, J. Bragantini, S. VijayKumar, M. Kamb, R. Gómez-Sjöberg, A. C. Solak, W. Wang, H. Kobayashi, M. N. McCarroll, L. W. Whitehead, R. P. Fiolka, T. B. Kornberg, A. G. York, and L. A. Royer, "DaXi—high-resolution, large imaging volume and multi-view single-objective light-sheet microscopy," Nat. Methods **19**, 461–469 (2022).
90. F. Crameri, G. E. Shephard, and P. J. Heron, "The misuse of colour in science communication," Nat. Commun. **11**, 5444 (2020).
91. J. D. Hunter, "Matplotlib: A 2D Graphics Environment," Comput. Sci. Eng. **9**, 90–95 (2007).
92. A. Bria and G. Iannello, "TeraStitcher - A tool for fast automatic 3D-stitching of teravoxel-sized microscopy images," BMC Bioinformatics **13**, 316 (2012).
93. J. Scholler, J. Jonsson, T. Jordá-Siquier, I. Gantar, L. Batti, B. L. Cheeseman, S. Pagès, I. F. Sbalzarini, and C. M. Lamy, "Efficient image analysis for large-scale next generation histopathology using pAPRica," 2023.01.27.525687 (2023).
94. N. The HDF Group and Q. Koziol, "HDF5-Version 1.12.0," (2020).
95. A. Miles, Jakirkham, M. Bussonnier, J. Moore, D. P. Orfanos, J. Bourbeau, A. Fulton, D. Bennett, G. Lee, Zain Patel, M. Rocklin, AWA BRANDON AWA, R. Abernathey, Saransh Chopra, M. R. B. Kristensen, E. S. De Andrade, J. Hamman, M. Durant, V. Schut, R. Dussin, Sanket Verma, Shivank Chaudhary, C. Barnes, J. Nunez-Iglesias, A. Sansal, B. Williams, B. Mohar, and C. Noyes, "zarr-developers/zarr-python: v2.16.0," (2023).
96. J. Moore, C. Allan, S. Besson, J.-M. Burel, E. Diel, D. Gault, K. Kozlowski, D. Lindner, M. Linkert, T. Manz, W. Moore, C. Pape, C. Tischer, and J. R. Swedlow, "OME-NGFF: a next-generation file format for expanding bioimaging data-access strategies," Nat. Methods **18**, 1496–1498 (2021).
97. S. Saalfeld, I. Pisarev, P. Hanslovsky, A. Champion, C. Rueden, J. Bogovic, M. Kittisopikul, and jakirkham, "saalfeldlab/n5: n5-2.5.1," (2022).
98. D. Hörl, F. Rojas Rusak, F. Preusser, P. Tillberg, N. Randel, R. K. Chhetri, A. Cardona, P. J. Keller, H. Harz, H. Leonhardt, M. Treier, and S. Preibisch, "BigStitcher: reconstructing high-resolution image datasets of cleared and expanded samples," Nat. Methods **16**, 870–874 (2019).
99. J. Schindelin, I. Arganda-Carreras, E. Frise, V. Kaynig, M. Longair, T. Pietzsch, S. Preibisch, C. Rueden, S. Saalfeld, B. Schmid, J.-Y. Tinevez, D. J. White, V. Hartenstein, K. Eliceiri, P. Tomancak, and A. Cardona, "Fiji: an open-source platform for biological-image analysis," Nat. Methods **9**, 676–682 (2012).
100. K. N. Elfer, A. B. Sholl, M. Wang, D. B. Tulman, S. H. Mandava, B. R. Lee, and J. Q. Brown, "DRAQ5 and Eosin (‘D&E’) as an Analog to Hematoxylin and Eosin for Rapid Fluorescence Histology of Fresh Tissues," PLOS ONE **11**, e0165530 (2016).
101. Y. Rivenson, K. de Haan, W. D. Wallace, and A. Ozcan, "Emerging Advances to Transform Histopathology Using Virtual Staining," BME Front. **2020**, (2020).
102. Z. Chen, W. Yu, I. H. M. Wong, and T. T. W. Wong, "Deep-learning-assisted microscopy with ultraviolet surface excitation for rapid slide-free histological imaging," Biomed. Opt. Express **12**, 5920–5938 (2021).
103. M. Boktor, B. R. Ecclestone, V. Pekar, D. Dinakaran, J. R. Mackey, P. Fieguth, and P. Haji Reza, "Virtual histological staining of label-free total absorption photoacoustic remote sensing (TA-PARS)," Sci. Rep. **12**, 10296 (2022).

104. X. Yang, B. Bai, Y. Zhang, Y. Li, K. de Haan, T. Liu, and A. Ozcan, "Virtual Stain Transfer in Histology via Cascaded Deep Neural Networks," ACS Photonics **9**, 3134–3143 (2022).
105. A. Rana, A. Lowe, M. Lithgow, K. Horback, T. Janovitz, A. Da Silva, H. Tsai, V. Shanmugam, A. Bayat, and P. Shah, "Use of Deep Learning to Develop and Analyze Computational Hematoxylin and Eosin Staining of Prostate Core Biopsy Images for Tumor Diagnosis," JAMA Netw. Open **3**, e205111 (2020).
106. M. G. Giacomelli, L. Husvogt, H. Vardeh, B. E. Faulkner-Jones, J. Hornegger, J. L. Connolly, and J. G. Fujimoto, "Virtual Hematoxylin and Eosin Transillumination Microscopy Using Epi-Fluorescence Imaging," PLOS ONE **11**, e0159337 (2016).
107. J. Ahlers, D. Althviz Moré, O. Amsalem, A. Anderson, G. Bokota, P. Boone, J. Bragantini, G. Buckley, A. Burt, M. Bussonnier, A. Can Solak, C. Caporal, D. Doncila Pop, K. Evans, J. Freeman, L. Gaifas, C. Gohlke, K. Gunalan, H. Har-Gil, M. Harfouche, K. I. S. Harrington, V. Hilsenstein, K. Hutchings, T. Lambert, J. Lauer, G. Lichtner, Z. Liu, L. Liu, A. Lowe, L. Marconato, S. Martin, A. McGovern, L. Migas, N. Miller, H. Muñoz, J.-H. Müller, C. Nauroth-Kreß, J. Nunez-Iglesias, C. Pape, K. Pevey, G. Peña-Castellanos, A. Pierré, J. Rodríguez-Guerra, D. Ross, L. Royer, C. T. Russell, G. Selzer, P. Smith, P. Sobolewski, K. Sofiiuk, N. Sofroniew, D. Stansby, A. Sweet, W.-M. Vierdag, P. Wadhwa, M. Weber Mendonça, J. Windhager, P. Winston, and K. Yamauchi, "napari: a multi-dimensional image viewer for Python," (2023).
108. P. Bankhead, M. B. Loughrey, J. A. Fernández, Y. Dombrowski, D. G. McArt, P. D. Dunne, S. McQuaid, R. T. Gray, L. J. Murray, H. G. Coleman, J. A. James, M. Salto-Tellez, and P. W. Hamilton, "QuPath: Open source software for digital pathology image analysis," Sci. Rep. **7**, 16878 (2017).
109. I. Jansen, M. Lucas, C. D. Savci-Heijink, S. L. Meijer, E. I. M. L. Liem, O. J. de Boer, T. G. van Leeuwen, H. A. Marquering, and D. M. de Bruin, "Three-dimensional histopathological reconstruction of bladder tumours," Diagn. Pathol. **14**, 25 (2019).
110. K. Liimatainen, L. Latonen, M. Valkonen, K. Kartasalo, and P. Ruusuvuori, "Virtual reality for 3D histology: multi-scale visualization of organs with interactive feature exploration," BMC Cancer **21**, 1133 (2021).
111. N. P. Reder, A. K. Glaser, E. F. McCarty, Y. Chen, L. D. True, and J. T. C. Liu, "Open-Top Light-Sheet Microscopy Image Atlas of Prostate Core Needle Biopsies," Arch. Pathol. Lab. Med. **143**, 1069–1075 (2019).
112. L. F. Horowitz, A. D. Rodriguez, A. Au-Yeung, K. W. Bishop, L. A. Barner, G. Mishra, A. Raman, P. Delgado, J. T. C. Liu, T. S. Gujral, M. Mehrabi, M. Yang, R. H. Pierce, and A. Folch, "Microdissected “cuboids” for microfluidic drug testing of intact tissues," Lab. Chip 10.1039.D0LC00801J (2021).
113. K. Bera, K. A. Schalper, D. L. Rimm, V. Velcheti, and A. Madabhushi, "Artificial intelligence in digital pathology — new tools for diagnosis and precision oncology," Nat. Rev. Clin. Oncol. **16**, 703–715 (2019).
114. G. Gao, D. Miyasato, L. A. Barner, R. Serafin, K. W. Bishop, W. Xie, A. K. Glaser, E. L. Rosenthal, L. D. True, and J. T. C. Liu, "Comprehensive surface histology of fresh resection margins with rapid open-top light-sheet (OTLS) microscopy," IEEE Trans. Biomed. Eng. **70**, 2160–2171 (2023).

115. A. Huisman, L. S. Ploeger, H. F. J. Dullens, J. T. C. Beekhuis, and P. J. van Diest, "A restaining method to restore faded fluorescence in tissue specimens for quantitative confocal microscopy," Cytometry A **71A**, 875–881 (2007).
116. J. P. Hinton, K. Dvorak, E. Roberts, W. J. French, J. C. Grubbs, A. E. Cress, H. A. Tiwari, and R. B. Nagle, "A Method to Reuse Archived H&E Stained Histology Slides for a Multiplex Protein Biomarker Analysis," Methods Protoc. **2**, 86 (2019).
117. Y. Chen, W. Xie, A. K. Glaser, N. P. Reder, C. Mao, S. M. Dintzis, J. C. Vaughan, and J. T. C. Liu, "Rapid pathology of lumpectomy margins with open-top light-sheet (OTLS) microscopy," Biomed. Opt. Express **10**, 1257–1272 (2019).
118. E. Murray, J. H. Cho, D. Goodwin, T. Ku, J. Swaney, S.-Y. Kim, H. Choi, Y.-G. Park, J.-Y. Park, A. Hubbert, M. McCue, S. Vassallo, N. Bakh, M. P. Frosch, V. J. Wedeen, H. S. Seung, and K. Chung, "Simple, Scalable Proteomic Imaging for High-Dimensional Profiling of Intact Systems," Cell **163**, 1500–1514 (2015).
119. S.-Y. Kim, J. H. Cho, E. Murray, N. Bakh, H. Choi, K. Ohn, L. Ruelas, A. Hubbert, M. McCue, S. L. Vassallo, P. J. Keller, and K. Chung, "Stochastic electrotransport selectively enhances the transport of highly electromobile molecules," Proc. Natl. Acad. Sci. **112**, E6274–E6283 (2015).
120. Y.-G. Park, C. H. Sohn, R. Chen, M. McCue, D. H. Yun, G. T. Drummond, T. Ku, N. B. Evans, H. C. Oak, W. Trieu, H. Choi, X. Jin, V. Lilascharoen, J. Wang, M. C. Truttmann, H. W. Qi, H. L. Ploegh, T. R. Golub, S.-C. Chen, M. P. Frosch, H. J. Kulik, B. K. Lim, and K. Chung, "Protection of tissue physicochemical properties using polyfunctional crosslinkers," Nat. Biotechnol. **37**, 73–83 (2019).
121. S. Zhao, M. I. Todorov, R. Cai, R. A. -Maskari, H. Steinke, E. Kemter, H. Mai, Z. Rong, M. Warmer, K. Stanic, O. Schoppe, J. C. Paetzold, B. Gesierich, M. N. Wong, T. B. Huber, M. Duering, O. T. Bruns, B. Menze, J. Lipfert, V. G. Puelles, E. Wolf, I. Bechmann, and A. Ertürk, "Cellular and Molecular Probing of Intact Human Organs," Cell **180**, 796-812.e19 (2020).
122. T. Ku, W. Guan, N. B. Evans, C. H. Sohn, A. Albanese, J.-G. Kim, M. P. Frosch, and K. Chung, "Elasticizing tissues for reversible shape transformation and accelerated molecular labeling," Nat. Methods **17**, 609–613 (2020).
123. E. A. Susaki, C. Shimizu, A. Kuno, K. Tainaka, X. Li, K. Nishi, K. Morishima, H. Ono, K. L. Ode, Y. Saeki, K. Miyamichi, K. Isa, C. Yokoyama, H. Kitaura, M. Ikemura, T. Ushiku, Y. Shimizu, T. Saito, T. C. Saido, M. Fukayama, H. Onoe, K. Touhara, T. Isa, A. Kakita, M. Shibayama, and H. R. Ueda, "Versatile whole-organ/body staining and imaging based on electrolyte-gel properties of biological tissues," Nat. Commun. **11**, 1982 (2020).
124. M. Belle, D. Godefroy, C. Dominici, C. Heitz-Marchaland, P. Zelina, F. Hellal, F. Bradke, and A. Chédotal, "A Simple Method for 3D Analysis of Immunolabeled Axonal Tracts in a Transparent Nervous System," Cell Rep. **9**, 1191–1201 (2014).
125. C. Pan, R. Cai, F. P. Quacquarelli, A. Ghasemigharagoz, A. Lourbopoulos, P. Matryba, N. Plesnila, M. Dichgans, F. Hellal, and A. Ertürk, "Shrinkage-mediated imaging of entire organs and organisms using uDISCO," Nat. Methods **13**, 859–867 (2016).
126. R. Cai, Z. I. Kolabas, C. Pan, H. Mai, S. Zhao, D. Kaltenecker, F. F. Voigt, M. Molbay, T. Ohn, C. Vincke, M. I. Todorov, F. Helmchen, J. A. Van Ginderachter, and A. Ertürk, "Whole-mouse clearing and imaging at the cellular level with vDISCO," Nat. Protoc. **18**, 1197–1242 (2023).

127. A. Laurino, A. Franceschini, L. Pesce, L. Cinci, A. Montalbano, G. Mazzamuto, G. Sancataldo, G. Nesi, I. Costantini, L. Silvestri, and F. S. Pavone, "A Guide to Perform 3D Histology of Biological Tissues with Fluorescence Microscopy," Int. J. Mol. Sci. **24**, 6747 (2023).
128. E. A. Susaki, K. Tainaka, D. Perrin, F. Kishino, T. Tawara, T. M. Watanabe, C. Yokoyama, H. Onoe, M. Eguchi, S. Yamaguchi, T. Abe, H. Kiyonari, Y. Shimizu, A. Miyawaki, H. Yokota, and H. R. Ueda, "Whole-Brain Imaging with Single-Cell Resolution Using Chemical Cocktails and Computational Analysis," Cell **157**, 726–739 (2014).
129. K. Tainaka, S. I. Kubota, T. Q. Suyama, E. A. Susaki, D. Perrin, M. Ukai-Tadenuma, H. Ukai, and H. R. Ueda, "Whole-Body Imaging with Single-Cell Resolution by Tissue Decolorization," Cell **159**, 911–924 (2014).
130. E. A. Susaki, K. Tainaka, D. Perrin, H. Yukinaga, A. Kuno, and H. R. Ueda, "Advanced CUBIC protocols for whole-brain and whole-body clearing and imaging," Nat. Protoc. **10**, 1709–1727 (2015).
131. D. Jing, S. Zhang, W. Luo, X. Gao, Y. Men, C. Ma, X. Liu, Y. Yi, A. Bugde, B. O. Zhou, Z. Zhao, Q. Yuan, J. Q. Feng, L. Gao, W.-P. Ge, and H. Zhao, "Tissue clearing of both hard and soft tissue organs with the PEGASOS method," Cell Res. **28**, 803–818 (2018).
132. Y. Liu, R. M. Levenson, and M. W. Jenkins, "Slide Over: Advances in Slide-Free Optical Microscopy as Drivers of Diagnostic Pathology," Am. J. Pathol. **192**, 180–194 (2022).
133. B. Balázs, J. Deschamps, M. Albert, J. Ries, and L. Hufnagel, "A real-time compression library for microscopy images," (2017).
134. S. Di and F. Cappello, "Fast Error-Bounded Lossy HPC Data Compression with SZ," in *2016 IEEE International Parallel and Distributed Processing Symposium (IPDPS)* (2016), pp. 730–739.
135. W. Masselink, D. Reumann, P. Murawala, P. Pasierbek, Y. Taniguchi, F. Bonnay, K. Meixner, J. A. Knoblich, and E. M. Tanaka, "Broad applicability of a streamlined ethyl cinnamate-based clearing procedure," Development **146**, dev166884 (2019).
136. S. van der Walt, J. L. Schönberger, J. Nunez-Iglesias, F. Boulogne, J. D. Warner, N. Yager, E. Gouillart, and T. Yu, "scikit-image: image processing in Python," PeerJ **2**, e453 (2014).
137. C. Gohlke, "cgohlke/tifffile: v2023.7.18," (2023).
138. C. R. Harris, K. J. Millman, S. J. van der Walt, R. Gommers, P. Virtanen, D. Cournapeau, E. Wieser, J. Taylor, S. Berg, N. J. Smith, R. Kern, M. Picus, S. Hoyer, M. H. van Kerkwijk, M. Brett, A. Haldane, J. F. del Río, M. Wiebe, P. Peterson, P. Gérard-Marchant, K. Sheppard, T. Reddy, W. Weckesser, H. Abbasi, C. Gohlke, and T. E. Oliphant, "Array programming with NumPy," Nature **585**, 357–362 (2020).
139. "Cancer of the Prostate - Cancer Stat Facts," https://seer.cancer.gov/statfacts/html/prost.html.
140. R. J. Rebello, C. Oing, K. E. Knudsen, S. Loeb, D. C. Johnson, R. E. Reiter, S. Gillessen, T. Van der Kwast, and R. G. Bristow, "Prostate cancer," Nat. Rev. Dis. Primer **7**, 1–27 (2021).
141. J. I. Epstein, L. Egevad, M. B. Amin, B. Delahunt, J. R. Srigley, P. A. Humphrey, and the G. Committee, "The 2014 International Society of Urological Pathology (ISUP) Consensus Conference on Gleason Grading of Prostatic Carcinoma: Definition of Grading Patterns and Proposal for a New Grading System," Am. J. Surg. Pathol. **40**, 244 (2016).
142. J. K. McKenney, J. Simko, M. Bonham, L. D. True, D. Troyer, S. Hawley, L. F. Newcomb, L. Fazli, L. P. Kunju, M. M. Nicolas, -Lopez Funda Vakar, X. Zhang, P. R. Carroll, J. D. Brooks, and null null, "The Potential Impact of Reproducibility of Gleason Grading in Men

With Early Stage Prostate Cancer Managed by Active Surveillance: A Multi-Institutional Study," J. Urol. **186**, 465–469 (2011).
143. C. F. Kweldam, D. Nieboer, F. Algaba, M. B. Amin, D. M. Berney, A. Billis, D. G. Bostwick, L. Bubendorf, L. Cheng, E. Compérat, B. Delahunt, L. Egevad, A. J. Evans, D. E. Hansel, P. A. Humphrey, G. Kristiansen, T. H. van der Kwast, C. Magi-Galluzzi, R. Montironi, G. J. Netto, H. Samaratunga, J. R. Srigley, P. H. Tan, M. Varma, M. Zhou, and G. J. L. H. van Leenders, "Gleason grade 4 prostate adenocarcinoma patterns: an interobserver agreement study among genitourinary pathologists," Histopathology **69**, 441–449 (2016).
144. R. B. Shah, J. Li, L. Cheng, L. Egevad, F.-M. Deng, S. W. Fine, L. P. Kunju, J. Melamed, R. Mehra, A. O. Osunkoya, G. P. Paner, S. S. Shen, T. Tsuzuki, K. Trpkov, W. Tian, X. J. Yang, and M. Zhou, "Diagnosis of Gleason Pattern 5 Prostate Adenocarcinoma on Core Needle Biopsy: An Interobserver Reproducibility Study Among Urologic Pathologists," Am. J. Surg. Pathol. **39**, 1242–1249 (2015).
145. M. Zhou, J. Li, L. Cheng, L. Egevad, F.-M. Deng, L. P. Kunju, C. Magi-Galluzzi, J. Melamed, R. Mehra, S. Mendrinos, A. O. Osunkoya, G. Paner, S. S. Shen, T. Tsuzuki, K. Trpkov, W. Tian, X. Yang, and R. B. Shah, "Diagnosis of “Poorly Formed Glands” Gleason Pattern 4 Prostatic Adenocarcinoma on Needle Biopsy: An Interobserver Reproducibility Study Among Urologic Pathologists With Recommendations," Am. J. Surg. Pathol. **39**, 1331–1339 (2015).
146. R. B. Shah, Q. Cai, M. Aron, D. M. Berney, J. C. Cheville, F.-M. Deng, J. Epstein, S. W. Fine, E. M. Genega, M. S. Hirsch, P. A. Humphrey, J. Gordetsky, G. Kristiansen, L. P. Kunju, C. Magi-Galluzzi, N. Gupta, G. J. Netto, A. O. Osunkoya, B. D. Robinson, K. Trpkov, L. D. True, P. Troncoso, M. Varma, T. Wheeler, S. R. Williamson, A. Wu, and M. Zhou, "Diagnosis of “cribriform” prostatic adenocarcinoma: an interobserver reproducibility study among urologic pathologists with recommendations," Am. J. Cancer Res. **11**, 3990–4001 (2021).
147. M. Zhou, J. Li, L. Cheng, L. Egevad, F.-M. Deng, L. P. Kunju, C. Magi-Galluzzi, J. Melamed, R. Mehra, S. Mendrinos, A. O. Osunkoya, G. Paner, S. S. Shen, T. Tsuzuki, K. Trpkov, W. Tian, X. Yang, and R. B. Shah, "Diagnosis of “Poorly Formed Glands” Gleason Pattern 4 Prostatic Adenocarcinoma on Needle Biopsy: An Interobserver Reproducibility Study Among Urologic Pathologists With Recommendations," Am. J. Surg. Pathol. **39**, 1331–1339 (2015).
148. P. A. Humphrey, "Complete histologic serial sectioning of a prostate gland with adenocarcinoma," Am. J. Surg. Pathol. **17**, 468–472 (1993).
149. E. I. Verhoef, W. A. van Cappellen, J. A. Slotman, G.-J. Kremers, P. C. Ewing-Graham, A. B. Houtsmuller, M. E. van Royen, and G. J. L. H. van Leenders, "Three-dimensional analysis reveals two major architectural subgroups of prostate cancer growth patterns," Mod. Pathol. Off. J. U. S. Can. Acad. Pathol. Inc **32**, 1032–1041 (2019).
150. J. T. Liu, S. S. Chow, R. Colling, M. R. Downes, X. Farré, P. Humphrey, A. Janowczyk, T. Mirtti, C. Verrill, I. Zlobec, and L. D. True, "Engineering the future of 3D pathology," J. Pathol. Clin. Res. **10**, e347 (2024).
151. C. A. Konopka and S. Y. Bednarek, "Variable-angle epifluorescence microscopy: a new way to look at protein dynamics in the plant cell cortex," Plant J. **53**, 186–196 (2008).
152. M. Tokunaga, N. Imamoto, and K. Sakata-Sogawa, "Highly inclined thin illumination enables clear single-molecule imaging in cells," Nat. Methods **5**, 159–161 (2008).

153. E. Sapoznik, B.-J. Chang, R. J. Ju, E. S. Welf, D. Broadbent, A. F. Carisey, S. J. Stehbens, K. Lee, A. Marín, A. B. Hanker, J. C. Schmidt, C. L. Arteaga, B. Yang, R. Kruithoff, D. P. Shepherd, A. Millett-Sikking, A. G. York, K. M. Dean, and R. P. Fiolka, "A Single-Objective Light-Sheet Microscope with 200 nm-Scale Resolution.," bioRxiv 2020.04.07.030569 (2020).
154. J. Chen and X. Intes, "Comparison of Monte Carlo methods for fluorescence molecular tomography-computational efficiency," Med. Phys. **38**, 5788–5798 (2011).
155. R. J. Crilly, W.-F. Cheong, B. Wilson, and J. R. Spears, "Forward–adjoint fluorescence model: Monte Carlo integration and experimental validation," Appl. Opt. **36**, 6513–6519 (1997).
156. A. R. Gardner, C. K. Hayakawa, and V. Venugopalan, "Coupled forward-adjoint Monte Carlo simulation of spatial-angular light fields to determine optical sensitivity in turbid media," J. Biomed. Opt. **19**, 065003 (2014).
157. H. Kirshner and D. Sage, "BIG • PSF Generator," (n.d.).

Appendix A. Performance tradeoffs for single- and dual-objective open-top light-sheet microscope designs: a simulation-based analysis

A.1 Remote focus geometric analysis and NA limits for single-objective systems

When a sample is illuminated with a non-orthogonal light sheet in a single-objective light-sheet microscopy (LSM) system, the resultant image is no longer perpendicular to the optical axis of the system. In order to form an in-focus image at the camera, a remote focus can be used to optically rectify the image at the camera plane (**Figure A.1**a) [59]. Dunsby employed this method to develop the first single-objective LSM system by combining several precursor designs [42,151,152].

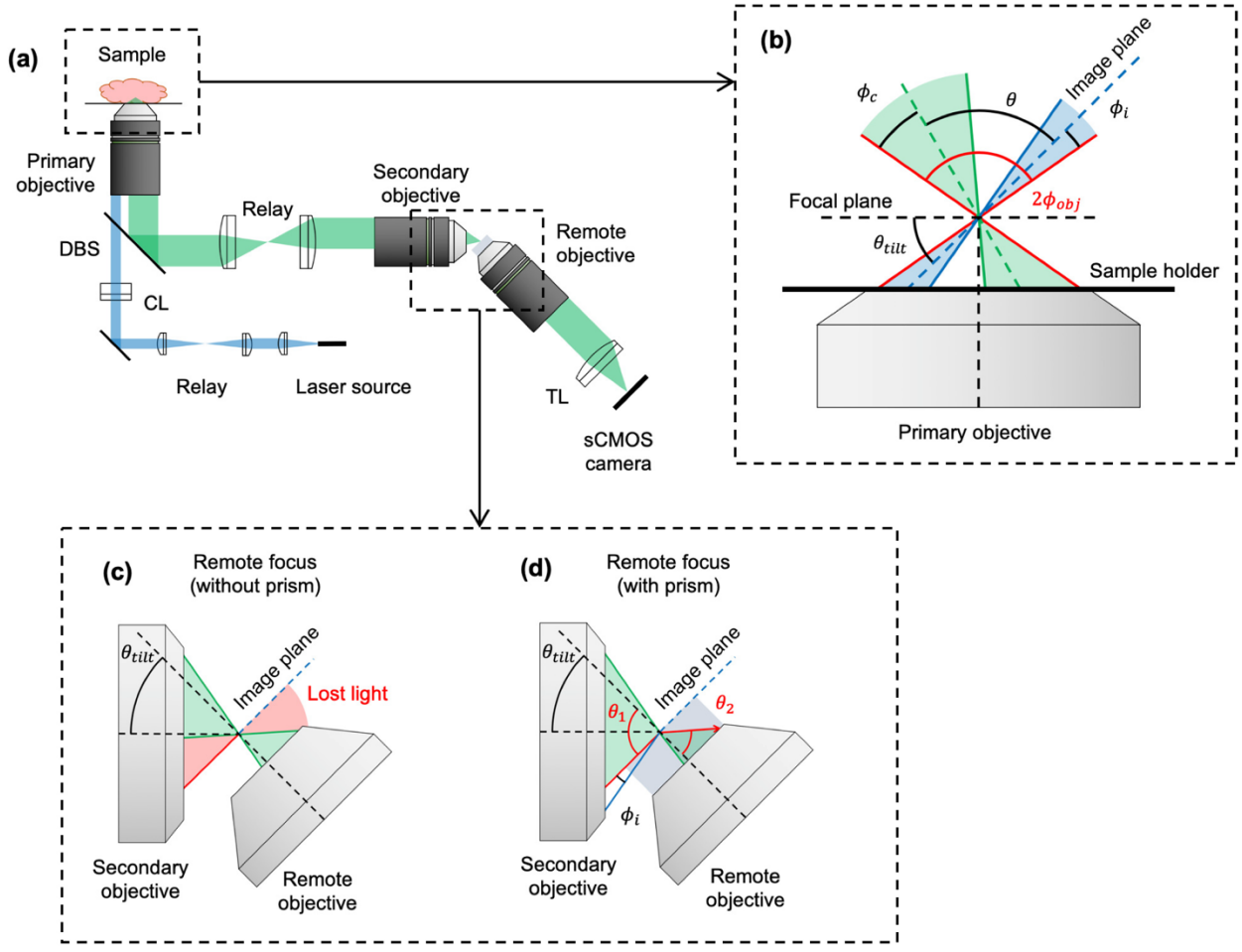


Figure A.1. (a) Optical schematic of a non-orthogonal single-objective (NOSO) LSM system, showing the illumination (blue) and collection (green) light paths. **(b)** Inset of the shared primary objective of a NOSO system showing the angled light sheet and collection path. **(c, d)** Inset of the remote focus of a NOSO system (c) without a refractive prism, showing some light is lost at the remote focus and (d) with a refractive prism, showing collection of otherwise lost light. CL: cylindrical lens, TL: tube lens, DBS: dichroic beam splitter.

From **Figure A.1**b, we see that the angle at which the light sheet is tilted relative to the focal plane in a single-objective system, θ_{tilt}, can be expressed as:

$$\theta_{tilt} = 90° - \phi_{obj} + \phi_i \quad \text{(A.1)}$$

Here, ϕ_{obj} and ϕ_i are the geometric half cone angles of the shared primary objective and the illumination cone, respectively.

Consequently, the image formed by the light-sheet-generated fluorescence is also tilted, which prevents an in-focus image from being formed on an untilted camera. An intermediate image plane is created along the collection light path using a secondary objective, essentially creating an exact 3D replica of the angled fluorescence sheet. The virtual light sheet is then imaged onto the camera by a final "remote" objective, which is physically tilted by θ_{tilt} such that it is normal to the light sheet, thus bringing the light sheet into focus at the camera chip (**Figure A.1**c). Bouchard et al. subsequently presented another single-objective LSM system, and was among several groups to present variations on Dunsby's work that laterally (rather than axially) scanned the light sheet [43,44,46]. Li et al. similarly described a variation on Dunsby's work in which a single remote objective paired with an oblique mirror allows refocusing of a plane tilted at an arbitrary angle [45].

While the systems described above allow an in-focus image to be generated from a single-objective, the tilt of the remote objective often causes a portion of the light (related to the degree of tilt) to fall outside the acceptance cone of the remote objective, thus reducing the effective collection numerical aperture (NA) of the system (**Figure A.1**c). To mitigate this NA loss, a refractive element can be placed at the image plane to refract light into the remote objective (**Figure A.1**d). The element is arranged such that the intermediate image is formed on the surface of the element and such that this image is in the focal plane of the remote objective. This principle is described with a prism below (as presented by [56,57]), but other methods such as a diffraction grating can also be used [47]. This development means that using a remote focus to correct for a tilted image plane does not by itself necessitate a reduction in collection NA (resolution and optical throughput).

To understand the extent to which a prism can mitigate NA loss, it is useful to consider the "limiting" incident angle in terms of rays that could theoretically be collected. If a prism of refractive index n_2 is placed at the front of the remote objective, which is an immersion objective designed for index n_2, then a theoretical ray incident at the limiting angle travels in the image plane (red arrow in **Figure A.1**d). This ray is incident on the prism at 90° relative to the surface normal. Applying Snell's law to such a ray gives:

$$n_{air} \sin\theta_1 = n_2 \sin\theta_2 \tag{A.2}$$

$$(1.0)\sin 90° = n_2 \sin\theta_2 \tag{A.3}$$

$$1.0 = n_2 \sin\theta_2 \tag{A.4}$$

From this equation we can find the remote objective NA necessary to collect this ray:

$$NA_{remote} = n_2 \sin\theta_2 \tag{A.5}$$

$$NA_{remote} = 1.0 \tag{A.6}$$

In theory, any remote objective with an NA of at least 1.0 can collect all rays incident at angles up to 90°, that is, all rays incident on the front surface of the prism. This is true regardless of the remote objective tilt. Any rays incident at angles larger than 90° hit the side of the prism rather than falling incident on the front surface of the prism and therefore can never be collected, regardless of the objective used. Because the ray at the limiting angle is also parallel to the central axis of the "virtual" illumination cone, this condition can be written mathematically as:

$$\phi_i + 2\phi_c \leq 2\phi_{obj} \tag{A.7}$$

This effect (also described elsewhere [56]) results in a fundamental maximum on the collection NA that may be used for a given primary objective. Note that this limit arises from sharing a primary objective, not from the remote focus itself. Equation (A.7) together with Eq. (2.4) describe the physical limits on a single objective system that we use to limit our simulation conditions. In other words, we only consider effective collection NAs that can be propagated through the system without geometric truncation (e.g., by employing a high-index prism) [47,56,57,153].

Practically speaking, light entering at such an extreme angle would suffer significant loss due to reflection (Fresnel) at the air/prism interface. The interface would also alter the polarization of the collected light, which may be undesirable. In practice, a designer would want to limit the collection light path to avoid such extreme angles. For simplicity, we will not consider these effects in our analysis, with the acknowledgment that this edge case represents a maximum limit on collection and illumination NA rather than a practical region of operation.

A.2 Resolution and contrast computation

A.2.1 Spatial resolution computation

In order to quantify spatial resolution, we computed the intensity point spread function (PSF) of each microscope configuration in MATLAB (R2019b, MathWorks, Natick, MA, USA) using the adjoint method [52,154–156]. The adjoint method is as follows. For each simulation condition, 3D intensity PSFs were first computed for the illumination and collection beams. Gaussian illumination was assumed (where NA is defined at the $1/e^2$ intensity point), along with uniform collection of angularly isotropic fluorescence emission (also at various NAs). The collection PSF was generated using a Java plugin implementing the Born and Wolf model [157]. The illumination PSF was rotated relative to the collection PSF at various crossing angles [43], and the overall system PSF (intensity) was calculated as the product of the two beams at each point in space (**Figure A.2**a). The system PSF describes the 3D spatial intensity distribution of signal that is detected from a point source of fluorescence. Note that due to the oblique crossing angle, in most cases the resultant system PSF is neither perfectly symmetric nor on-axis.

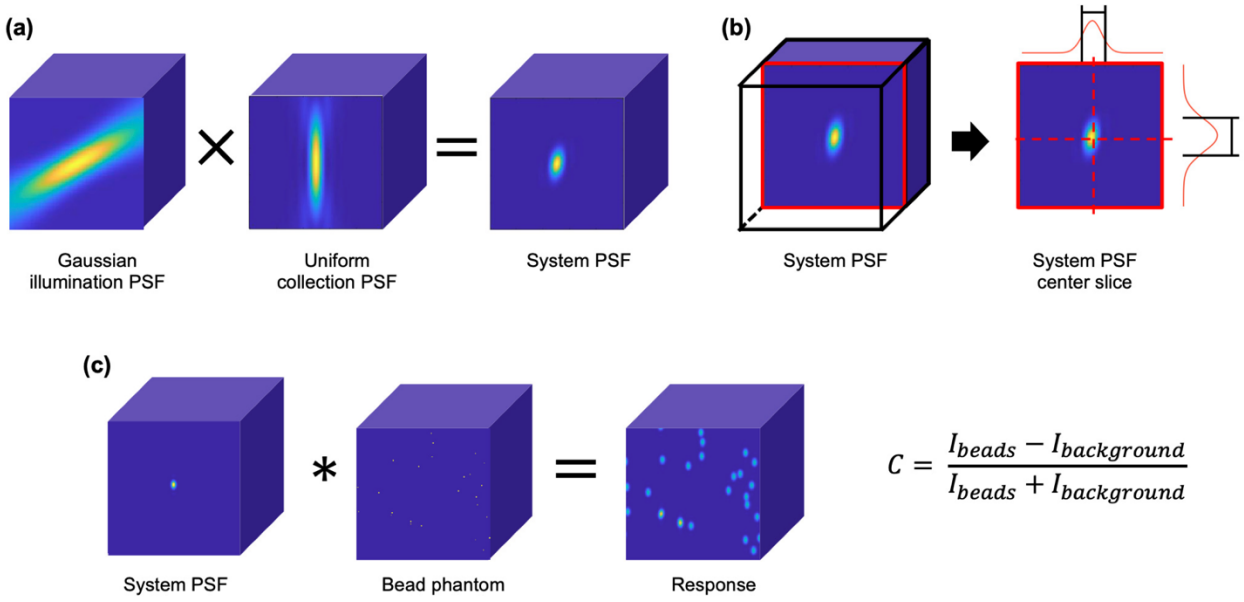


Figure A.2. Computational methods for analyzing the resolution and contrast of a given configuration. **(a)** Three-dimensional point spread functions (PSFs)

(assuming Gaussian illumination and uniform collection) are computed separately and multiplied together using the adjoint method to calculate a system PSF. **(b)** Resolution is computed by finding the full width at half maximum through the center of the system PSF in the lateral and axial directions (relative to the collection objective). **(c)** To analyze relative differences in image contrast, the system PSF is convolved with a random bead phantom, in which single voxels are set to a value of 1 to simulate diffraction-limited fluorescent beads. Relative contrast levels are then computed based on the value of the response at the locations of the beads (I_{beads}) relative to the background signal level seen in the images ($I_{background}$).

The resolution in a particular direction is defined as the full width at half maximum (FWHM) through the center of the system PSF in that direction (**Figure A.2**b). Lateral and axial resolutions are defined with respect to the collection objective, as is common for LSM. A wavelength of 500 nm was used for all simulations.

A.2.2 Contrast computation

Contrast was computed by simulating the system's response to a diffraction-limited fluorescent bead phantom. A 3D volume with a voxel pitch of 100 nm was generated. Voxels in a random subset were designated as "beads" and set to a value of 1, while all other voxels were set to a value of 0. A bead concentration of 0.5% of voxels was used for all simulations in the main text. The normalized system PSF was then convolved with this bead phantom to simulate the system's response (**Figure A.2**c). Contrast was computed as:

$$C = \frac{I_{beads} - I_{background}}{I_{beads} + I_{background}} \tag{A.8}$$

Here, C is contrast, I_{beads} is the intensity of the response averaged over all the bead locations, and $I_{background}$ is the average intensity of the response over the bottom 5% of pixels, which

adequately represents the background signal for this relatively sparse phantom. **Figure A.3** shows an example phantom and response with a 0.01% fluorescent bead concentration.

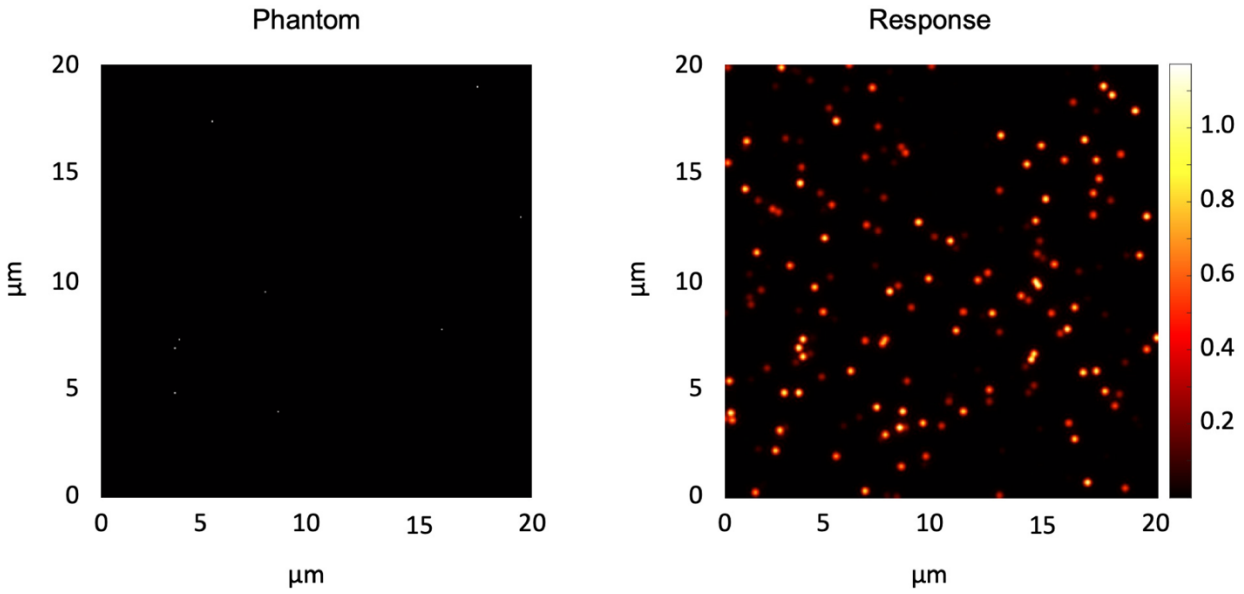


Figure A.3. Example of a diffraction-limited fluorescent bead phantom and response for contrast computation. A 0.01% bead concentration is shown for an orthogonal dual-objective (ODO) system with 0.7 collection NA and 0.2 illumination NA. Note that the figure shows a single slice of a 3D phantom, so many beads visible in the response cannot be seen in the phantom as they are in planes in front of or behind the plane shown.

For this simulated phantom, it is relevant to consider how different bead concentrations impact contrast measurements. **Figure A.4** shows contrast as a function of crossing angle for a dual-objective system computed using three different bead concentrations: 0.01%, 0.1%, and 0.5% (a, b, and c, respectively), similar to **Figure 2.8**. For simplicity, a moderate collection NA of 0.7 is used for all cases. An example phantom response for each concentration is shown below each plot (d-f). For low bead concentrations, near-perfect contrast (close to 1.0) is achieved for all configurations (a) as beads are generally well separated (d). This is representative of a sparsely

labeled sample (e.g., one stained for subnuclear features), in which axial resolution is most important. At higher bead concentrations (c), contrast varies significantly with configuration (as described previously in **Figure 2.8**) due to significant background fluorescence. In this case, strong optical sectioning [50] is critical to reject background fluorescence and yield high contrast. Such a phantom is representative of a densely labeled specimen, for instance one stained with a stromal stain such as eosin. We therefore selected a bead concentration of 0.5% for all simulations in the main text above in order to capture the impact of LSM configuration on contrast in densely labeled specimens, where contrast is a key consideration.

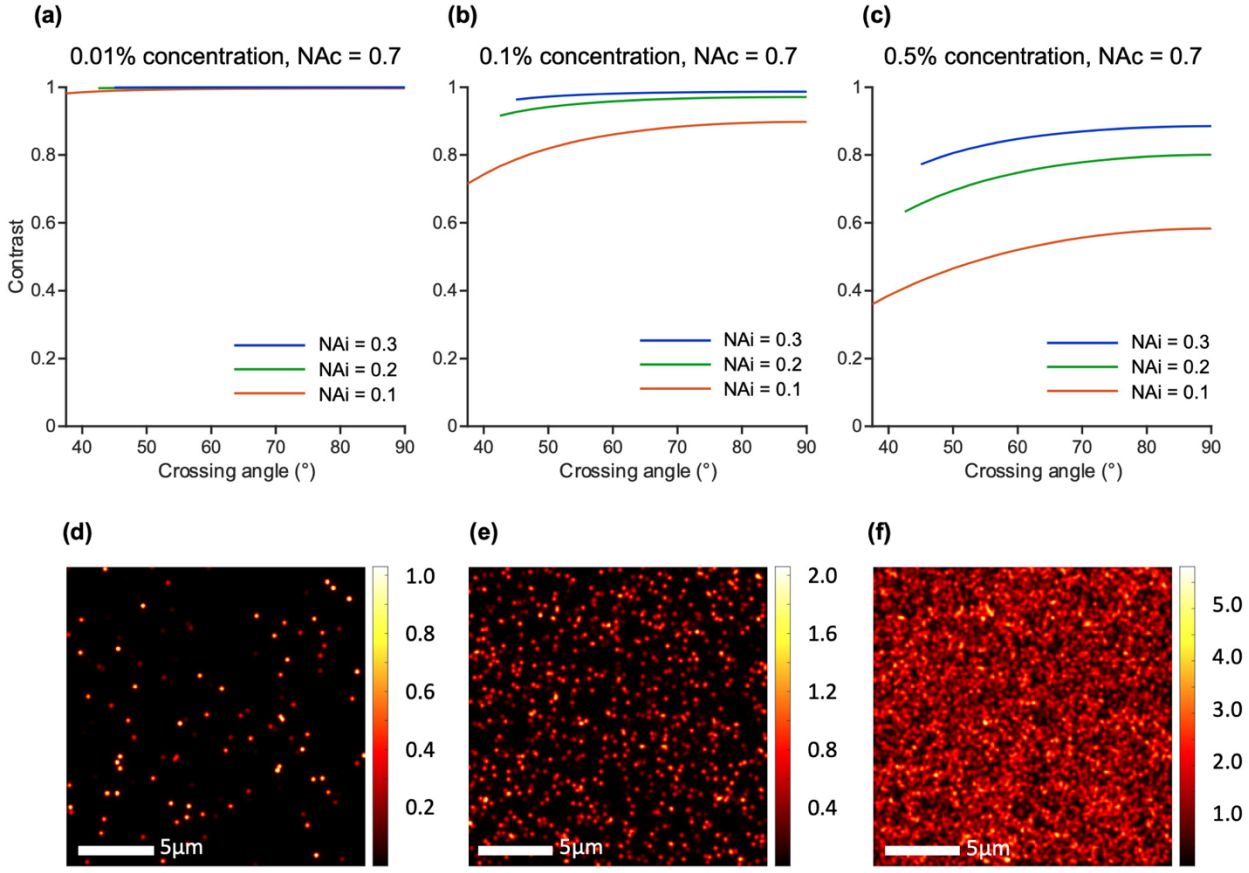


Figure A.4. Variation in contrast measurement for a dual-objective system for various bead concentrations in the simulated fluorescent phantom. **(a-c)** Impact of crossing angle on contrast for 0.01%, 0.1%, and 0.5% bead phantoms. Each plot shows contrast at three different illumination NAs (different curves). A collection

NA of 0.7 is used for all systems in this example. **(d-f)** Example phantom responses for bead concentrations of 0.01%, 0.1%, and 0.5%, respectively. Near-perfect contrast is achieved regardless of configuration at low concentrations (sparsely labeled samples; (a) and (d)) but varies significantly with configuration at higher concentrations (densely labeled samples; (c) and (f)).

A.3 Survey of commercial objectives

In order to establish an appropriate range of objective NAs to consider (collection objective NA for dual-objective systems and shared primary objective NA for single-objective systems), we surveyed relevant commercial objectives. As it would not be feasible to consider every existing microscope objective, we limited our search to those designed for, or amenable to, cleared-tissue imaging. Specifically, we considered immersion objectives compatible with refractive indices between 1.38 and 1.56, a range covering most popular clearing protocols [28]. In addition, we only considered objectives with a working distance of at least 1 mm, as shorter working distances would be impractical for volumetric imaging of many cleared-tissue specimens. Finally, we only included objectives with an NA of at least 0.4 (~1μm or better lateral resolution). Note that some specifications (magnification, NA) change with immersion index for multi-immersion objectives. In these cases, the manufacturer's nominal specification is used. The objectives identified that meet these criteria are shown in Table A.1 and range in NA from 0.4 to 1.0. As such, we used this range for our analysis.

Table A.1. Survey of commercial objectives for cleared tissue imaging

Manufacturer	Model	Mag	NA	WD (mm)	Index min	Index max	Clearance angle (°)	Housing headroom (°)
LaVision BioTec	12x NA 0.53 MI Plan - DC33 WD8.5 W	12x	0.53	8.5	1.33	1.41	42.4	20.3
LaVision BioTec	12x NA 0.53 MI Plan - DC49 WD10.9 AB	12x	0.53	10.9	1.42	1.48	39.4	18.4

Table A.1. Survey of commercial objectives for cleared tissue imaging

Manufacturer	Model	Mag	NA	WD (mm)	Index min	Index max	Clearance angle (°)	Housing headroom (°)
LaVision BioTec	12x NA 0.53 MI Plan - DC57 WD10 O	12x	0.53	10	1.49	1.57	40.3	20.6
Leica	HC FLUOTAR L 25x/1.00 IMM	25x	1.0	6	1.46	1.46	-	-
Leica	HCX APO L 20x/0.95 IMM	20x	0.95	1.95	1.56	1.56	-	-
Nikon	CFI PLAN APO 10XC Glyc	10x	0.5	5.5	1.33	1.51	63	43.7
Nikon	CFI90 20XC Glyc	20x	1.0	8.2	1.44	1.50	51.2	9.4
Olympus	XLPLN10XSVMP	10x	0.6	8	1.33	1.52	50	26.8
Olympus	XLSLPLN25XGMP	25x	1.0	8	1.41	1.52	56	14.9
Olympus	XLSLPLN25XSVMP2	25x	0.95	8	1.33	1.40	55	12.3
Olympus	XLPLN25XSVMP2	25x	1.0	4	1.33	1.40	60	14.4
Special Optics (ASI)	54-10-12	17x	0.4	12	1.33	1.56	32	16
Special Optics (ASI)	54-12-8	24x	0.7	10	1.33	1.56	37.9	9
Zeiss	Clr Plan-Apochromat 10x/0.5 nd = 1.38	10x	0.5	3.7	1.38	1.38	55.5	34.3
Zeiss	Clr Plan-Apochromat 20x/1.0 Corr nd = 1.38	20x	1.0	5.6	1.38	1.38	64.1	17.7
Zeiss	Clr Plan-Neofluar 20x/1.0 Corr nd = 1.45	20x	1.0	5.6	1.45	1.45	64.1	20.5
Zeiss	Clr Plan-Neofluor 20x/1.0 Corr nd = 1.53	20x	1.0	6.4	1.53	1.53	-	-

For each identified objective, we also identified the clearance angle of the objective's mechanical housing in order to provide a first-order approximation of which objectives could be physically positioned together (as in a dual-objective system) without colliding. We define clearance angle as the angle between the optical axis and the furthest extent of the objective's housing (with the vertex of this angle being the focal point of the objective). Clearance angles were determined based on published mechanical drawings. Three objectives had no mechanical drawing available, indicated in Table A.1 by a "-". Additionally, we computed the additional housing

"headroom" of each objective, defined as the difference between the clearance angle and the half cone angle of the objective's NA (i.e., an objective whose light cone is perfectly flush with the mechanical housing would have a housing headroom of 0°). For multi-immersion objectives with a variable cone angle, we used the maximum immersion index (maximum headroom).

The housing headroom varies significantly among objectives (from 9° at the lowest to 43.7° at the highest), making it challenging to generalize the feasibility of an objective pair, in terms of this particular constraint, based on NA alone. Further, the working distance of the objectives must be taken into account, as in some cases a long working distance can allow one objective to be positioned far enough away from the other objective that the mechanical housing permits a smaller crossing angle than suggested by the headroom parameter. It is thus important for designers to evaluate the positioning of specific candidate objectives, as there is no uniform rule for effective positioning. Lastly, we note that while consideration of mechanical housing is important, the objective housing primarily limits the minimum crossing angle in a dual-objective design. In most cases, however, operating at the minimum crossing angle is undesirable from a performance standpoint (as shown above).

A.4 PSF focal volume for various architectures

In addition to considering axial and lateral resolution separately, it is sometimes useful to consider combined resolution metrics, such as the 3D PSF volume. This can be especially relevant for samples where structures of interest do not follow a particular spatial orientation, and thus resolution in each direction is equally important. While a small and fully isotropic focal volume may be ideal, there are tradeoffs involved in optimizing focal volume (as with other metrics). **Figure A.5** compares the PSF volume of ODO, NODO (60° crossing angle), and NOSO

architectures (similar to the axial resolution comparison shown in **Figure 2.5**). The PSF volume V is computed by approximating the PSF as an ellipsoid:

$$V = \frac{4}{3}\pi R_x R_y R_z \tag{A.9}$$

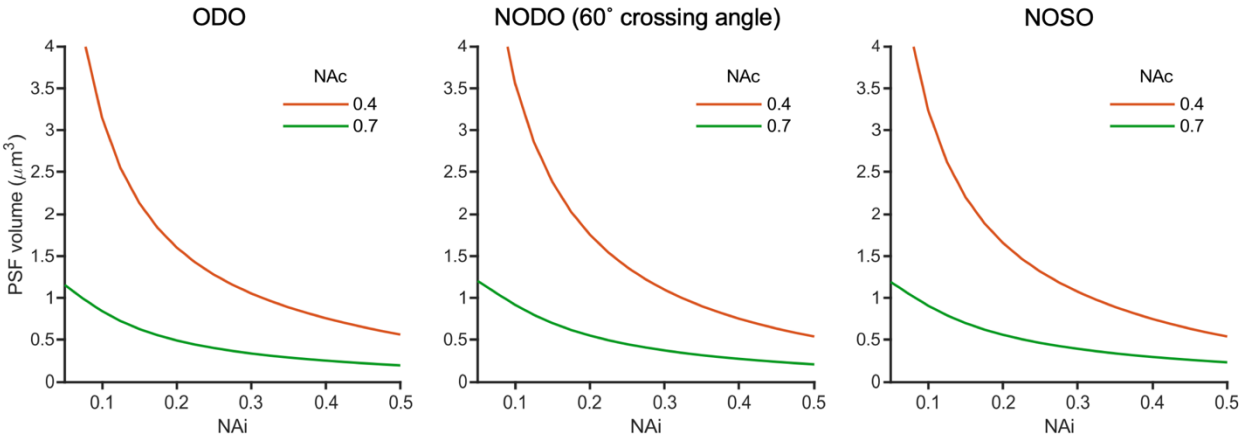


Figure A.5. Impact of illumination NA on PSF volume for **(a)** an ODO system, **(b)** a NODO system at a crossing angle of 60°, and **(c)** a NOSO system using a 1.0 NA primary objective. Collection NAs of 0.4 and 0.7 are shown. In all cases, PSF volume depends significantly on both illumination NA and collection NA. All three configurations show similar focal volume trends, indicating that architecture is not a significant driver of focal volume on its own.

Here, R_x, R_y, and R_z are the x, y, and z resolutions, respectively, as described in Appendix A.2. Unlike axial or lateral resolution, total PSF volume depends on both illumination and collection NA for all architectures, meaning that a designer must consider both parameters is combination in order to optimize total PSF volume. Further, total PSF volume is relatively similar for all architectures at a given illumination and collection NA pair, suggesting that architecture on its own is not a significant driver of focal volume. However, architecture can indirectly impact

focal volume in that different architectures have different limits on NAs that can be easily achieved, as discussed previously.

A.5 Contrast of a dual-objective system at various collection NAs

As shown in the Analysis results section, the contrast of a dual-objective system increases with crossing angle until around 60°. **Figure A.6** shows that this trend holds for other collection NAs (0.4 and 1.0). The plot for a 0.7 collection NA is also reproduced here. Note that there is slight improvement in contrast overall at higher collection NAs. This is because higher collection NAs provide some degree of additional optical sectioning, which makes the PSF in the axial direction narrower and provides a slight boost in contrast.

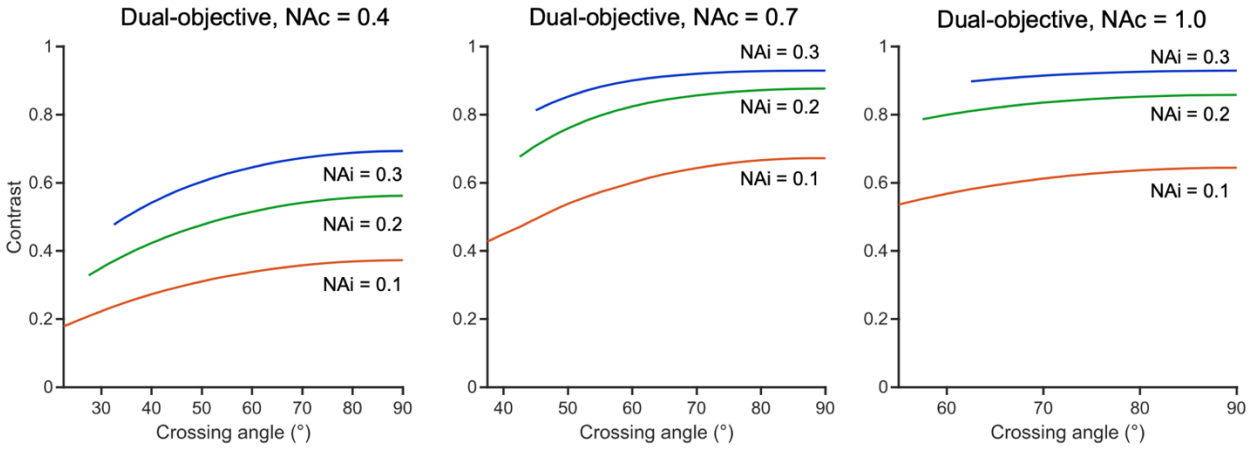


Figure A.6. Contrast of a dual-objective system as a function of crossing angle for collection NAs of 0.4, 0.7, and 1.0. In all cases, contrast improves with crossing angle until around 60°, at which point further gains are minimal. Contrast also improves slightly at higher collection NAs, as the collection objective provides some additional optical sectioning at higher NAs.

A.6 Differences in working distance between configurations for example designs

An important practical difference between the ODO, NOSO, and NODO configurations is the available working distance. The ODO configuration limits the usable working distance of the collection objective as the objective is placed at a 45° angle with respect to the sample holder (**Figure 2.1**b). In both the NOSO and NODO configurations, the objective is instead oriented perpendicularly to the sample holder such that the full working distance can be used for imaging (**Figure 2.1**d and **Figure 2.3**b). Note that in either dual-objective case (ODO or NODO), the illumination objective generally has a much longer working distance than the collection objective (as it is lower NA) and consequently does not limit the system's working distance in most cases.

Due to variability in specific objective geometry (as discussed in Appendix A.3), the difference in effective working distance between the ODO and NOSO/NODO configurations depends on which objective is used. Table A.2 shows the effective system working distance for each configuration for two example objectives from Special Optics (selected because they were designed specifically with a multi-immersion ODO LSM configuration in mind). The effective system working distance is defined in all cases as the vertical distance from the sample holder to the focal point of the collection objective.

Table A.2. Comparison of effective system working distance between ODO and NOSO/NODO configurations

Objective	ODO working distance (mm)	NOSO/NODO working distance (mm)
Special Optics 54-10-12	5.09	12
Special Optics 54-12-8	2.02	10

Appendix B. Axially swept open-top light-sheet microscopy for densely labeled clinical specimens

B.1 List of optical components

Table B.1. Optical components used in axially swept OTLS microscope

Reference	Description	Vendor & part number
–	Laser source	Hübner Photonics Cobolt Skyra
A	100 mm aspheric lens	Edmund Optics 16-277
GV_X/GV_Y	Galvo mirrors	Thorlabs GVS212
C	75 mm cylindrical lens	Thorlabs ACY254-075-A
L_1	60 mm spherical lens	Thorlabs AC254-060-A-ML
–	Voice coil actuator	Thorlabs BLINK
L_2	30 mm spherical lens	Thorlabs AC127-030-A
L_3	30 mm aspherized doublet lens	Newport APAC15
O_1	10× / 0.2 NA air objective	Nikon MUE31100
–	SIMlens	BMV Optical Technologies (custom part): 31.5 mm and 30 mm radii of curvature
O_2	26 × / 0.75 NA (RI 1.56) Multi-immersion objective	Applied Scientific Instrumentation 54-12-8
L_4	200 mm tube lens	Edmund Optics 58-520
L_5	165 mm tube lens	Thorlabs TTL165-A
O_3	20× / 0.45 NA air objective	Nikon MUE10200
O_4	20× / 0.8 NA air objective	Olympus UPLXAPO20X
FW	Filter wheel	Contains Semrock filters FF01-618/50-25 (561 nm channel) and BLP01- 647R-25 (638 nm channel)
L_6	100 mm tube lens	Thorlabs TTL100-A
–	sCMOS camera	PCO Edge 4.2

B.2 Volumetric tile size

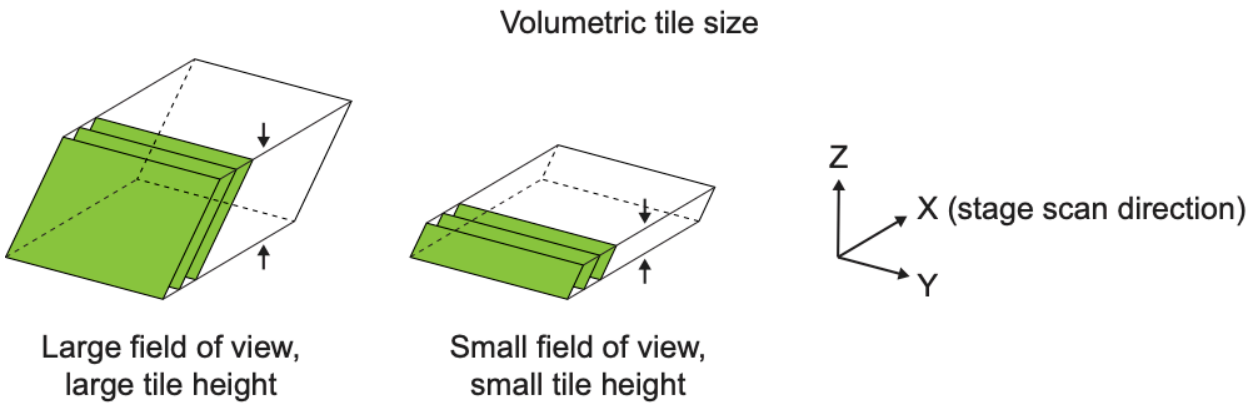


Figure B.1. Volumetric tiles are created by stage scanning the sample along the X axis through a stationary field of view (determined by the width and depth-of-focus

of the illumination light sheet). The volumetric tile width and height (YZ cross section) are determined by the field of view, and the depth (X dimension) is determined by the scan extent. Imaging larger tiles decreases the total number of tiles required to cover a given volume, reducing the number of overlapping seams (redundantly imaged regions). Fewer seams significantly reduces the computational time required to fuse tiles into a contiguous 3D volume and reduces stitching artifacts.

B.3 Ray-trace optical simulation

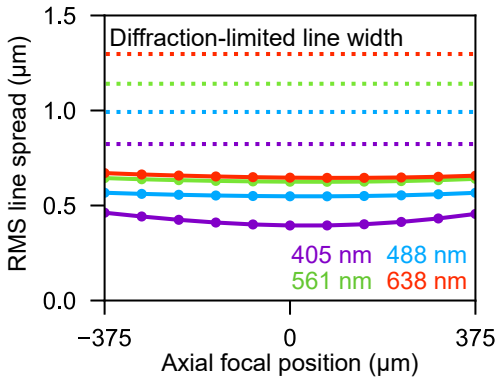


Figure B.2. A ray-trace simulation of the illumination arm was performed Zemax OpticStudio to validate the voice-coil-based axial sweeping method. The solid curves show the RMS line spread (half width) at the illumination light sheet beam waist for each wavelength (i.e., the spread due to geometric aberrations alone). The dotted lines show the diffraction-limited half line width (i.e., without aberrations). The line spread is below the diffraction-limited line width across the axial focal range for each wavelength, indicating near-diffraction-limited performance. O_1 was modeled based on US patent 9001420B2. Models for the remaining lenses were obtained from their manufacturers.

Appendix C. An end-to-end workflow for nondestructive 3D pathology

C.1 Image atlas of clinical and preclinical tissues processed with variants of the standard Path3D protocol

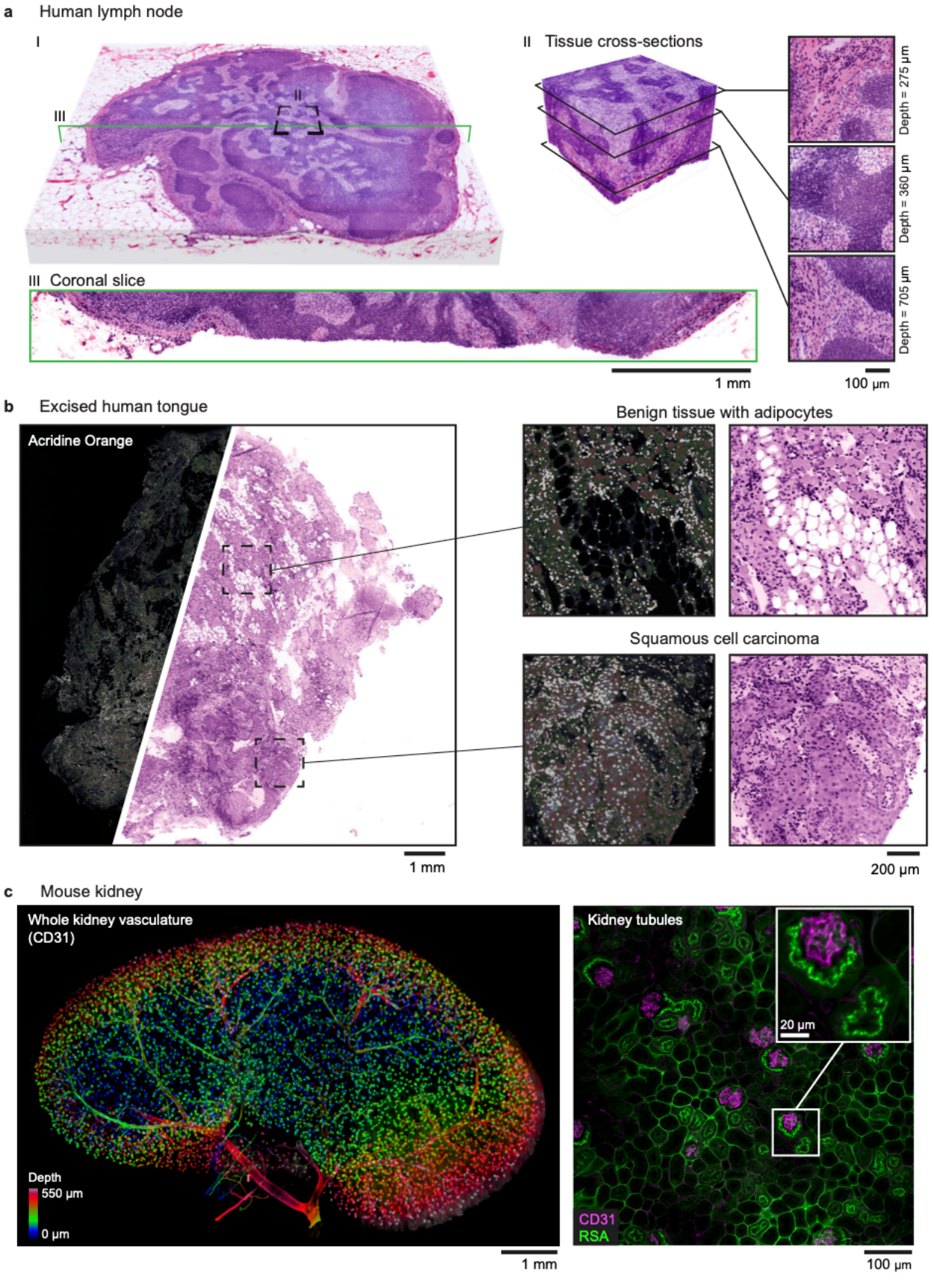

a Human lymph node
I
II
III
II Tissue cross-sections
Depth = 275 µm
Depth = 360 µm
Depth = 705 µm
III Coronal slice
1 mm
100 µm
b Excised human tongue
Acridine Orange
Benign tissue with adipocytes
Squamous cell carcinoma
1 mm
200 µm
c Mouse kidney
Whole kidney vasculature
(CD31)
Depth
550 µm
0 µm
Kidney tubules
20 µm
CD31
RSA
1 mm
100 µm

Figure C.1. Image atlas of clinical and preclinical tissues processed with variants of the standard Path3D protocol. **(a)** Fixed human lymph node prepared with a CUBIC-clearing-based Path3D variant [8] and false colored to mimic the appearance of standard H&E staining, shown as volumetric renderings (generated using Aivia) and 2D cross sections. **(b)** Fresh human head & neck cancer surgical specimen (tongue) prepared using a single-stain (acridine orange) Path3D variant without clearing. A single 2D view of the irregular tissue surface was computationally extracted from a thin 3D volume. Nuclear and cytoplasmic channels were computationally separated and false colored to mimic the appearance of standard H&E staining [114]. **(c)** Whole mouse kidney with vasculature and glomeruli labelled with antibodies delivered via *in vivo* retro-orbital injection and cleared with ECi. A maximum intensity projection color-coded by depth (left) allows visualization of the whole kidney vasculature in a single image.

C.2 Photos showing agarose bead phantom preparation

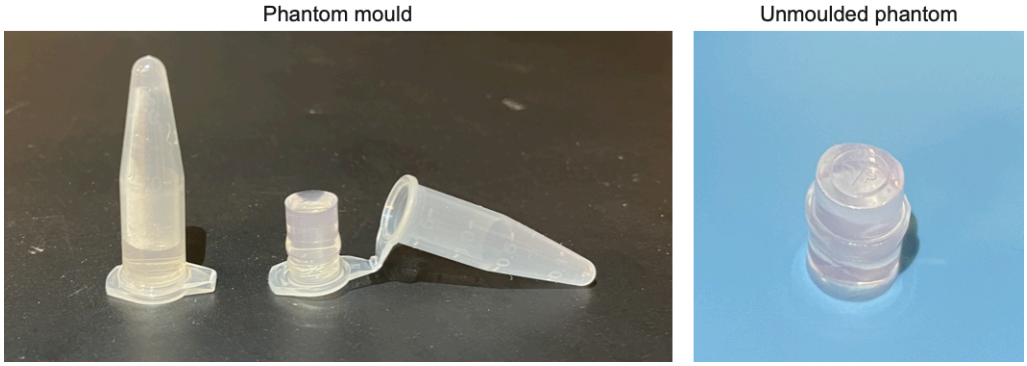


Figure C.2. Photos showing agarose bead phantom preparation. Phantoms molded in inverted microcentrifuge tubes (step 3F) form flat-bottomed cylindrical plugs, which are convenient for use with inverted or open-top microscopes with a planar sample holder.

C.3 Example scatter plot illustrating local vs. global PSF variations

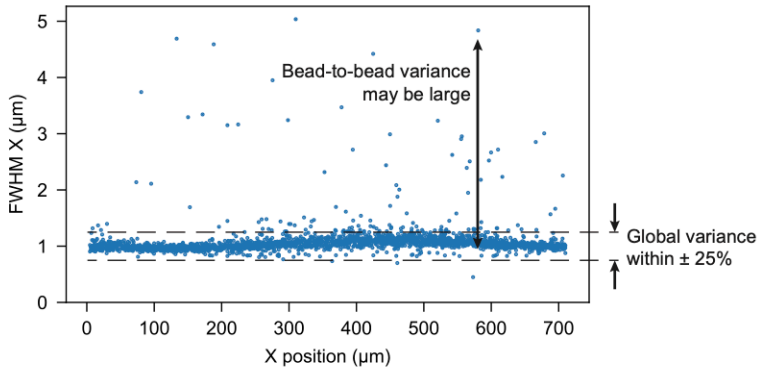


Figure C.3. Example scatter plot illustrating local vs. global PSF variations. The plot was produced by the Bead_PSF_computation package (step 6) and shows individual beads in a volumetric agarose phantom dataset. Scatter plots show how a microscope's lateral resolution (FHWM of individual beads) changes across the field of view (X position). Well-aligned microscopes should have a global variance (i.e., average FWHM values in one region relative to another) of 25% or less. Due uncertainty inherent in measuring the FWHM of diffraction-limited beads, there may be significantly higher variance between individual beads.

C.4 PSF heatmaps of well-aligned vs. misaligned microscopes

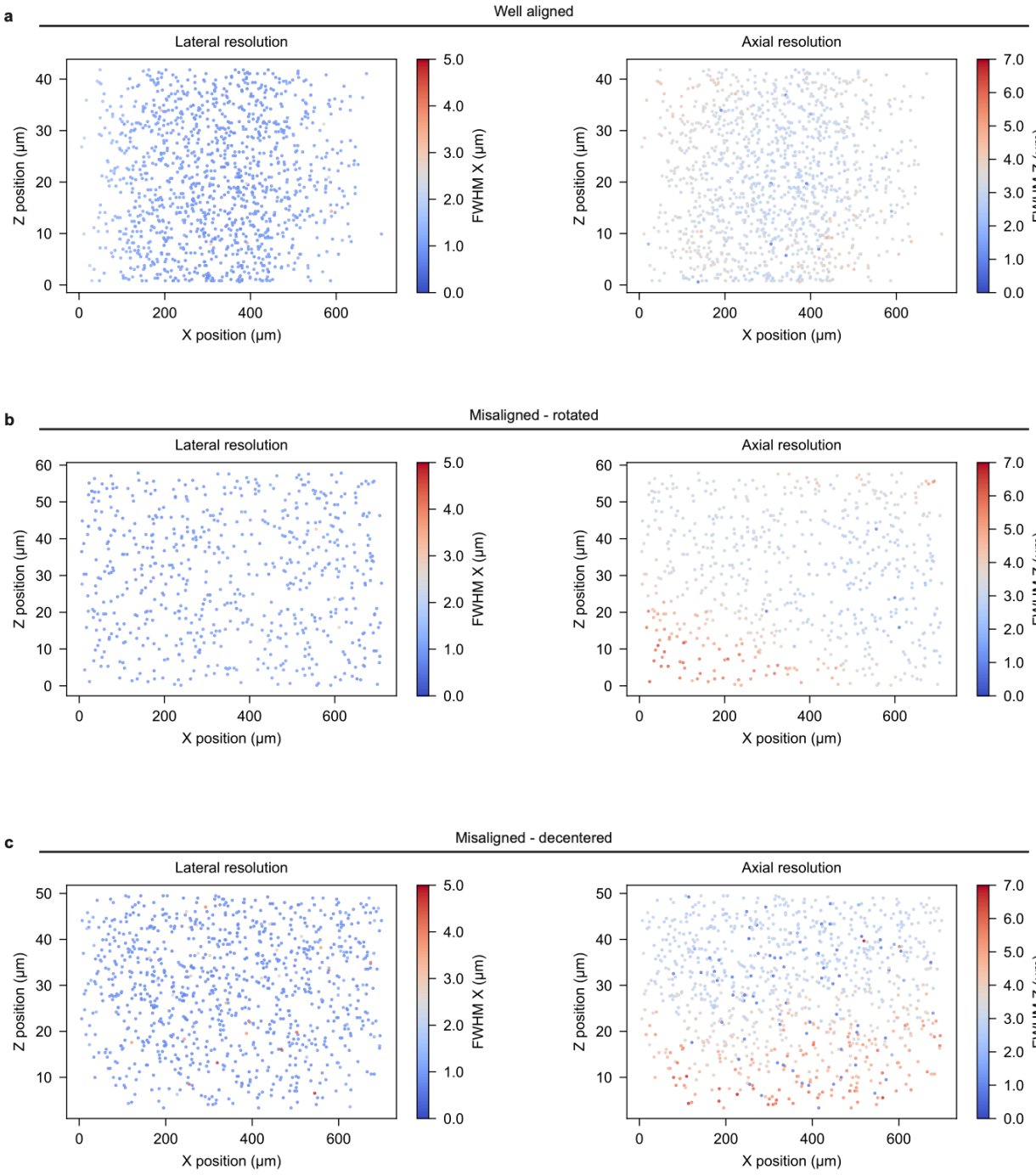


Figure C.4. PSF heatmaps of well-aligned vs. misaligned microscopes. Heat maps were generated with the Bead_PSF_computation package (step 6) from example agarose bead datasets and show how a microscope's resolution varies across the field of view (FOV). Each point represents a single diffraction-limited bead. The bead's position indicates its location in the FOV (XZ plane in this case), while the

color indicates the full width at half maximum (FWHM) of the fit Gaussian function in the lateral or axial direction. In the well-aligned case, **(a)** there is minimal variation in resolution across the FOV. In the rotated case, **(b)** the axial resolution is degraded in the lower left and upper right corners of the FOV, suggesting the light-sheet focus is rotated relative to the camera. In the decentered case, **(c)** the axial resolution at the bottom of the FOV is degraded relative to the top of the FOV, indicating the light-sheet focus is not centered within the FOV. Note that a perceptually uniform diverging colormap [90] (Matplotlib [91], "coolwarm") is used, such that beads near the center of the FWHM range appear dull and beads at the edges of the range appear brightly colored. This was selected intentionally to accentuate regions of particularly poor resolution, as these regions are typically the most informative for assessing resolution uniformity.

C.5 Identifying peak signal level, background level, and noise level

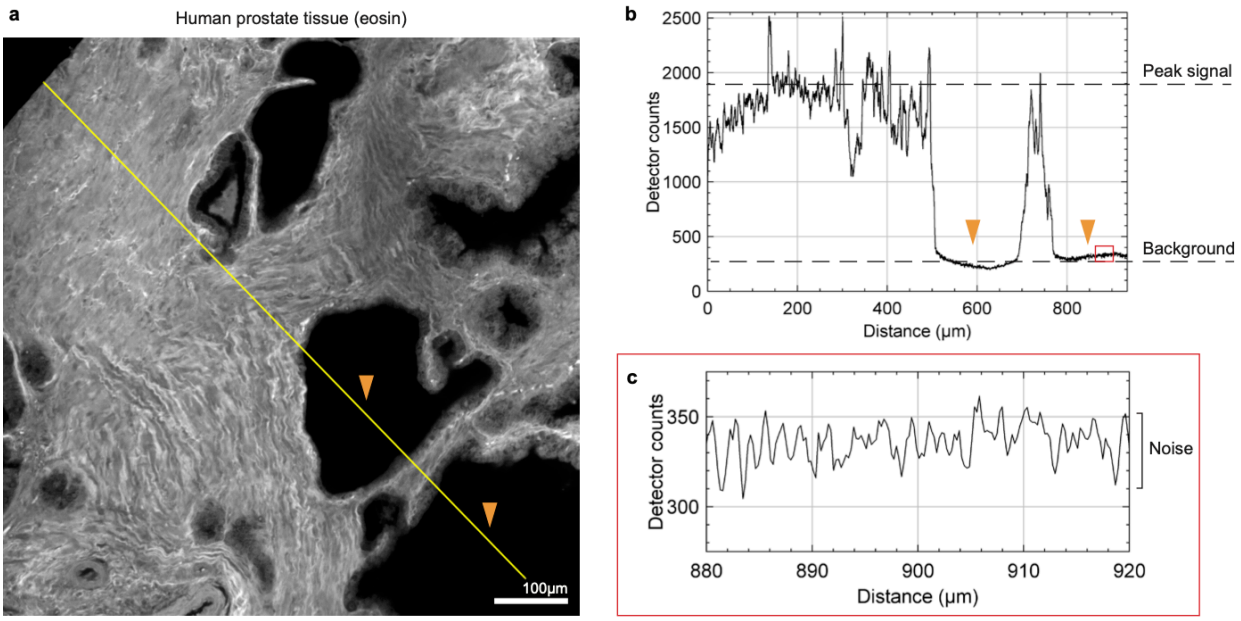


Figure C.5. Identifying peak signal level, background level, and noise level**. (a)** Human prostate tissue with eosin staining. **(b)** Profile of yellow line shown in (a) indicating peak signal level and background level. Empty gland lumens indicated by orange arrows in (a) show up as regions of background signal in (b). **(c)** Zoom in of a background region indicated by red box in (b) shows random noise level.

C.6 False coloring settings

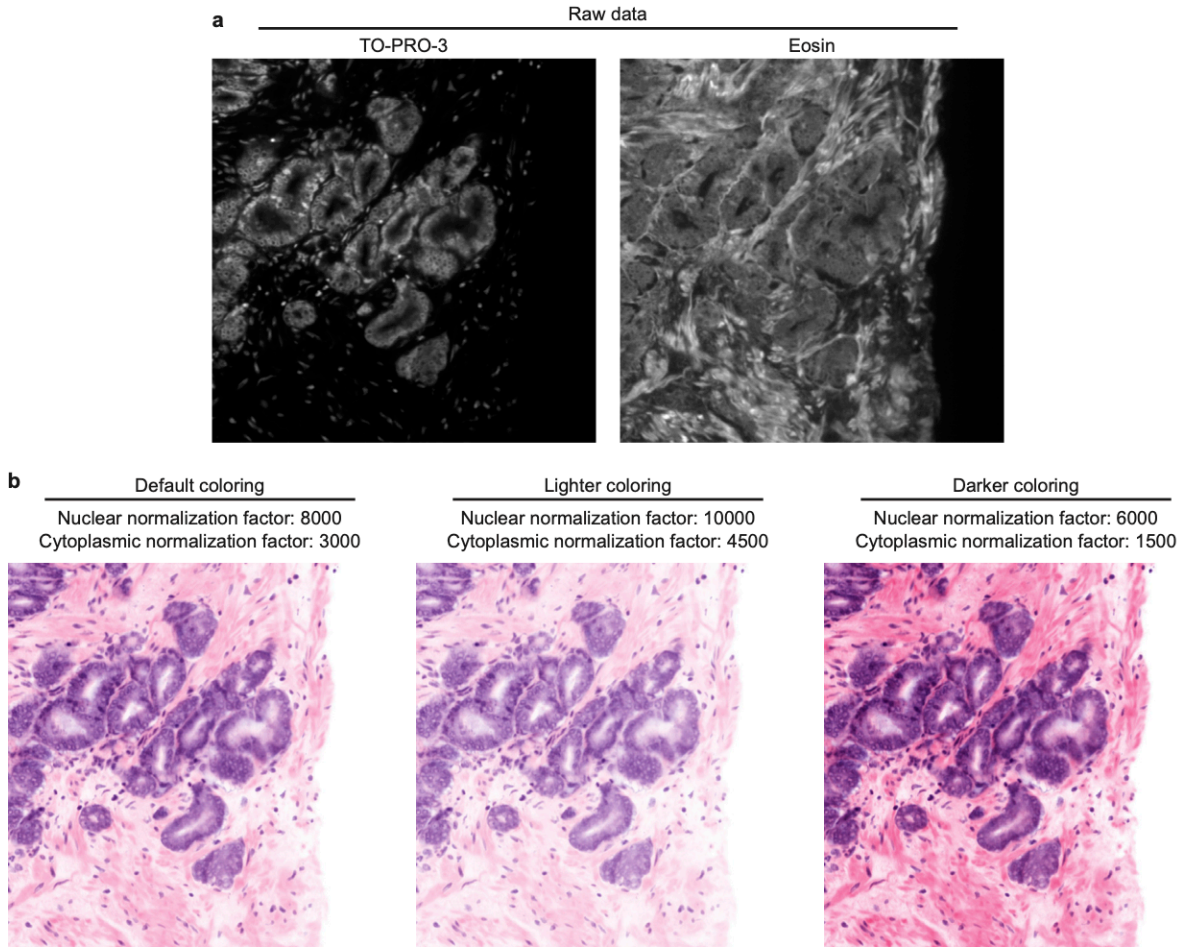


Figure C.6. False coloring settings. The same raw fluorescence data, **(a)** can be used to generate false-colored data with a range of appearances, **(b)** by adjusting the color parameters (such as normalization factors) in FalseColor Python (step 18).

C.7 Schematic of beam paths for troubleshooting

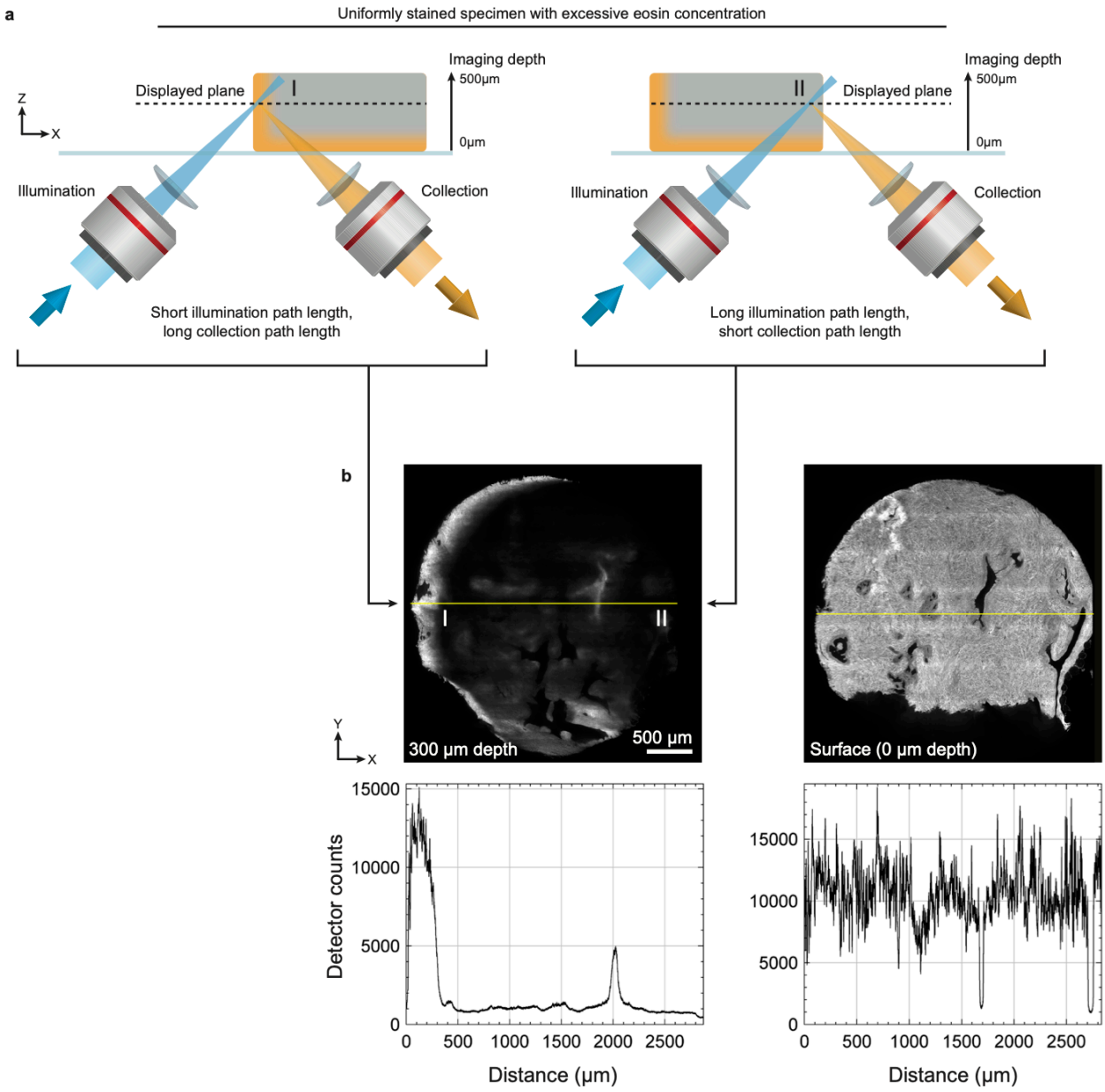


Figure C.7. Schematic of beam paths for troubleshooting. Understanding light paths of a given microscope can be useful to troubleshoot image quality issues. **(a)** In this example, a uniformly stained specimen is imaged on an open-top light-sheet (OTLS) microscope. Due to excessive eosin concentration, illumination light is rapidly attenuated by dye absorption at the tissue surface. This results in bright signal at the edges facing the illumination beam (I) and low signal at the tissue core and edges facing away from the illumination beam (II). **(b)** Upon initial inspection, *en face* views of the dataset can give the appearance of poor dye penetration,

illumination light attenuation, or collection light attenuation. However, evaluation of light paths reveals that high signal is seen in areas of short illumination path length in tissue (I) and that low signal is seen in areas of long illumination path length in tissue (II), suggesting that illumination attenuation due to excessive dye concentration is the culprit.

C.8 Photos showing visual appearance of tissue after tissue preparation problems

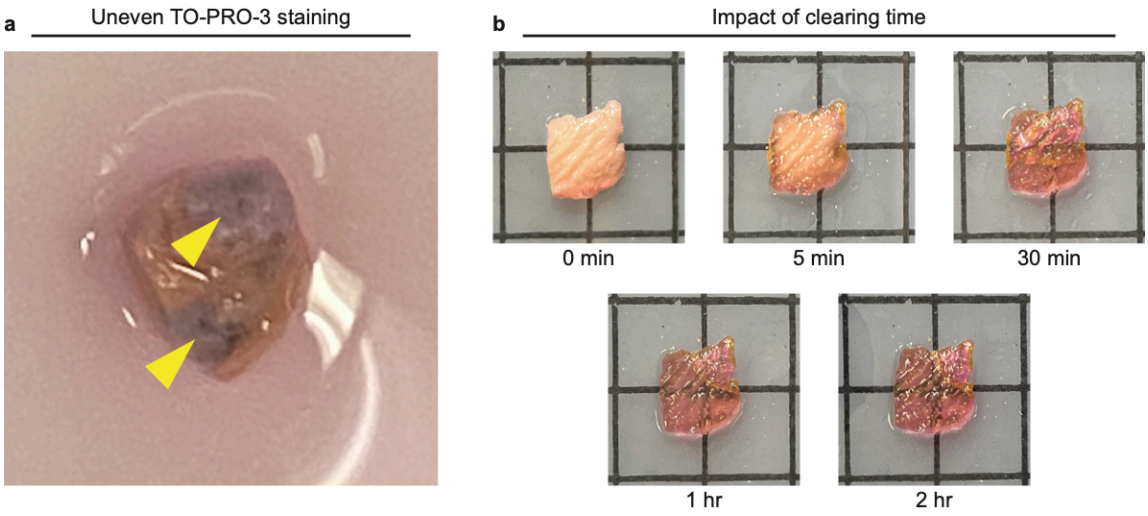


Figure C.8. Photos showing visual appearance of tissue after tissue preparation problems. **(a)** Uneven TO-PRO-3 staining of a human prostate specimen results in visible dark patches on the tissue surface (yellow arrows). **(b)** Mouse flank skin specimen shown after increasing amounts of time in ECi clearing medium. Short clearing times result in a relatively opaque specimen. By 2 hours of clearing, the specimen is relatively transparent and suitable for imaging.

C.9 Napari interface for interacting with Path3D data.

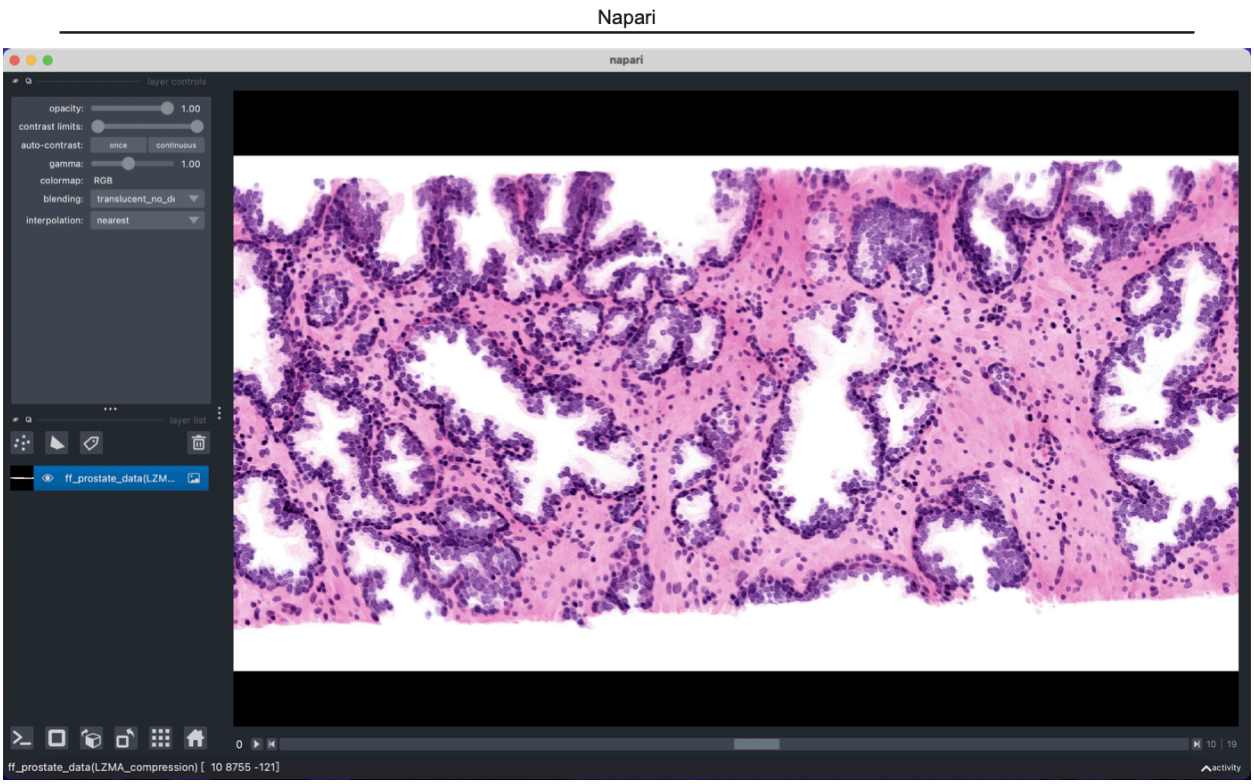


Figure C.9. Napari interface for interacting with Path3D data. Napari viewer (steps 19 - 20), showing a false-colored Path3D dataset of a human prostate core needle specimen. The interface allows users to pan, zoom, and scroll to different depth levels, as well as add annotations.

C.10 Alternative interfaces for interacting with Path3D data

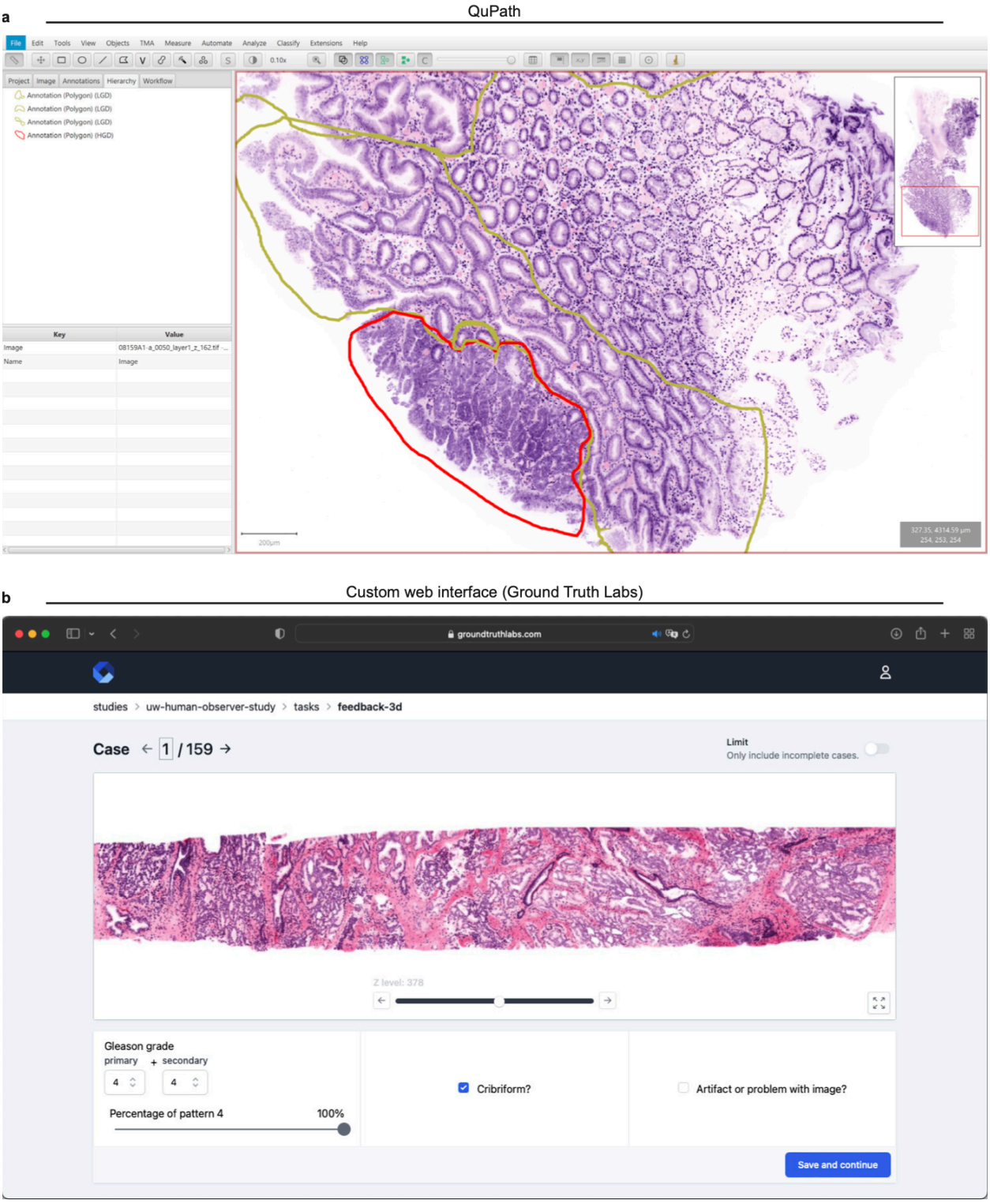


Figure C.10. Alternative interfaces for interacting with Path3D data. **(a)** QuPath interface, showing a false-colored human esophagus biopsy. Pathologist annotations indicating regions of low-grade dysplasia (yellow) and high-grade

dysplasia (red). **(b)** Custom web interface developed by Ground Truth Labs showing a false-colored human prostate core needle specimen. The integrated grading section below the image allows pathologists to record information such as Gleason grade and presence of cribriform glands for each specimen.

C.11 PSF computation details

The Bead_PSF_computation package allows automatic computation of point spread function (PSF) dimensions across a 3D imaging volume. The input dataset is a 3D volume of diffraction-limited beads (e.g., gold nanoparticles embedded in agarose). First, beads centroids are located within the 3D volume using a method developed by Sofroniew [https://github.com/sofroniewn/psf]. Beads which are not well separated from one another, or whose PSFs are significantly truncated by the volume edges are excluded from further analysis. Next, a 3D Gaussian function is fit to each bead, which takes the following form:

$$G(x,y,z) = C + A * \mathrm{Exp}\left(-\left[\frac{(x-x_o)^2}{2\sigma_x^2} + \frac{(y-y_o)^2}{2\sigma_y^2} + \frac{(z-z_o)^2}{2\sigma_z^2}\right]\right) \quad \text{(C.1)}$$

where C and A are intensity offset and amplitude constants, respectively, x_o, y_o, and z_o are expected values in each dimension, and σ_x, σ_y, and σ_z are standard deviations in each dimension. Finally, the full width at half maximum (FWHM) is computed in each dimension for each bead's Gaussian fit. An arbitrary rotation can optionally be added if the expected PSF is rotated relative to the volume's coordinate system (note that this will impact the relative orientations of FWHM measurements).

Note that diffraction-limited beads are inherently barely resolved (i.e., 2 – 3 pixels per FWHM given Nyquist sampling) and significant variation in Gaussian fits and FWHM measurements between individual beads is expected. A properly aligned microscope should have a global

variance (i.e., average FWHM values in one region relative to another) of 25% or less, while variance between individual beads may be significantly higher (**Figure C.3**).

The resulting data (i.e., centroid coordinates and FWHM values for every bead) can be plotted against one another using the package's three plotting functions:

Histograms (**Figure 4.4**e) show the distribution of FWHM values in a given dimension without regard to the spatial position of each bead. Histograms are a useful starting point to assess the resolution variation within an acquired volume. Some outliers are expected, but most beads should be clustered around a central value.

Scatter plots (**Figure C.3**) show each bead as a single point and plot the bead's FWHM value in a given dimension relative to the bead's centroid coordinate in one dimension. Scatter plots are helpful to visualize changes in resolution as one moves across the field of view.

Heat maps (**Figure 4.4**f and **Figure C.4**) show each bead as a single point, which is color-coded according to the bead's FWMH value in a given dimension and plotted based on the bead's centroid coordinate in two dimensions. Heatmaps are helpful for visualizing higher order changes in resolution. Beads are colored using the "coolwarm" colormap from Matplotlib [91], a perceptually uniform diverging colormap [90]. This choice is intentional in order to accentuate regions of particularly poor resolution.

C.12 Improving Napari efficiency

Napari will by default attempt to load entire TIFF stacks into RAM for visualization, which can be inefficient for large datasets. Computational performance can be improved by instead dynamically loading subregions of a tiled pyramidal TIFF file as the user views them ("lazy loading"). This can be accomplished by using Tifffile [137] to read data as a Zarr format [95] into a Dask array [https://docs.dask.org/en/stable]. For example:

```
import dask.array
import napari
import zarr
import tifffile

store = tifffile.imread('dataset.tif', aszarr=True)
z = zarr.open(store, mode='r')
data = dask.array.from_zarr(z)
viewer = napari.view_image(data)
```

Loading time and storage requirements can also be improved by compressing TIFF files before storage. For example, Tifffile can be used to apply JPEG compression, where a 90% quality compression level can reduce file sizes by ~10× in some cases:

```
import tifffile

tf = tifffile.TiffFile('dataset.tif')

with tifffile.TiffWriter('compressed.tif', bigtiff=True) as tif:
    options = dict(metadata=None,
                   photometric='rgb',
                   tile=(512, 512),
                   compression=('jpeg',90))
    for page in tf.pages:
        tif.write(page.asarray(),**options)
```

C.13 Image processing approaches to normalize signal level

Optimizing experimental conditions should be the first step in addressing nonuniform signal levels across a dataset. However, even after careful optimization, some variation in signal level across large datasets can be unavoidable. Image-processing steps may be applied to improve signal level uniformity if the SNR and dynamic range of the raw images allow. Here we describe computational approaches to two common problems, lateral variations across multi-tile datasets and drops in signal level with depth. The code snippets provided below are for illustrative purposes; complete implementations of these approaches are provided on GitHub:

https://github.com/LiuBiophotonicsLab/FixImage3D

C.13.1 Lateral variations

A variety of factors, such as photobleaching of the overlapping regions between adjacent tiles or illumination light intensity variations across the width of the light sheet can result in lateral variations in signal level across a dataset. These variations are often especially apparent at seams between tiles.

The `stripe_fix` function normalizes the lateral signal level across a dataset. First, the average horizontal line profile is computed across each Z level:

```
## Calculate profiles with background removed
line_prof_n_nobg = np.zeros((img_nobg.shape[1]), dtype = np.float64)

## Grab horizontal line profile
for col in range(img_nobg.shape[1]):
      line_prof_n_nobg[col] =
         np.sum(img_nobg[:, col].astype(np.float64))

## Normalize line profile
line_prof_n_nobg = line_prof_n_nobg / np.max(line_prof_n_nobg)
```

Then, each row of the Z level is divided by the line profile, levelling the intensity horizontally across the image. Any negative values (a result of background subtraction) are set to be zero:

```
for row in range(img_nobg.shape[0]):
        img_nobg[row, :] = img_nobg[row, :] / line_prof_n_nobg

## Set negative values to zero
img_nobg[img_nobg < 0] = 0
return img_nobg.astype(np.uint16)
```

C.13.2 Depth variations

Even in well-cleared specimens, light scattering or absorption can lead to some attenuation of light intensity as the imaging depth is increased. This results in a drop in signal levels at deeper layers relative to the tissue surface.

The `Fix_script.py` script corrects lateral and depth variations throughout the depth of a dataset. First, the 2nd percentile (`p2`) and 98th percentile (`p98`) of signal intensities are computed for every layer from an 8× downsampled dataset:

```
p2, p98 = np.percentile(img_8x,
                        (2, 98),
                        axis = (1,2))
```

Then, in each z-level, the lateral normalization function (`stripe_fix`, described above) and a contrast stretching function (`contrast_fix`) are applied. The contrast stretching function rescales the intensity profile of each layer to a consistent intensity scale, commensurate to the surface level, based on the calculated `p2` and `p98`:

```
for z in range(len(img_3d)):
    img_corrected[z] = stripe_fix(img[z])
    img_corrected[z] = contrast_fix(img_corrected[z],
                                    p2[z],
                                    p98[z])
```

The correction is performed independently on each layer, ensuring that the result of one layer remains unaffected by the others. This enables the possibility of parallelization to expedite the processing time.

VITA

Kevin Bishop is completing his PhD in Bioengineering in the Molecular Biophotonics Lab led by Prof. Jonathan Liu at the University of Washington. There he focuses on developing microscopy systems for 3D pathology, particularly leveraging light-sheet microscopy. Kevin completed his undergraduate degree in Electrical & Computer Engineering at Oregon State University, where he worked in Prof. Matthew Johnston's lab on microfluidic platforms to

interface with integrated-circuit-based biosensors. Prior to his PhD, Kevin worked at Massachusetts General Hospital in Prof. Guillermo Tearney's lab on miniaturized and low-cost systems for optical coherence tomography, and then at Washington University in St. Louis in Prof. Samuel Achilefu's lab developing systems for fluorescence-guided surgery and early cancer detection. Outside of lab, Kevin enjoys running, hiking, reading about/cooking/eating food, and spending time with his partner, cat, and friends.